Fabrication and characterisation of MgLi thin films for neurological implants

Dissertation
zur Erlangung des akademischen Grades eines
Doktors der Ingenieurswissenschaften
(Dr.-Ing.)
der Christian-Albrechts-Universität zu Kiel

vorgelegt von

Lisa Hanke

aus
Hamburg

Kiel
2024

Erstgutachter:	Prof. Dr. Eckhard Quandt
Zweitgutachter:	Prof. Dr. Regine Willumeit-Römer
Drittgutachter:	Prof. Dr. Markus Valtiner
Datum der Disputation:	25.10.2024

Contents

Abstract

Due to their mechanical properties, biocompatibility and degradability, magnesium alloys are promising materials for various medical implants, such as bone fixations or stents. Compared to other materials, negative long-term effects of the implants or a second operation to remove the implant can be avoided. Another advantage of the degradation of the material is the potential therapeutic effect of the alloying elements itself. In this work, magnesium-lithium alloys are considered as biodegradable reservoirs for lithium which can be used for neurological treatments. For this purpose, small implants with defined structures need to be fabricated. This manuscript describes the requirements and properties of the thin films produced by magnetron sputtering. Particular attention is paid to the corrosion properties, as these determine not only the lifespan of the implants but also the concentration of released ions. Different possibilities to tailor the properties of the films are also discussed.

In a first study, alloys with four different lithium fractions were compared in terms of their structural and mechanical properties and corrosion rate. A subdivision of the properties according to the phases present in the film was found. While the single-phase alloys exhibited a corrosion rate similar to that of unalloyed magnesium films, which only slightly increased with lithium content, secondary phases sometimes resulted in strongly increased corrosion rates due to galvanic corrosion in the absence of passivating surface films. However, the corrosion rate could also be controlled by other factors, such as orientation or grain boundary modification by changing the sputtering parameters during the manufacturing process.

The release of lithium during degradation determines the effectiveness of the implants as a reservoir for neurological treatments. It has, therefore, been studied over longer periods as well as at the onset of corrosion. The onset of contact with the solution is of particular interest as the surface films and surface processes significantly influence corrosion, especially for thin films. A lithium carbonate film, which forms in air and dissolves during immersion, was identified on the studied thin films. Subsequent selective dissolution of the lithium leads to a change in concentration throughout the measurement.

Since the bulk structure of the film and the surface affect the corrosion resistance, both can be altered to adjust the properties. A plasma treatment with a dielectric barrier discharge plasma resulted in a change in surface chemistry and morphology. The modified surface showed improved corrosion resistance after only a few seconds of treatment. The addition of silver to the alloy increased the tensile strength while not significantly affecting corrosion rate.

This study, thus, provides a first insight into magnesium-lithium thin films as neurological implants and different processes and options to consider for optimising the films for the application.

Zusammenfassung

Magnesiumlegierungen sind aufgrund ihrer mechanischen Eigenschaften, Biokompatibilität und Degradierbarkeit vielversprechende Materialien für den Einsatz in verschiedenen medizinischen Implantaten wie beispielsweise als Knochenfixierung oder Stents. Im Vergleich zu anderen Materialien können negative Langzeitfolgen der Implantate oder ein zweiter Eingriff zur Entfernung des Implantats vermieden werden. Ein weiterer Vorteil des Abbaus des Materials liegt in der potentiellen therapeutischen Wirkung der beinhalteten Legierungselemente. In dieser Arbeit werden Magnesium-Lithium-Legierungen als biodegradierbare Reservoirs für die neurologischen Behandlungen mit Lithium betrachtet. Hierzu müssen kleine Implantate mit definierten Strukturen angefertigt werden. Die folgende Arbeit beschreibt hierzu die Anforderungen und ermittelten Eigenschaften von Dünnschichtfilmen, welche durch Magnetronsputtern hergestellt wurden. Ein besonderes Augenmerk liegt auf den Korrosionseigenschaften, da diese nicht nur die Lebensdauer der Implantate, sondern auch die Konzentration der Wirkstoffe bestimmen. Zusätzlich werden verschiedene Möglichkeiten diskutiert, die Eigenschaften der Filme anzupassen.
In einer ersten Studie wurden Legierungen mit vier verschiedenen Lithiumkonzentrationen bezüglich ihrer strukturellen und mechanischen Eigenschaften und ihrer Korrosionsrate verglichen. Es ergab sich eine Unterteilung der Eigenschaften abhängig von den in Film vorliegenden Phasen. Während für die einphasigen Legierungen eine Korrosionsrate ähnlich zu Magnesiumfilmen ohne Legierungselemente ermittelt wurde, welche mit Lithiumgehalt leicht anstieg, führten sekundäre Phasen teilweise zu deutlich erhöhten Korrosionsraten aufgrund von galvanischer Korrosion, wenn keine passivierenden Oberflächenfilme entstanden. Die Korrosionsrate konnte allerdings auch durch weitere Faktoren wie beispielsweise die Orientierung oder Änderung der Korngrenzen durch Anpassung der Sputterparameter während des Herstellungsprozesses angepasst werden.
Die Lithiumfreigabe während der Degradation definiert die Wirksamkeit der Implantate als Reservoir für neurologische Behandlungen. Aufgrund dessen wurde diese sowohl über längere Zeiträume als auch während des Starts der Korrosion betrachtet. Der Beginn des Kontakts mit der Lösung ist von besonderem Interesse, da gerade für dünne Filme die Oberflächenfilme und -prozesse die Korrosion maßgeblich beeinflussen. Auf den untersuchten Dünnschichten wurde ein Lithiumcarbonatfilm ermittelt, welcher sich an Luft bildet und während der Immersion gelöst wird. Anschließend führt eine selektive Lösung des Lithiums zu einer Konzentrationsänderung über den Messungsverlauf.
Da sowohl die Struktur des Volumens des Films als auch die Oberfläche einen Einfluss auf die Korrosionsbeständigkeit haben, können beide zur Anpassung der Eigenschaften verändert werden. Eine Plasmabehandlung mit einem dielektrischen Barriereentladungsplasma führte zu einer Änderung der Oberflächenchemie und -morphologie. Die veränderte Oberfläche zeigte eine verbesserte Korrosionsbeständigkeit nach nur wenigen Sekunden Behandlung. Die Zugabe von Silber führte zu einer Erhöhung der Zugfestigkeit während die Korrosionsrate unverändert blieb.
Diese Studie bietet somit einen ersten Einblick in Magnesium-Lithium-Dünnfilme als neurologische Implantate und verschiedene Prozesse und Optionen, welche es für die Optimierung für die Anwendung zu bedenken gilt.

1 Motivation

Lithium as a global player material is worldwide known and increases in importance due to its applications for electromobility and energy storage [1, 2]. Besides this, it has advantageous properties for many further applications, not least in the field of medicine.
It is widely used and state-of-the-art for the treatment of bipolar disorder [3, 4] and can also be prescribed for several other mood disorders, including suicidal behaviour [5]. Further, a beneficial effect on the treatment of other neurological diseases such as Alzheimer's, Parkinson's or ischemic strokes is observed [6–11]. However, the use in medicine is discussed controversially due to possible side effects. Lithium is only a trace element in the human body with a blood serum level of 2-4 ng/g [12]. Continuous Li intake or high concentrations can lead to side effects ranging from nausea to severe tremor, kidney dysfunction, epithelial cell disease or renal failure [13–15]. Since the desired lithium levels for, e.g., bipolar disorder range only from 0.4 mmol/l to 1.2 mmol/l [16], it needs to be carefully controlled and adjusted for a patient.
Therefore, a local treatment by placing a reservoir directly in the brain is advantageous to reduce the necessary dosage and to avoid exposure of the overall body to the drug. The release of Li from implants such as, e.g., ceramics or hydrogels in treatments for bone regrowth or nerve regeneration has been tested before [17–20]. Placing such implants in the brain comes with many additional challenges regarding size, placement and interaction with the tissue. Biodegradable thin-film implants offer an option for fabricating small implants that allow continuous ion release. Biodegradable materials degrade over time in the body until full dissolution when the task of the implant is fulfilled [12]. This prevents the necessity of additional surgery to remove the implants and results in ion release of all ions included in the material. Biodegradable metals of interest include magnesium, iron and zinc [12, 21, 22]. Magnesium is the biodegradable material which is most widely studied and discussed. The corrosion rate of Mg is found to be the highest, followed by Zn and Fe. Thus, while extensive research is done on Mg alloys to reduce the degradation rate, the studies on Fe-based alloys try to enhance the degradation rate [23]. All three materials are biocompatible and are of interest for different biomedical applications, depending on the degradation and mechanical properties needed [12, 21, 22].
To prepare local Li-releasing implants, biodegradable alloy thin films can be used. If Li is directly present in the alloy, no further steps for adding the therapeutic element are necessary, and a simple process for easily adjustable shapes and sizes can be carried out. Since Mg can offer additional therapeutic advantages for neurological disorders [24, 25] and previous studies on the preparation of Mg-based thin films were carried out [26–32], MgLi alloys were investigated as the material of choice. The process for fabricating Mg alloy thin films with adjustable structure was previously developed by Haffner et al. [26]. The released Li concentration can be influenced by the Li content in the alloy, the area of the reservoir and the corrosion rate. However, the degradation process is not that straightforward in praxis due to several connected processes influencing each other. This includes the oxidation and release of the metal alloy elements, hydrogen evolution, formation of components such as oxides and hydroxides as corrosion products but also the effect

of such products as passivating surface layers, influence of the ions in solution and the preferred release of one element from the alloy [33–35]. Additionally, negative side effects due to corrosion products such as pH change, hydrogen gas bubble formation and ion release can occur and can cause problems when interacting with the surrounding tissue [36, 37]. Therefore, the material properties and degradation processes need to be studied and understood in detail in a physiological surrounding to allow control and adjustment of the ion release for treatments.

The goal of this thesis is to give first insights into the fabrication and properties of MgLi thin films for the usage as neurological implants and provide possibilities to adjust the properties according to the application.
Therefore, in the first sections 3.1 and 3.2, the fabrication and general properties of MgLi alloys prepared by magnetron sputtering with different Li contents are described. This includes the properties such as microstructure, phase, mechanical properties, and corrosion rates of stress-free thin films, as well as the possibility of adjusting parameters by changing the sputtering parameters.
Since the application is mainly based on the degradation of thin films, a particular focus is placed on understanding the corrosion process. The influence of the solution in long-term studies and additional analysis on the corroded samples is discussed in section 3.3.
In the manuscript in section 3.4, the degradation and ion release of films with low Li content are then analysed to study the corrosion processes and passivating layers on the sample surface. This also includes the changes of films in air and ageing effects.
Additionally, the corrosion of the thin films can be changed by additional elements (section 3.6) or a post-treatment. In chapter 3.5, the influence of an easy and fast post-treatment by dielectric barrier discharge - plasma is described.

2 Fundamentals

To underline the possibilities and challenges for MgLi thin films as a biodegradable implant material for local drug release, the following chapter will discuss the underlying principles and state of the art. Therefore, the properties of Mg and Mg alloys, specifically MgLi, concerning medical usage are described first before discussing the influence of the fabrication as thin films.
Since the application is highly dependent on degradation and, thus, corrosion, an additional section focuses on the theory and studies of different corrosion processes and the usability of several measurement techniques specifically for the samples of this work.

2.1 Magnesium and its alloys

Mg is a widely available, second group alkaline earth metal with a melting point of 650 °C [1, 38]. It has the lowest density of construction materials with 1.74 g/cm^3 [39] and a good strength-to-weight ratio [40], leading to applications in several fields such as aerospace or automotive industries [41].
Mg has a hexagonal close-packed (hcp) structure with lattice parameters a =3.2088 Å and c =5.2111 Å [42]. It possesses a Young's modulus of around 44.7 GPa (at 20 °C) [41] and a varying tensile strength between 150-400 MPa [41] depending on factors such as the material purity and fabrication. A lower tensile strength is found for cast material, and higher values are measured for wrought material [41]. The ductility is low due to the low amount of independent slip systems. While slip along the $<11\bar{2}0>$ direction is possible on basal, pyramidal and prismatic planes (figure 2.1) and $<11\bar{2}3>$ slip can take place along the pyramidal planes (figure 2.1), the critical resolved shear stress is much lower on the (0001) basal plane, therefore, slip mainly occurs on those [43–45]. Additionally, twin formation on the $\{10\bar{1}2\}$ and $\{10\bar{1}1\}$ plane is possible.

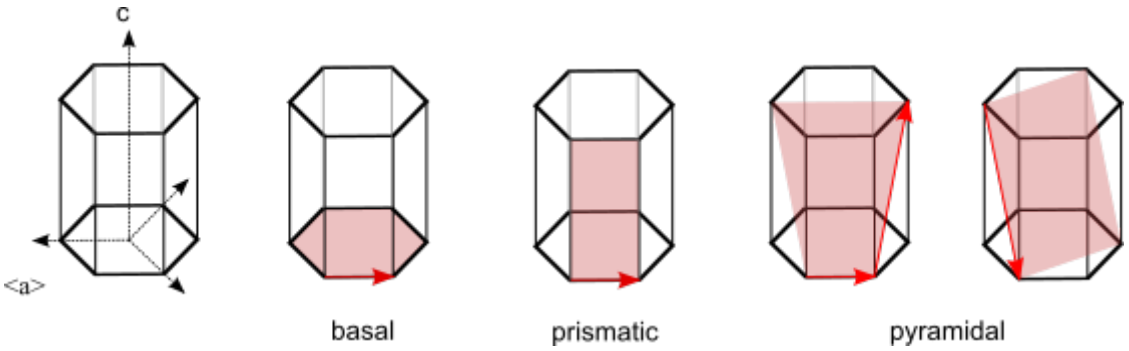

Figure 2.1: Slip systems in a hexagonal unit cell of Mg.

If the material is in contact with water for specific applications, the degradation needs

to be considered in addition to its structural and mechanical properties. Mg possesses a low standard electrode potential of -2.37 V vs SHE (standard hydrogen electrode) [46 a], which leads to high corrosion rates. Due to the complexity of the corrosion process and the importance for the applicability of Mg-based materials, it will be discussed separately in section 2.3.

2.1.1 Applications in medicine

While the corrosion of Mg should be avoided for applications such as the automotive industry, this property can also be used as an advantage if the degradation process is controlled. In medicine, Mg and Mg-based alloys are studied for biodegradable implants to avoid side effects of long-term implants or prevent additional operations for implant removal [22].
Mg is already present in human bodies with approximately 25 g [47], and an intake of around 300 mg is necessary for adults per day [1]. It is important for many cellular processes, used as an intracellular cation and takes part in over 600 enzymatic reactions [47]. Mg is partially stored in bones, and any excess Mg can be filtered by the kidney, thus not leading to side effects when Mg is released during the degradation of implants [47, 48].
The usage of Mg for implant materials is not a new development [49]. The first Mg implants, Mg wires, were tested in 1878 by E.C. Huse [50]. Further studies were conducted around the beginning of the 20th century. The implants often did not lead to any infections or pain, but subcutaneous gas cavities could form. In general, the corrosion products and hydrogen gas proved to be the biggest hindrance for a wide use of Mg implants due to possible reactions with the tissue [36, 37]. Thus, the corrosion process of the material in solution, in vitro and in vivo, has been studied to overcome the challenges of corrosion control. For each application, specific requirements need to be considered. This includes, e.g., for vascular stents the mechanical stability for at least six months, a corrosion rate below 0.1 mm/yr [22] and a low hydrogen evolution to avoid side effects due to gas bubbles [51].
By understanding the corrosion and adapting it accordingly, several products have reached an animal or clinical trial or even the market. This includes stents (Magmaris®: coronary stent and UNITY-B: biliary stent [52–54]) and orthopaedic implants such as screws and pins [12, 55, 56]. In addition to the advantage of degradation of the implant, the mechanical properties of Mg are closer to the mechanical properties of bones than other typical implant materials, thus leading to less mismatch and side effects [57].
Nanoparticles, flakes and coatings of Mg were also studied as therapeutic materials by drug loading of the biodegradable material or taking advantage of directly formed active species such as hydrogen and pH shift leading to stress in bacteria and cytotoxic effects [58–61].
Since Mg takes part in neurological functions by neurotransmission, connection at the neuromuscular junction or prevention of excitotoxicity [24, 25], diseases such as Alzheimer's, Parkinson's, epilepsy, anxiety and depression could be influenced by it [25]. Therefore, Mg is not only advantageous for preparing biodegradable substrates for other treatments but also for a release during degradation in the brain, which might be beneficial for treating disorders. While the studies described in this work mainly discuss the effect of Li release from MgLi alloys as a therapeutically active element, Mg itself can, therefore, also positively affect the treatment.

2.1.2 Mg alloys for medical applications

While the properties of Mg itself can be slightly influenced by adjusting, e.g., the fabrication and microstructure, a more fundamental change occurs when additional alloying elements are included. This can significantly change properties such as mechanical behaviour and corrosion. Several studies discuss alloys such as WE alloys (Y+rare earth element-Mg alloys) or AZ alloys (Al+Zn- Mg alloys), mainly produced by casting, rarely as wrought alloys [62]. However, for medical applications, the biocompatibility and non-toxicity of the elements are the deciding factors. While Al is, for example, often added in Mg alloys to improve strength and castability, the possible negative effect on neurological pathologies makes it unfit for usage in implants [63].
Thus, mainly elements such as Ca, Zn, Zr, Sr or rare earth elements (REE) are studied [64]. Ca is already present in the human body and has advantageous effects such as a reduction in grain size and improved mechanical properties while not influencing the corrosion resistance negatively. Good corrosion resistance and mechanical stability are found for low amounts of Zn, Zr or Sr. The properties are not only influenced by a change in structure but also by additional protective films formed by the added elements. REE improve corrosion resistance and strength; however, toxicity cannot be excluded, even though advantages can be found in possible anti-carcinogenic properties [63].
Alloying with Li is also possible, often in addition to other elements such as Al, Zn, Ca or REE, to change strength and ductility [65–67]. Even though Li is a mild toxic element [68], it was discussed for its usage in medical applications [69–71], and in experiments, no negative effect on cell lifetimes was found [68]. Alloys such as the LZ alloys (Li+Zn) are studied for the use in medical applications with the addition of Zn to reach high strength in the mixed phase [66].

2.1.3 MgLi

MgLi is of interest for this work due to the effect of Li on mood disorders such as depression, reduction of suicide and suicidal behaviour [5] and the possibility of reducing side effects by placing a local Li reservoir in the brain. However, to foresee the behaviour of such an implant, the properties of the material have to be determined.
MgLi possesses a lower density than pure Mg of 1.35-1.65 g/cm^3 [72] due to the low density of Li itself (0.534 g/cm^3 [38]). The addition of Li not only leads to a reduction in density but also an increase in formability and ductility [73]. The specific strength and stiffness can be kept relatively high, even though ultimate tensile and compressive strength are reduced [72, 74]. This change in mechanical properties occurs mainly due to the change in crystallographic structure. Li has a bcc structure with a =3.5089 Å [75] and is the only element that changes the hcp lattice of pure Mg to body-centred cubic (bcc) at room temperature [74]. Three different zones can be defined in the MgLi phase diagram [76] (see figure 2.2). Up to roughly 5-5.6 wt% or 15.6-17.2 at% of Li (temperature dependent), the Mg-rich α-phase is present as hcp. It is often named α-Mg or α-MgLi. For high fractions of Li over roughly 10.9 wt% (30 at%), a bcc structure, β-Li or β-MgLi, based on the structure of pure Li is present. Between these compositions, a mixed α+β-phase is formed.
Including Li reduces the a and c lattice parameters and the c/a ratio even for the α- phase

(comparison: $a = 3.2076$ Å, $c/a = 1.6227$ for 0.65 wt% vs. $a = 3.193$ Å and $c/a = 1.6068$ for 5.24 wt% Li) [42].
The change of hcp to a more cubic-like structure or the presence of bcc leads to the availability of more slip systems for mechanical deformation. With a c/a ratio closer to 1, the prismatic and pyramidal slip are more pronounced, leading to a higher ductility and maximum elongation [77, 78]. The elongation varies depending on the Li content. Zhou et al. found, e.g., an increase from around 15 % to 41 % from Mg3.5Li to Mg8.5Li [79]. On the other hand, while low amounts of Li can increase the strain hardening and yield strength, further Li addition and additional slip lowers the possibility for strain hardening and reduces the tensile strength [78]. Furthermore, the plastic anisotropy is reduced, and in comparison to pure Mg, the grain growth during recrystallisation is increased [77]. β-MgLi shows an especially high formability, ductility and slightly reduced Young's modulus but also lower strength and low thermal and creep resistance [72, 80].

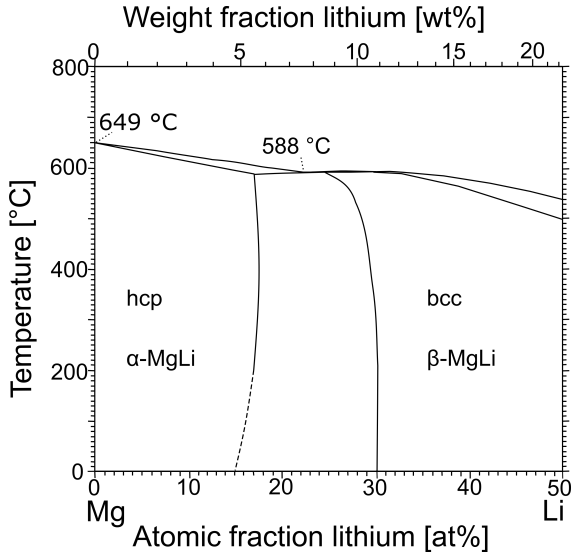

Figure 2.2: Phase diagram of Mg-Li. Reproduced and adapted with permission from Springer Nature [76].

While Li could be equally distributed in the single phase material or grains from each phase in the mixed material, a segregation at the grain boundaries is found even for low Li fractions [81]. This can either lead to an enhanced embrittlement or improved grain boundary sliding. For mixed-phase materials after heat treatment and mechanical treatment, grain boundary sliding was found to lead to superplasticity [72]. The Li segregation at grain boundaries possibly influences the diffusion of Li, which is in general lower for α-phase than β-phase [82, 83], leading to an easier transport of Li to the surface over grain boundaries also for the hcp phase. The accumulation of Li could also affect the corrosion properties of the material which will be described later.
In addition to the phases, the properties of MgLi are also influenced by microstructure. Different post-treatments such as heat treatments or mechanical treatments, e.g. rolling, change grain sizes and texture [40, 72, 84]. This can lead to hardening of the material. Especially for nanostructured Li-rich materials, an improved strength is found [40]. Other elements such as Zn, Al or REE are often added for improved properties [40, 65, 66].
Working with MgLi also has additional challenges due to the high reactivity of Li. This leads to high oxidation [72] and complicates the processing. Especially for β-MgLi, ad-

ditional ageing effects result in the formation of precipitates and recrystallisation to a partial α-phase even at room temperature [85, 86]. This can lead to age softening and defect formation at interfaces between both phases. Therefore, the properties also depend on the time between sample preparation and experiment.

2.2 Sputtered thin films

The definition of thin films differs in the literature. While some describe that a thin film is thinner than 1 µm [87, 88], it can also include structures in the µm-range or even 100s of µm if the material is still small in comparison to the substrate [89]. Thin films can be fabricated by different techniques using solid, liquid or gaseous deposition [90]. The most commonly used techniques are chemical (CVD) or physical (PVD) vapour deposition. In PVD, the material of choice is brought into the gas phase by physical means such as heat or ion bombardment. The atoms will then deposit and form a layer on the chosen substrate without any additional chemical reactions taking place.
Sputtering as one of the PVD techniques is carried out in a vacuum chamber which is flooded with an inert gas such as argon for non-reactive sputtering [91]. An applied voltage starts a plasma between the target material and the substrate. Due to the bombardment of the target by compounds from the plasma, atoms of the target will be ejected and deposited on the substrate. For a higher sputtering rate and lower necessary voltage and pressure, permanent magnets can be placed behind the targets for the so-called magnetron sputtering [90, 92]. This leads to a longer, spiral path in the plasma and, thus, further ionising by interaction of gas atoms. Therefore, the amount of ions hitting the target is increased, leading to a higher sputtering rate. A side effect is the formation of specific sputtering trenches due to the small area of attack. The composition of materials including multiple elements can differ from target to deposited material since, depending on the atomic number of the elements, the atoms have a different angular distribution.

2.2.1 Microstructure of thin films

During sputtering, parameters of the process, such as the applied power, pressure of gas and gas flow, can be adjusted. This can then increase or decrease the energy of the atoms, therefore influencing the microstructure formed during deposition.
The development of microstructure dependent on the temperature of the substrate (T_s) and melting temperature (T_m) as $T_\mathrm{s}/T_\mathrm{m}$ was described by Movchan and Demchishin in 1969 [93], indicating different zones 1-3 depending on the substrate temperature since it influences the energy available for activation and, thus, diffusion.
Thornton then added the dependence on the pressure and developed the structure-zone model shown in figure 2.3 [94, 95]. The model is mainly described by zone 1-3 and a transition zone T between 1 and 2 [94, 95, 97].

- In **zone 1** with the lowest $T_\mathrm{s}/T_\mathrm{m}$, the low diffusion leads to a high defect density, shadowing and open grain boundaries. The diameter of the grains increases with

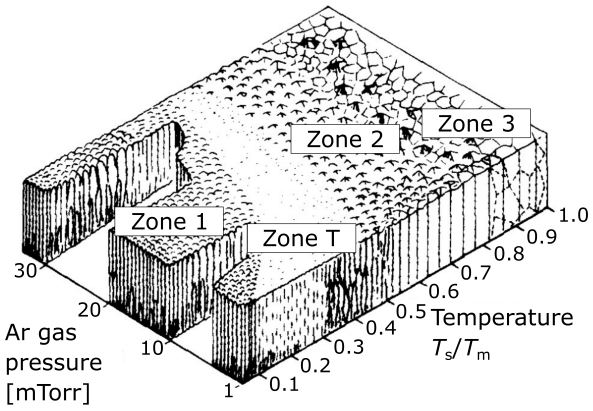

Figure 2.3: Structure-zone model developed by Thornton showing the microstructure of sputtered films dependent on the temperature (substrate temperature T_s and melting temperature T_m) and the inert gas pressure. Reproduced with permission from Elsevier [96].

temperature.

- In the transition **zone T**, surface diffusion is already possible, resulting in a denser structure with the formation of less defined grains or fibrous structures.

- For **zone 2**, a smooth surface and dense grain boundaries between columnar grains are reached, leading to better mechanical properties.

- In **zone 3**, volume diffusion and recrystallisation can occur, forming round grains and microstructures similar to bulk material.

- On the other axis, the increase in **pressure** shifts the transformation temperatures to higher values due to a loss in kinetic energy.

The revised structure-zone model by Messier et al. exchanged the pressure with a substrate floating potential and claims the T zone as a subzone of zone 1 [98]. Barna and Adamik also added the importance of impurities on the final structure [99], and Anders adjusted the model by switching to a generalised temperature and normalised energy flux to account for other deposition techniques [100]. Thus, the different structure-zone models can give an insight into the approximate structure of thin films but need to be defined and adapted for the system of interest [97].
In comparison to bulk materials, fewer precipitates are found in sputtered films. This is due to the fast cooling rate during deposition, leading to non-equilibrium supersaturated solutions of materials which can possess very different melting points [32].
In addition to the microstructure described in the structure-zone model, changing the sputtering parameters also influences the film stress, specifically, the intrinsic film stress defined by the structural disorder [96]. For the fabrication of stable, possibly freestanding thin films, an optimisation to low film stress is necessary to prevent such films from deformation after lift-off from the substrate.

2.2.2 Mg alloy thin films

For medical applications, Mg alloy thin films are of interest in different forms such as coatings or freestanding films for, e.g., stents or scaffolds [26, 61]. Fabrication by sputtering leads to the advantage of an easy change in structure (amorphous or crystalline), adjustment of thickness, production of supersaturated single-phase materials and structuring by other thin-film techniques [27, 61].
Sputtered Mg alloy thin films show a strong preferred orientation and, thus, higher texture than bulk material. This is influenced by a preferred growth in [0001] direction due to the lowest surface energy of the (0001) planes [28], leading for MgAg and WE alloys to a columnar growth with grain sizes in µm range and a grain length equal to the film thickness [28, 29].
The influence of different alloying elements such as Ag, Zn, Ca and REE on the film properties have been tested. While for MgAg typically only 2 wt% Ag are soluble in Mg, sputtering can form metastable solid solutions up to 6 wt% before precipitates occur [28]. By adjusting sputtering parameters, even metallic glasses such as Mg50Zn5Ca, which thus have a high solubility and no precipitates, can be fabricated [30]. The parameters need to be chosen as low power and high pressure to reduce diffusion.
For many alloying elements such as Ag, Y and Gd, an increase in lattice parameter with addition of the alloying element is found [27, 31]. The surface roughness is also reduced for sputtered AZ alloys in comparison to sputtered Mg [101].
The texture and addition of elements influence the mechanical properties due to solid solution strengthening, high defect densities and small grain diameters [28, 31]. A higher yield strength is determined for MgAg, MgY and MgGd when including more of the alloying element, while the Young's modulus stays similar [28, 31]. The maximum elongation is often decreased at the same time [28]. The influence of sputtering parameters for the different alloys was analysed. Studies claim an influence of the sputter pressure on the maximum elongation due to lower diffusion and increasing inert gas atoms addition to the films for higher pressure [29]. A change of pressure and power can change between brittle and ductile films, even leading to amorphous materials [29, 30, 102].
While the adapting of parameters for changing the microstructure is dependent on the specific alloys, a general route for the structuring and fabrication of freestanding thin films in a thickness range of 10-250 µm was developed by Haffner et al. [26] and is described as performed in the studies for this work. The outline is shown in figure 2.4. It includes UV-lithography, magnetron sputtering and etching steps.
In the first step, a silicon wafer is coated by spin coating with an image reversal resist (a). After transferring a mask structure onto the wafer by illumination with ultraviolet light and removing the non-illuminated photoresist (b), a layer of Al with a thickness of approximately 150 nm is added by magnetron sputtering (c). The resist is then dissolved in acetone so that only the structure remains as an Al hard mask (d).
A Bosch process is then carried out by ICP-RIE (inductively coupled plasma - reactive ion etching) to etch up to a depth of at least 20 µm for the films produced in the following studies, often further to up to 60 µm (e). After cleaning in acetone and isopropanol, AlN is added with a thickness of 500 nm by reactive magnetron sputtering using an Al target and nitrogen gas (f) before the final sputtering of Mg alloy (g). During the lift-off in 20 wt% KOH, the sacrificial AlN layer is dissolved (h). The freestanding thin films can then be cleaned in distilled water and isopropanol before drying them with nitrogen.

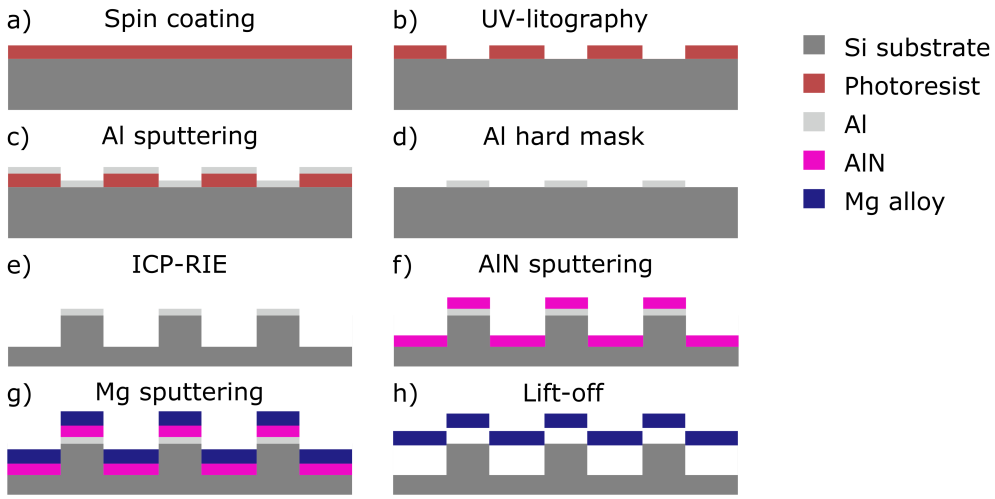

Figure 2.4: Fabrication steps for freestanding Mg alloy thin films using UV-lithography, magnetron sputtering and sacrificial layers as performed for this work, based on the process of Haffner et al. [26].

2.3 Corrosion

Corrosion can occur by chemical or electrochemical means or with the additional influence of biological matter [103 a, 46 b]. It is, in general, defined as the degrading or destruction of a material due to reactions with the environment. While corrosion was defined in the past mainly for metals, it can now include the degradation of all materials [46 b]. The type of corrosion described in the studies of this thesis is electrochemical, more specifically, metal corrosion and oxidation in an aqueous solution. The overall reaction includes an anode, a cathode, an electrolyte and a path for the electrons to transfer between the electrodes, forming a corrosion cell. Other factors, such as temperature, pH, and salt in the solution, can further influence the reactions that take place. [104 a]
While the anodic reaction includes the corrosion and dissolution of the sample by oxidation, the cathodic reduction reactions can include different reactions depending on the reaction medium and electrode potential. The probability or strength of corrosion is described by the electrode potential, which is always defined as the potential compared to another electrode. Metals with a lower electrode potential are more prone to corrosion and will act as anodes if they are in contact with metals with a higher potential. [103 b]
While corrosion in aqueous solution, in general, is defined by the ion release, this does not have to be a continuous release over the surface. The different types of corrosion are split into homogeneous and local corrosion, which includes, but is not limited to, galvanic, dealloying, intergranular, filiform, pitting and crevice corrosion [103 c, 46 c, 104 b]:

- For **homogeneous** or **uniform corrosion**, the reaction takes place on the overall surface. It often occurs if no stable passivating layer is formed. While measurements and calculations for corrosion rates only assume uniform corrosion, other corrosion types also take place and need to be considered.
- In **galvanic** or **microgalvanic corrosion**, two metals or metal phases are in contact

with each other, leading to faster corrosion of the compound with the lower electrode potential.

- Similar to galvanic corrosion, **dealloying corrosion**, also called **selective corrosion**, describes the dissolution process of one specific alloying element due to the lower potential.
- If a difference in potential occurs at grain boundaries due to, e.g., preferred accumulation of one compound at boundaries, this could lead to **intergranular corrosion**.
- When corrosion products are formed during corrosion, they can form filaments on the surface, which start from surface defects and lead to an active anodic head of the filament and a growing cathodic area of corrosion products. This process is called **filiform corrosion**. It often occurs if the corroding material is coated.
- **Pitting corrosion** occurs if the material itself is not homogeneous or the passivation layer forms cracks or other defects, leading to a preferred attack and formation of pits at those places. It can also be influenced by highly reactive anions in solution.
- **Crevice corrosion** takes place if another object limits the volume above an area of the sample and less exchange of solution occurs, leading to localised corrosion.

2.3.1 Mg corrosion

Mg has a very low electrode potential of -2.37 V vs SHE [46 a]. The redox reaction consists of the anodic Mg ion release and cathodic hydrogen evolution. Mg ions and hydrogen can then further react to Mg hydroxide. [105]

$$\begin{aligned} &\text{Oxidation:} && \mathrm{Mg} \longrightarrow \mathrm{Mg^{2+}} + 2\,\mathrm{e^-} \\ &\text{Reduction:} && 2\,\mathrm{H_2O} + 2\,\mathrm{e^-} \longrightarrow 2\,\mathrm{H_2} + 2\,\mathrm{OH^-} \\ \hline &\text{Redox:} && \mathrm{Mg} + 2\,\mathrm{H_2O} \longrightarrow 2\,\mathrm{H_2} + \mathrm{Mg(OH)_2} \end{aligned}$$

Since Mg often reacts to MgO and forms an oxide layer in air, the reaction to $Mg(OH)_2$ can also be rewritten as

$$\begin{aligned} 2\,\mathrm{Mg} + \mathrm{O_2} &\longrightarrow 2\,\mathrm{MgO} \\ \mathrm{MgO} + \mathrm{H_2O} &\longrightarrow \mathrm{Mg(OH)_2} \end{aligned}$$

The change and reaction of the surface layer are influenced by the stability of such layers on the surface and solubility in water. The stability is typically described by the Pilling-Bedworth ratio (PBR) [106, 107]. The ratio defines the stress of a surface layer on the substrate by calculating the ratio of the corrosion product's molar volume to the original metal's molar volume. A value of 1, therefore, defines a stress-free film, and any value of PBR=1-2 is defined as relatively stable. While <1 means that tensile stress occurs, a

PBR>1 leads to compressive stress. For MgO, the PBR is <1 with 0.8, but for $Mg(OH)_2$, a value of 1.8 and, therefore, a more stable film is reached [108].
The stability of surface layers is, however, also dependent on an applied potential and the pH of the aqueous solution. Those parameters and the responding products are given in Pourbaix diagrams, showing different areas of reactions [109]. The reaction and formation of $Mg(OH)_2$ is just stable for a higher, alkaline pH [109] and, thus, the pH influences the corrosion by reducing the corrosion rate for a higher pH [110, 111].

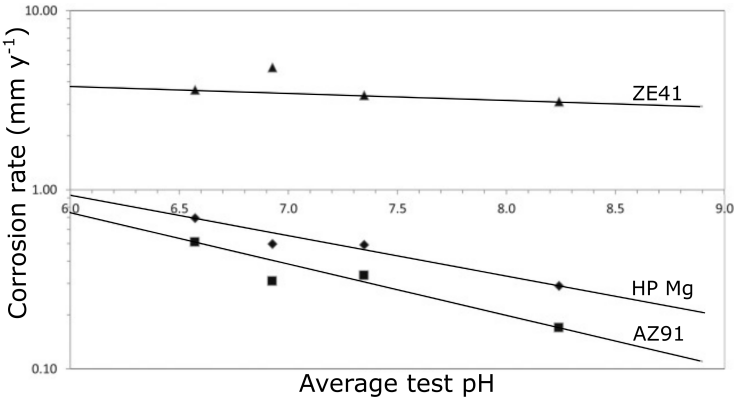

Figure 2.5: Corrosion rate dependent on the pH in Hank's balanced salt solution (buffered) for three exemplary Mg materials (high purity Mg HP Mg, AZ91, ZE41 Zn+REE). Reproduced and adapted with permission from Elsevier [111].

At a pH of 7.4, which corresponds to the pH in a human body, neither $Mg(OH)_2$ nor MgO are stably formed and therefore do not hinder further reaction and dissolution [112]. However, $Mg(OH)_2$ can still form at lower pH due to an increase of pH close to the sample by the reactions taking place [32]. Since the corrosion rate reduction due to the hydroxide layer is higher for a higher pH, the open circuit potential (potential of the sample vs. reference in a certain system if no voltage is applied, E_{OCV}) can also shift pH dependently [113, 114].
An additional point to consider when describing the corrosion of Mg is that the cathodic and anodic reactions cannot be easily separated. For a standard metal, the cathodic reaction - in this case, hydrogen evolution - takes place if a negative potential is applied, while a positive potential leads to more anodic reaction, thus, metal dissolution and a decrease in the cathodic reaction rate. However, for Mg alloys, an enhanced voltage also leads, in many cases, to an increase in hydrogen evolution and a fast Mg dissolution, which already starts in the cathodic region. This is called negative difference effect (NDE) [105, 115, 116]. Certain theories, such as the presence of Mg^+ ions or the influence of the protective film as cathodic regions for hydrogen evolution, have been proposed. Both hypotheses were contradicted by other studies [34, 115, 117–119]; thus, no final explanation has been determined.

2.3.2 Influencing factors

The corrosion process and rate of Mg are very complex and influenced by several factors, such as the structure, including microstructure and texture, the solution in which corrosion

takes place and additional elements. The importance of these factors will be discussed in the following sections.

Influence of structure

The structure of the Mg samples can highly influence the corrosion rate. This is often used to lower the rate by thermal or mechanical treatments [120]. Hereby, two main factors are changed: grain size and orientation. The influence of grain size is widely studied. Grain boundaries, in general, count as defects, increase the area available for corrosion start and, therefore, could increase the corrosion rate, especially if a change of composition occurs between grain volume and boundary [121, 122]. However, it is often found that small grains lead to improved corrosion resistance due to the formation of a more uniform passivating film [121–123], smaller precipitates [32] or a change in potential at the grain boundaries [124]. The formation of a better passivating film also explains why short-term measurements might show higher corrosion rates for small grains since the film has not been stably formed.
The orientation of grains and, thus, the texture also changes the corrosion rate. Even though all grains consist of the same phase, each plane can show a slightly different corrosion rate, mainly influenced by the strength of bonds between the atoms. Therefore, theoretically, the densest plane should possess the best corrosion resistance, which is the (0001) plane in the case of Mg [125, 126]. However, planes with the lowest activity for reactions also have the lowest activity towards, e.g., oxidation, therefore forming thinner oxide or protective layers [127–129]. A uniform texture might also be critical for low corrosion additional to the specific plane since it prevents galvanic coupling [130]. Therefore, the preference of a structure for good corrosion resistance has to be determined for each particular system of sample alloy and surrounding.

Influence of solution

As already described for the pH in section 2.3.1, the solution in which corrosion takes place strongly affects the corrosion rate. This is even more true if additional ions are involved [131]. Kwon et al. showed a strong difference in the corrosion behaviour of a Mg alloy if different ions were present in the solution even though the pH was held constant [132]. Silva et al. found that the oxygen content can also influence the corrosion [133].
When working under physiological conditions, either just in a salt solution or in vitro or in vivo, the system is complex. While added organic components such as molecules and cells can also influence [134], the experiments in these studies are carried out in salt solution; thus, this effect is mainly described in the following.
In salt solutions such as Hank's balanced salt solution (HBSS), hydrocarbonates, carbonates, and carbon dioxide are often present as buffering systems or from air, leading to the formation of $MgCO_3$ or more complex carbonates [135]. The formation of carbonates, in general, was found by Santucci et al. [112] to be more stable with increasing pH and increasing concentration, while $MgCO_3$ specifically is stable in a broad pH range. Additional salts, including elements such as Ca, can lead to the formation of further carbonates or phosphates. Ca phosphate is especially known to form a stable product which reduces the corrosion rate [131, 136] (table 2.1). It also has a PBR of 1.27 and, thus, forms a

surface film with low film stress [108].
A complex system including cells or in vivo measurements can influence the corrosion rate [134, 137], but the influence and process of corrosion product formation are still important. Zhao et al. found, e.g., Mg carbonates and phosphates on Mg alloys after implantation into a mouse model, indicating that the effect of salts in solution is also of interest for the final application [138].

Influence of purity

When discussing the influence of additional elements on corrosion, two possibilities have to be considered - impurities and alloying elements.
Impurities are, in general, unwanted additions of elements. When comparing ultra-pure Mg with high-purity Mg, the corrosion rate of ultra-pure Mg is significantly lower [139]. The impurities are problematic if they have low solubility and, thus, form additional phases with higher electrode potential which can lead to microgalvanic corrosion. Since nearly all elements have a higher electrode potential than Mg [46 a], this results in faster Mg dissolution. One impurity which is often included is iron. If the concentration exceeds 0.005-0.017 % [140, 141], it can increase the corrosion rate. Techniques such as sputtering might prevent the formation of additional phases and, therefore, reduce such effects [27].
Elements can also be added on purpose as alloying elements to influence the properties. This can include changing the microstructure or surface properties to reduce the corrosion rate, at least in comparison to Mg with low purity [120]. REE have a similar electrode potential to Mg, and the potential of Ca is even lower, leading to a lower overall potential of the intermetallic phase [142]. A decrease in size of the second phase or continuous distribution preventing the propagation of pits can, e.g., reduce the corrosion rate [108, 143–146]. Since Mg alloys can form passivating surface layers, sputtered Mg alloys have also been discussed as self-healing layers, which can prevent galvanic corrosion [120].

2.3.3 Mg thin film corrosion

The structure of thin films produced by sputtering results in two main factors which can reduce the corrosion, namely a strong texture with basal (0001) planes on the surface and a supersaturated solid solution preventing the formation of additional phases up to higher fractions of the alloying element [27, 31, 126, 147].
Therefore, less pitting corrosion and other local corrosion is found for sputtered samples since less galvanic coupling can occur with precipitates [32]. Blawert et al. also discussed the incorporation of alloying elements of thin films into the passivating layers, leading to a better corrosion resistance if distributed homogeneously, which can further be influenced by changes in microstructure [101].
For WE alloys, no effect of the alloying elements on the corrosion rate occurs since no precipitates are found [102]. Even an increase of the alloying element does not lead to changes as studied for up to around 23 at% of Y or 3.6 at% of Gd [31]. For MgAg, the addition of the element even decreases the corrosion rate by increasing the standard potential when forming a solid solution [27]. A reduction is also measured for amorphous MgZnCa, for which the corrosion rate is possibly reduced by reducing the hydrogen evolution via Zn

	PBR [108]	K_{sp}[149]
Li_2CO_3	1.35	$8.15 \cdot 10^{-4}$
$Mg(OH)_2$	1.80	$5.61 \cdot 10^{-12}$
MgO	0.80	-
LiOH	1.26	-
$MgCO_3$	2.04	$6.82 \cdot 10^{-6}$
$Mg_3(PO_4)_2$	2.29	$1.04 \cdot 10^{-24}$
$Li_3(PO_4)_2$	1.20	$2.37 \cdot 10^{-11}$
$Ca_3(PO_4)_2$	1.27	$2.07 \cdot 10^{-33}$

Table 2.1: Pilling-Bedworth ratios (PBR) and solubility product constants (K_{sp} at 25 °C of possible corrosion products of MgLi in salt solution.

incorporation [30]. For this material, an influence of the sputtering parameters on the corrosion by changing from polycrystalline to amorphous material is described.

2.3.4 MgLi corrosion

The electrode potential of Li is even lower than for Mg with -3.05 V vs SHE [46 a]. Thus, Li enhances the reactivity and the corrosion rate. It is found to increase the hydrogen evolution by increasing the cathodic kinetics [35, 148]. While Li is studied to reduce the corrosion resistance short term, studies also show enhanced resistance over longer measurement times [33]. This might be influenced by a stronger increase in pH during the beginning, which stabilises $Mg(OH)_2$ on the surface afterwards [73].
Since the influence of corrosion products on the corrosion resistance is influenced by the stability and solubility, PBR and solubility product constants of possible components formed by MgLi in salt solutions are listed in table 2.1. The effect of Li on the corrosion is highly influenced by the exact amount of Li. The main change depends on the MgLi phase. In general, the corrosion resistance is often described to be the highest for β-MgLi, followed by α-MgLi and then α+β-MgLi [150].
The corrosion rates and influences for each phase are described in the following sections.

α-phase

For MgLi with a hcp structure, the corrosion is generally assumed to be similar to the corrosion of pure Mg [151]. Thus, the formation of MgO and $Mg(OH)_2$ will occur [152]. Since Li has a lower electrode potential than Mg, the corrosion potential of the alloy decreases with increasing Li content [153]. During the corrosion, anodic and cathodic regions develop on the surface. Hydrogen and corrosion products are formed in the cathodic regions and the corrosion progresses as filiform corrosion [150, 154]. While Li can lower the overall electrode potential, Li et al. found for α-MgLi with different Li fractions the best corrosion resistance for the highest Li fraction due to the influence on microstructure and surface films [153].
In addition to the corrosion products on Mg, Li-containing components are found. For MgLi-based alloys such as, e.g., LA51 (Mg-5Li-1Al in wt%), Li_2CO_3 and LiOH are formed in air on the surface [155].

α+β-phase

In a mixed-phase material, the corrosion is mainly driven by galvanic coupling of two phases [156, 157]. Since the electrochemical potential of one phase - in this case β - is lower than for the other phase, this one is often preferentially corroded and a combination of filiform corrosion and localised corrosion takes place [150]. The corrosion is found to start accordingly at the grain boundary and attacks the β-phase as studied by Song et al. [158].
The corrosion rate also changes over time due to the formation of a protective layer. Since the layer mainly forms on β-phase, Wang et al. described that therefore the main corrosion occurs in β-MgLi at the beginning but later changes to α-phase with increased hydrogen evolution [159]. Due to the higher activity and the higher availability of Li and therefore faster oxidation and reaction to corrosion products (a more detailed description can be found in the section for β-phase), the β-phase might be better protected against corrosion while the α-phase is preferentially attacked. Several stacks of protective films have been proposed on mixed-phase MgLi alloys [108, 159].
The corrosion rate is highly dependent on the amount of each phase and microstructure of the material [157, 160]. The properties of the material can also change if Li diffuses and thus changes the distribution of phases [85, 157, 160]. For structures with smaller grain sizes and higher β-phase fractions, a better protection of the overall material can already be developed similar to the one found on the high Li content phase. The microstructure was changed by forging and rolling for a LZ91 alloy, resulting in a higher corrosion resistance due to smaller grains and a higher β-phase fraction [157]. In addition to the faster diffusion of Li from bcc to the surface, the smaller grains can reduce the stress of surface films formed if the PBR is not 1 [108].
Wang et al. also found an increase in β-phase with rolling, leading to the highest corrosion rate for the middle value of the rolling ratio (rolling ratio of 5 in comparison to 3 and 10) [159]. Thus, for α+β-MgLi, microstructure and Li content influence the galvanic coupling and formation of passivating layers which have the main influence on the corrosion process.

β-phase

The β-phase MgLi alloys include the highest Li fraction and, therefore, the highest activity. However, several studies found the lowest corrosion rate for those materials, mainly due to a protective film formed during corrosion [151, 161, 162]. This film formation leads to less pitting and a corrosion resistance which is enhanced over time while intergranular corrosion can still take place [33, 150]. The single phase exhibits low hydrogen evolution and development of few defects [163]. It also shows a lower NDE than α-MgLi [164].
Layer systems including oxides, hydroxides and carbonates were discussed [40, 161]. Since the PBR for both Li and Mg oxides is <1 but 1-2 for LiOH, $Mg(OH)_2$ and Li_2CO_3 and 2.04 for $MgCO_3$ (table 2.1), several combinations of protective layers are possible [108]. While Li et al. [165] ascribe the low corrosion rate to a $Mg(OH)_2$ layer with additional Li components such as LiOH closing the otherwise porous structure, Yan et al. [162] claim a reduced formation of $Mg(OH)_2$ due to a more stable MgO layer formed because of additional Li doping. The doping with Li lowers the chemical reactivity and increases the PBR. Since the PBR for MgO is 0.8 before doping but changes to >1 if a minimum Li doping of 15-18 at% is reached, this would be in agreement with a change in passivation

mainly in β-phase materials [162].
Other measurements show C signals in the outer layer. Li_2CO_3 is widely discussed to form on β-MgLi and influence the corrosion [40, 163, 166]. However, in the case of, e.g., Yan et al. [161], the Li_2CO_3 layer can also be attributed to the storage in air. The reaction of Li into additional compounds leads to a depletion of Li in the area underneath the passivating layer. Thus, the material can change into α-phase in the zone directly under the surface [40, 161, 162].
Since the discussion of whether Li_2CO_3 is even formed during corrosion or is mainly a product of the fast reactivity of Li in contact with air is a widely debated point, it will be discussed in more detail separately.

2.3.5 Li_2CO_3 formation

Especially for β-MgLi, an ongoing discussion of whether Li_2CO_3 is formed in corrosion and reducing the corrosion rate in comparison to α-MgLi takes place. It is found on the surface of samples before and after corrosion and has a PBR of 1.35, indicating a possible stability [108].
For high Li fractions, a large amount of Li is available close to the surface and can readily react. Additionally, further Li can diffuse easier to the surface for β-phase since the diffusion coefficient of Li in β-MgLi is found to be higher than in the α-MgLi [82, 83]. In α-phase a coefficient dependent on the Li fraction and temperature but relatively independent on the direction in the structure is determined [83, 167].
The study by Yan et al. showed an increased thickness of the Li_2CO_3 film over time in air [168], indicating a continuously ongoing reaction to the carbonate. Tests of Li-free alloys in dissolved Li_2CO_3 also showed a reduction of filament-like corrosion with Li and carbonate components found on the surface afterwards [169]. Since carbonate is, in general, present under physiological conditions, similar reactions could be possible on MgLi [163].
However, other studies emphasise that the PBR would propose a stable layer independent of the Li fraction [150]. Even though less Li is available, a formation and diffusion of Li to the surface, possibly also over the grain boundaries with increased Li fraction, could occur. This would contradict the start of Li_2CO_3 formation as the influence on the lowest corrosion rate for β-phase.
Additionally, several studies found that Li_2CO_3 is dissolved when samples come into contact with aqueous solution, even if carbonate is present in the solution itself [162, 170]. This is due to the relatively high solubility of Li_2CO_3 in water (see table 2.1 for comparison to other components). The presence of Li_2CO_3 in measurements before and after corrosion might, therefore, be attributed to storage in air before each measurement, while other components such as MgO doped with Li [162] have the actual effect on reduced corrosion rate.
However, other studies claim to have measured Li_2CO_3 during in-situ measurements or in near in-situ studies after long immersion times [166, 170]. The stability of Li_2CO_3 in solution is dependent on the pH and Li concentration present in solution [112]. Therefore, since corrosion can increase both pH and concentration due to a high reactivity at the beginning, the formation of Li_2CO_3 becomes more likely over longer immersion times. Since the concentration will be increased for β-phase material, the formation on the bcc material could be favourable, however, no final decision can be found with the research

available.

2.4 Corrosion measurement techniques and feasibility for MgLi thin film measurements

The quantitative analysis of the corrosion rate can be done by measuring either 1) the loss of material of the sample or 2) the gain of released material (ions, electrons, gas). Several techniques have been developed in the past [105, 171], and a few main techniques will be described with an additional discussion regarding their relevance for defining the corrosion rate of Mg, MgLi and, more specifically, thin films.
It has to be noted that the measurement parameters, such as time frames or additional activation by, e.g., voltage application, lead to differing corrosion rates from methods that cannot be directly compared. Especially the definition of which material counts as corroded can change the corrosion rate. While some methods measure released ions, others include the corrosion products formed in the sum of released material, therefore changing the value.
These factors often lead to corrosion rates which are lower for electrochemical measurements (e.g. potentiodynamic polarisation) than weight-loss or hydrogen-evolution studies [172, 173] but the differences can also give further insights into the corrosion process and thus provide additional information.

2.4.1 Weight-loss measurements

The first possibility to define a corrosion rate is by measuring the weight loss of a sample during immersion time since (a part of) the material is dissolved during corrosion. Weight-loss measurements are carried out by measuring the mass of samples before and after immersion [105, 171]. The corrosion rate, often described in mm/yr, can then be calculated from the corroded mass m and time t by taking the surface area A and density ρ of the material into account.

$$CR = \frac{m}{t \cdot A \cdot \rho} \tag{2.1}$$

Weight loss measurements need longer immersion time to identify a significant weight change and can be carried out in a solution relevant to the application. In the experiments described in the publications of this work, a salt solution (HBSS, H1387, Sigma-Aldrich, with added sodium bicarbonate, 155 mmol) with a pH of 7.4±0.2 controlled by CO_2 gas regulation and a temperature of 37±1 °C is used to work at conditions similar to physiological conditions. The longer immersion leads to measurements closer to equilibrium conditions than electrochemical techniques, which will be discussed in section 2.4.3.
While first challenges can arise due to a non-exact definition of the surface area due to roughness changes and - in the case of MgLi thin films - only a few values of bulk materials for the density, the estimation of a corrosion rate could be determined. A main challenge is caused by the obligatory cleaning step after immersion. In general, samples are cleaned in mainly chromic acid after immersion to remove any corrosion products

formed on the surface, which would increase the weight, possibly even to a mass larger than before immersion. Since the definition of corrosion for weight loss measurements includes the material which reacted from the metal to corrosion products, this weight has to be removed. Even though this is a standard praxis for Mg alloys [105, 171], the measurement on thin films is complicated. In addition to the small weight loss and, thus, minor change in weight by the corrosion itself, the cleaning step can change the surface of Mg alloys slightly (see figure 2.6) and, therefore, change the determined corrosion rate. While the small influence of chromic acid on the surface does not affect the corrosion rate significantly for larger samples with larger volumes and more difference in weight between starting material and corroded material, a careful cleaning to avoid larger influences has to be performed if weight loss measurements are used for thin film samples of Mg alloys. The immersion times of thin films are also often short to avoid a pitting through the film during measurement since the calculations assume homogeneous corrosion and do not include such phenomena [108]. Alternatives of cleaning processes, e.g. in ultrasonic baths, were also developed [174] to remove any corrosion products from Mg but were not used in this work.
If surface films or treatments which alter the sample to oxide or carbonate-containing compounds are added, the studied minor weight loss cannot determine the corrosion rate accurately due to problems in identifying the reaction to surface films and the differentiation of the removal of corrosion products or such films.

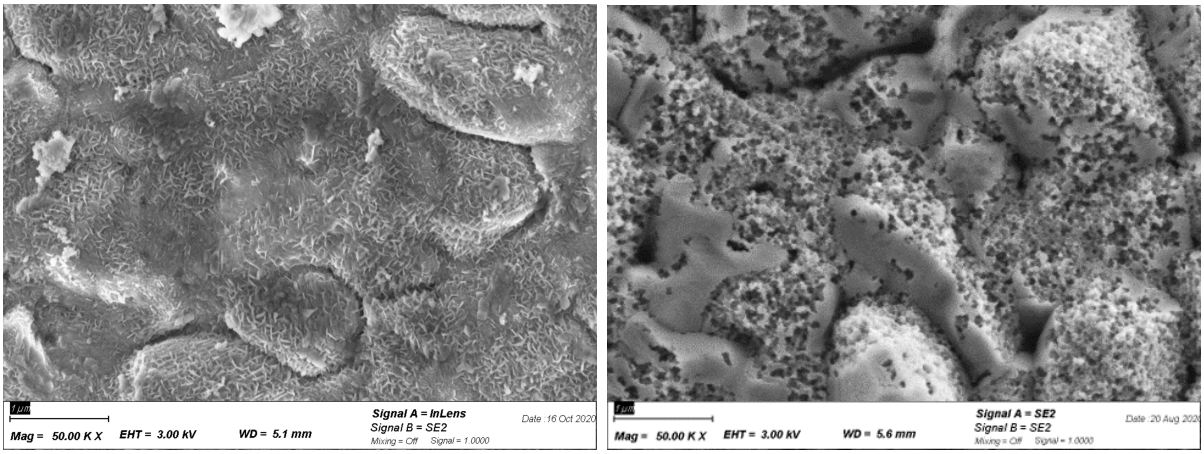

(a) (b)

Figure 2.6: SEM images of Mg-3(wt%)Li thin films before and after treatment with chromic acid.

2.4.2 Hydrogen evolution

In addition to the loss of material from the sample, the products of the corrosion reactions can also be measured. During the reduction, hydrogen gas is produced and can thus be used to determine the rate of corrosion [118, 175]. The sample is placed in a solution under a funnel that directly connects to a tube of a burette to determine the volume of developed H_2. While this method thus only uses a very simple set-up and measurements can be carried out at different time points throughout the degradation, problems can arise for samples with low corrosion rate and in physiological salt solutions for which the H_2

evolution can differ significantly from the determined corrosion rate by other methods [118, 171]. Even though H_2 is also produced for thin films and the corrosion rate is not necessarily low, the small amount of area and corrosive material only produces low amounts of gas, which are more difficult to detect and can lead to further differences in the detected corrosion rate to, e.g., weight loss measurements (exemplary visible in [31]). Therefore, the hydrogen evolution is not used for determining the corrosion rate in this work.

2.4.3 Potentiodynamic polarisation

Electrochemical measurements such as potentiodynamic polarisation allow estimating long-term corrosion rates in relatively short measurements [171].
A three-electrode set-up including working, counter and reference electrode is used. For the experiments described in this work, the sample is placed in a holder with an opening on one side with an area of 0.916 cm^2 as the working electrode [176]. Additionally, a Pt mesh as a counter electrode and an Ag/AgCl reference electrode (reference electrode with 3 mol/l KCl solution) placed in a Luggin capillary are chosen. The open circuit potential E_{OCV}, often also described as corrosion potential, of the sample can then be measured between the sample and reference electrode when no additional voltage is applied. This is the potential where the cathodic current equals the anodic current [103 d]. Figure 2.7 shows the set-up used in the following studies. Since the surrounding should model physiological conditions, these measurements are carried out in HBSS under temperature and pH control similar to the weight loss measurements.

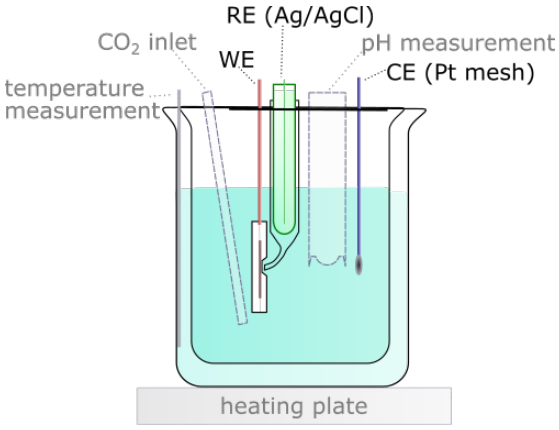

Figure 2.7: Schematic set-up for potentiodynamic polarisation measurements with a three-electrode set-up including the sample in the sample holder as the working electrode (WE), a reference Ag/AgCl electrode (RE) and a Pt mesh counter electrode (CE).

A voltage can be applied to enhance the corrosion kinetics. By measuring the current while applying a continuously increasing voltage starting in the cathodic region and reaching into the anodic region, the change in current with potential can be measured. The corrosion rate CR is defined by the change in thickness d over time t. By using Faraday's

law, this can be written as [176]:

$$CR = \frac{d}{t} = \frac{M}{n \cdot F \cdot \rho} \cdot i_0 \tag{2.2}$$

with the density ρ, the Faraday constant F, electrons released per atom n and the molar mass M and corrosion current density i_0.
The current density is described by the Butler-Volmer equation as [177, 178]

$$i = i_0 \left(e^{\frac{\alpha \cdot n \cdot F \cdot \eta}{RT}} - e^{-\frac{(1-\alpha) \cdot n \cdot F \cdot \eta}{RT}} \right) \tag{2.3}$$

The exchange current density or corrosion current density i_0 is influenced by the rate and surface concentration of the reduced and oxidised species [177]. α is defined as the transfer coefficient and η is the overpotential, thus, $\eta = E - E_{\mathrm{OCV}}$. Additionally, temperature T and gas constant R are included.

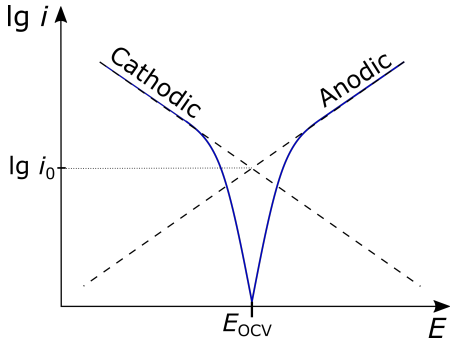

Figure 2.8: Schematic of a potentiodynamic polarisation measurement, depicted as a Tafel plot.

The current measured is often plotted logarithmically in a so-called Tafel plot (figure 2.8). If either the anodic or cathodic overpotential is high, the other reaction is negligible, leading to a linear equation and a straight line in the plot if the graph is plotted logarithmically. [179]

$$\lg(i) = \lg i_0 + \frac{\alpha \cdot n \cdot F}{2.3 \cdot R \cdot T} \cdot \eta \tag{2.4}$$

$$\lg(i) = \lg i_0 + \frac{(1-\alpha) \cdot n \cdot F}{2.3 \cdot R \cdot T} \cdot |\eta| \tag{2.5}$$

The crossing point of the linear branches at E_{OCV} thus, theoretically directly defines i_0, and the CR can be determined. In addition to the corrosion rate, the plots can also show a plateau due to passivation followed by a sharp increase in current at a certain potential, indicating a start of pitting in anodic measurements when the passivating film starts to develop defects [103 e, 32].
While this measurement, thus, theoretically gives insight into the corrosion rate and formation of passivating films, some factors have to be taken into account for Mg alloy

corrosion. The measurement generally does not show corrosion in a non-disturbed system and varies significantly from the corrosion rate of weight loss or hydrogen evolution [180]. One problem is also the assumptions for the Tafel extrapolation, which only describes one reaction occurring for each branch. In praxis, this does not hold true, especially considering the NDE, which, together with the formation of oxides and hydroxides, often prevents a crossing of both linear extrapolations at E_{OCV} [118, 180–182]. The hydrogen evolution and formation of bubbles on the sample surface can further influence the results [183], especially considering small measurement areas as often used for the thin film samples.
However, an extrapolation from the cathodic branch can be used to estimate a corrosion rate and compare different samples placed in the same set-up [180, 184].

2.4.4 In-line ICP-MS

During the corrosion in solution, the sample itself gets dissolved. Therefore, additional information regarding the corrosion rate and, even more importantly, about the specific released element can be determined by analysing the dissolution product in the electrolyte.
Samples of solution with dissolved species can be analysed by techniques such as inductively coupled plasma - mass spectrometry (ICP-MS) or inductively coupled plasma-atomic emission spectrometry (ICP-AES, also called ICP-OES, OES = optical emission spectrometry) to determine, e.g., catalyst loading, stability of partially metallic catalysts or the concentration in solution after a defined duration of corrosion [66, 79, 185–187]. However, this only gives the integral information over time between measurements. Based on previous measurement techniques [188], an in-line technique was presented by Ogle and Weber in 2000 [189]. The AESEC (atomic emission spectroelectrochemistry) combines ICP-AES with an electrochemical flow cell upstream in which the sample is added as the working electrode. Thus, the dissolved elements can be directly analysed downstream and during electrochemical measurements. Similar set-ups with ICP-MS have been developed [185, 190, 191], and both types are used for the study of time-resolved corrosion or catalysis [185, 188, 192]. Both will be discussed; however, the main focus is on the technique used for studies in this thesis, thus, a combination of the flow cell with ICP-MS.
In both cases, the system consists of the flow cell - a cell with defined sample surface in contact with solution and defined volume over the sample through which the electrolyte is pumped with a defined speed -, the spectrometer and the data acquisition system. Multiple important parameters have to be taken into account during the measurement. While, e.g., the flow rate can be determined to compare the ion release of different samples measured with slightly differing rates, this rate will also directly influence the corrosion process by, e.g., hindering precipitation, changing passivation layers or pH changes [188, 193–195]. The flow cell includes a three-electrode set-up with a counter electrode and reference electrode. In figure 2.9, the set-up of the flow cell [196, 197] described in this work is shown. In the ICP-MS system, the electrolyte is converted into an aerosol in the nebuliser by Ar flow and then transported into the spray chamber, from which only a few droplets will be transferred into an Ar plasma to bring the elements into the gas phase and ionise them. Afterwards, the ions are passing into a vacuum chamber for mass determination. Here, at first, any remaining neutral particles are separated from the ions, and the beam is focused before it reaches a collision/reaction cell. In this cell, any ions

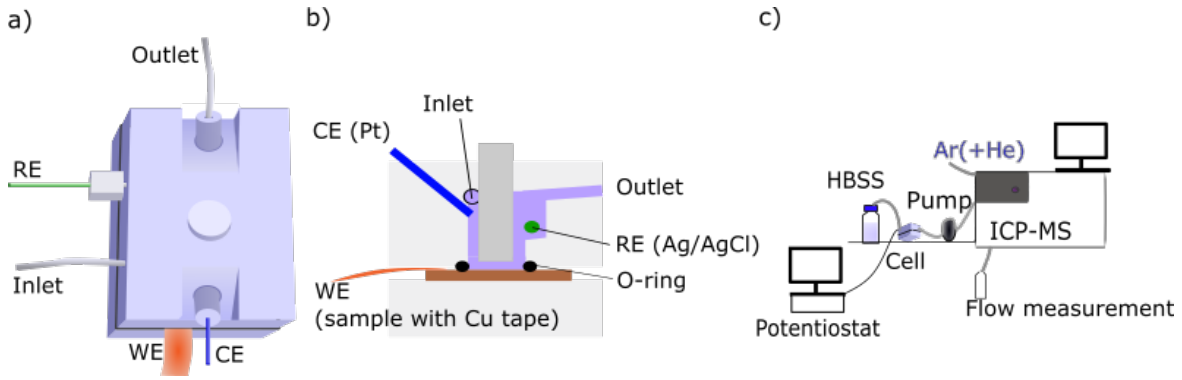

Figure 2.9: Schematic of flow cell as described in [196, 197] and inline ICP-MS measurement. a) Flow cell as used for the measurement of Mg alloy samples, including a Pt counter electrode (CE), reference electrode (RE) and the sample as a working electrode (WE), connected by copper tape. b) Cross section of flow cell. c) Overall set-up with solution flow through the flow cell to the ICP-MS.

including multiple atoms are split, in the case of the machine used in this work (Agilent 7900 ICP-MS) by collision with He atoms. The quantification dependent on the mass takes place using a quadrupole mass spectrometer in high vacuum to avoid recombination. While ICP-MS allows the quantification of isotopes and detection down to a limit of ppt (parts per trillion), the electrolyte needs to be much more diluted than for ICP-AES. [185, 188]
The dissolution rate j_m is then defined by the concentration $c(t)$ after calibration, the flow rate f of the electrolyte and the area of sample A in contact with said electrolyte [185, 188]:

$$j_\mathrm{m}(t) = f \cdot c(t)/A \tag{2.6}$$

To calculate the dissolution current density i, the Faraday constant F, electrons released per atom n and the molar mass M are taken into account

$$i(t) = j_\mathrm{m}(t) \cdot n \cdot F/M \tag{2.7}$$

While this current density (if it is added up for all elements) can, in theory, be compared to the results of, e.g., potentiodynamic polarisation if a voltage sweep is performed in the flow cell (e.g. [182]), the influence of side reactions, signal broadening and transfer time from flow cell to ICP-MS need to be taken into account [182, 188, 189].
By applying a potential or current, a change in composition during and after passivation regions can also be determined. The combination with the flow cell and identification of each element individually, thus, makes the identification of the stoichiometry of dissolved elements possible. Therefore, selective dissolution due to dealloying, preferential corrosion, film formation during corrosion, or catalytic reactions can be measured time resolved. The combination with electrochemistry also helps to receive information not directly available from ICP-MS, such as the oxidation state of the elements after corrosion [185, 188].
Several studies by both in-situ ICP-MS and ICP-AES have been carried out for further understanding the corrosion process and protective layers during corrosion. The system also allows to analyse the ion dissolution during other electrochemical measurements [198] or reactions under additional influences such as, e.g. light or scratching [185, 191, 196,

199, 200].
The techniques were used for several studies on Mg and MgLi. For Mg corrosion, studies by Thomas et al. investigated the influence of impurities of Fe, proving an increase in activity [201]. The influence of a pH change and applied anodic potential was tested by Rossrucker et al. [110, 182], showing a lower NDE for low polarisation and high pH. Compared to ex-situ measurements, the dependence on time and change after applying anodic polarisation can be directly observed. For Mg corrosion, earlier studies suggest the possibility of the formation of Mg^{+} additional to Mg^{2+} as a reason for the NDE occurring for Mg, however, analysis by Świątowska et al. [117] and Lebouil et al. [115] showed only Mg^{2+} and rather suggested the growth of cathodes by corrosion product formation if an anodic potential is applied. This also leads to an improved stability of the dissolution after anodic polarisation when the sample is held at E_{OCV}. The formation of hydrogen gas can be identified as noise in the measurements [117].
For MgLi, specifically with high Li content (β-phase), the composition of a passivation layer formed during corrosion was analysed by determining the change in stoichiometry when applying an increasing voltage and scratching the surface [162, 166, 200], showing, e.g., a preferred Li dissolution after the scratch in the study by Yan et al. [200]. Hou et al. found a greater Mg:Li ratio in the dissolved ions than in the material itself and determined the presence of Li_2CO_3 by a change to a ratio similar to bulk when the voltage is increased over a certain threshold [166]. However, Yan et al. [162] did not find the same difference in ratio but rather found a Mg-rich layer determined by Mg-rich particles released after scratching.
For the studies of thin films, the possibility to gain insight into the start of the corrosion in-situ is especially important since the surface affects the overall sample properties significantly due to the high surface-to-volume ratio. Additionally to thin films on substrate, free-standing thin films can also easily be placed into the flow cell, however, special care has to be taken to prevent corrosion mainly as crevice corrosion when the thin film is bent around the O-ring [197].
Since the dissolved ions are directly detected, no effects such as the NDE can influence the assumed corrosion rate compared to the actual ion release. Since the detection limit is very low, there is also no effect of concentrations that are too low due to the thin films, especially since, in any case, the technique analyses in short time frames, and thus, no long-term accumulation of corrosion products is necessary. It also allows for the identification of light elements such as Li, therefore allowing the studying of nearly any Mg alloys.
While the technique can be used for longer in-situ experiments, the measurement times for thin films are limited to prevent crevice or pitting corrosion through the whole film to avoid contact between the electrolyte and the substrate material or sample holder additional to the sample. Thus, no long-term corrosion properties are analysed. Since the machine is very sensitive, the electrolyte needs to be adjusted. While the corrosion rates were mainly determined in HBSS (155 mmol) at a pH of 7.4±0.2 and a temperature of around 37±1 °C (see 2.4.1, 2.4.3) to simulate physiological conditions, for the in-situ measurements, the concentration was adjusted to 15 mmol HBSS during the experiments for this work. The pH was close to 7.4 but no temperature control was applied. This is, however, possible by, e.g., a water bath heating [188].
In-line ICP-MS might not be necessary to determine the corrosion rate, which can be done with less effort with other techniques, but it provides a further understanding of corrosion processes and element-dependent dissolution of MgLi thin films.

2.4.5 Further measurements

While several techniques have been discussed to determine the corrosion rate and analyse the corrosion process, those often need to be combined with additional measurements [105]. Those can be used for studying the surface pre- and post-corrosion to investigate a change in surface composition by, e.g., formation of corrosion products (e.g. SEM/EDX (scanning electron microscopy/energy dispersive X-ray spectroscopy), XRD (X-ray diffraction), XPS (X-ray photoelectron spectroscopy)), or change in surface morphology (e.g. AFM (atomic force microscopy), SEM) for defining the overall change during corrosion. Additional measurements such as EIS (electrochemical impedance spectroscopy) can give further insight into the electrochemical processes taking place at different time scales and help to identify the formation of corrosion layers. Thus, since the corrosion of Mg and Mg alloys in aqueous solution and especially in more complex electrolytes is a complex system, no single technique can give all results necessary to understand the ongoing process.

3 Results

To analyse the viability of MgLi thin films as a local drug reservoir for the treatment of neurological disorders, in the following studies and chapters with additional experimental results, the fabrication, structural properties and corrosion rate of MgLi thin films with varying Li content will be discussed. In addition to the general test of the properties of such alloys, the studies opt to further understand the corrosion, the influence of participating parts such as phases, Li content, microstructure, orientations or surface films on the corrosion rate and a more detailed corrosion process and ion release will be described. This not only provides a more thorough understanding of the underlying mechanisms occurring but also allows the understanding of adjustments to the corrosion rate by changing the sputtering parameters or applying additional post-treatments.

3.1 Publication: Structural characterisation and degradation of Mg-Li thin films for biodegradable implants

To develop MgLi thin films for medical treatments, freestanding films of the alloys have to be prepared and studied. In this work, thin films in α and α+β-phase were fabricated by magnetron sputtering with low film stress. The microstructure and phases were analysed, showing not only β-phase for higher Li fractions but also additional Li_2CO_3 and a change in orientation. In mechanical tests, a lower tensile strength was found for all MgLi compositions compared to pure Mg, and the maximum elongation was reduced except for samples with the lowest Li fraction. While the corrosion rate increased for an increase in Li fraction in the α-phase due to higher reactivity and the influence of orientation changes, a lower corrosion rate was found at high Li fraction in the mixed phase, indicating a possible effect of protective surface films.

Own contributions to the following article
(concept - 50 %, planning - 75 %, experiments - 75 %, analysis - 90 %, writing - 90 %):

- Sample preparation and preparation optimisation
- XRD, SEM and EDX investigation
- Tensile testing, weightloss and potentiodynamic polarisation measurements
- Interpretation and discussion of the results
- Writing of the manuscript

www.nature.com/scientificreports

scientific reports

Check for updates

OPEN

Structural characterisation and degradation of Mg–Li thin films for biodegradable implants

Lisa Hanke[1], Lea K. Jessen[1], Felix Weisheit[1], Krathika Bhat[2], Ulrike Westernströer[3], Dieter Garbe-Schönberg[3], Regine Willumeit-Römer[2] & Eckhard Quandt[1]✉

Freestanding thin films of Mg–Li (magnesium–lithium) alloys with a Li mass fraction between 1.6% (m/m) and 9.5% (m/m) were prepared and studied with respect to their structure and degradation properties. With increasing Li content, the microstructure deviates from hexagonal Mg–Li with strict columnar growth and preferred orientation, and additional cubic Mg–Li and Li_2CO_3 occur. The corrosion rate was measured in Hanks' balanced salt solution by potentiodynamic polarisation and weight loss measurements to investigate biodegradation. Influences of the orientation, phase and protective layer formation lead to an increase in corrosion from 1.6 to 5.5% (m/m) from 0.13 ± 0.03 to 0.67 ± 0.29 mm/year when measured by potentiodynamic polarisation but a similar corrosion rate for 9.5% (m/m) and 3% (m/m) of Li of 0.27 ± 0.07 mm/year and 0.26 ± 0.05 mm/year.

Magnesium and its alloys are widely studied as materials for applications in the medical field due to their biodegradability. Different elements such as, e.g., Ca, Zn or rare earth elements (REE) are included to improve mechanical properties or tailor the degradation rate to adjust them for applications as, e.g., stents or bone implants[1–4]. Additional to the advantage of having an implant which degrades after it is no longer required, the possible therapeutic effects of the implants are explored by, e.g., loading stents with drug-eluting layers[5] or using the corrosion process and changes in the environment such as pH and hydrogen evolution directly for its antibacterial properties[6].

In line with the idea to use the implant itself as treatment, an alloy including the therapeutically active element lithium will be analysed in this study. Lithium is used in treatments for mood disorders, in particular bipolar disorder, and is also studied to have effects on Alzheimer's and Parkinson's disease[7–10]. Magnesium itself shows also neurological effects[11]. Therefore, the degradation and, thus, continuous release of both the magnesium and additional elements would allow a local treatment in the brain. If a controlled and local release is achieved by understanding the degradation of the material, side effects which can occur during the treatment with Li[12] could be reduced.

For Mg–Li, the structure in bulk materials differs from pure Mg by a reduction of the distance in *c*-direction and a phase change to a body centred cubic (bcc) phase (β phase) for higher Li fractions (Mg–Li phase diagram, Fig. 1 [13]). This change leads to additional non-basal slip on the prismatic planes, twinning, and more ductile properties even in hcp Mg–Li alloys. For higher Li fractions, the addition of the second phase can significantly change the mechanical properties. Li et al. showed that cracks are preferably formed at the phase boundaries which is facilitated by the difference in the number of gliding systems present in both phases and, thus, a difference in stress accumulation[14]. Additionally, the ageing of the second phase and change from bcc to hcp phase even at room temperature influences the properties over time[14,15].

The corrosion rate of Mg–Li alloys is influenced by several factors such as the high activity of Li, change of microstructure and surface films. The low electrochemical potential of Li leads to an increase in the cathodic kinetics and a more significant shift of the pH. Filiform corrosion is found to be one of the main corrosion processes occurring for Mg–Li alloys in the α or α + β materials[16–18]. For films with mixed phases, micro-galvanic coupling is found as a main factor for an increase in corrosion rate with preferred corrosion and pitting at the phase boundaries[19,20]. However, the diversity of microstructure and protective layers formed during corrosion makes a clear indication of the influence of the different factors on the corrosion rate difficult. Li et al. showed that the corrosion rate decreases from α + β > α > β[18]. The lower corrosion rate of the bcc phase is assumed to be

[1]Inorganic Functional Materials, Institute for Materials Science, Faculty of Engineering, Kiel University, Kiel, Germany. [2]Institute of Metallic Biomaterials, Helmholtz Centre Hereon, Geesthacht, Germany. [3]Marine Climate Research, Institute of Geosciences, Faculty of Mathematics and Natural Sciences, Kiel University, Kiel, Germany. ✉email: eq@tf.uni-kiel.de

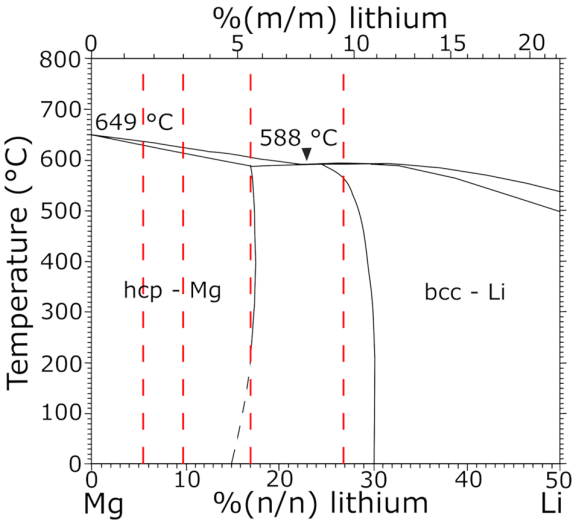

Figure 1. Mg–Li phase diagram, adapted from[13]. The region with a Li fraction from 0 to 50% (n/n) is depicted and the concentration of sample films (Li mass fraction of 1.6% (m/m), 3% (m/m), 5.5% (m/m) and 9.5% (m/m)) are marked. Low Li concentrations lead to a Mg rich α-phase with a hcp structure and high Li concentrations to a β-phase with a bcc structure. In the mixed phase regions, α-phase and β-phase are formed.

due to the high density and stability of a formed protective layer. While for the Mg rich phase, mainly a porous $Mg(OH)_2$ layer is expected to form during corrosion[21,22], the layer structures of surface films formed on Mg–Li including the bcc phase are complex. Xu et al., e.g., analysed the structure of the natural film formed in air as a Li_2CO_3 film on the surface, Mg oxide and Li oxide film underneath and Mg-rich film before the bulk material[23]. Other studies claim for films formed in air or during corrosion several compounds including carbonates, oxides and hydroxides of both Li and Mg, often separated in a layer structure[16,24,25]. Previous studies assumed or suspected that the formed Li_2CO_3 has the main influence on the higher corrosion resistance of the bcc phase[23,26,27]. The Pilling–Bedworth ratio (PBR), which is a measure for film stress and, thus, identifies a stable film for $1 < PBR < 2$, is > 1 for all Mg:Li ratios for Li_2CO_3. Thus, it could already be formed for lower Li mass fractions in the hcp phase[18]. Yan et al. suggest another possible influence as Li doping and therefore strengthening the MgO and hindering the formation of the more porous and less protective magnesium hydroxide. Since the critical Li fraction for forming a stable layer of MgO is calculated to be around 15–18 at. % (4.8–5.9%(m/m)), this is in agreement with the formation of the layer only on Mg–Li with β or α + β[28]. Therefore, with the assumption of the formation of a stable MgO layer by Li doping, the higher Li fractions leads to a decrease in corrosion rate by changing the film stress.

However, it has to be noted that the corrosion of Mg–Li with different phases is a complex system, leading to other studies showing the lowest corrosion rate for the hcp phase[19]. The main influences on the actual corrosion rate are therefore not just Li content and phases but also the microstructure of the material.

For neurological implants, small freestanding films and structures in the sizes of a few µm–mm are needed. Previous to this paper, no extensive studies of Mg–Li thin films regarding the growth and properties are available to our knowledge. As found for thin films of other Mg alloys, significant influences on the properties in comparison to bulk materials are expected. For different Mg alloys such as Mg–Ag or Mg–REE, the structure of thin films was studied[29–33]. For sputter-deposited films, the hexagonal close packed (hcp) magnesium phase (α phase) is strongly textured with a preferred growth direction of [001] and a columnar grain structure is apparent[31,33–35]. The strong texture influences the deformation by, e.g., reducing work hardening and influences therefore the mechanical properties[33]. The corrosion of thin films in comparison to bulk is shown to be more homogeneous with less effect of pitting[35,36]. Additionally, the corrosion resistance and oxidation of different planes are different due to the packing and binding energies, thus, the corrosion rate is influenced by the texturing of the films[37]. The (001) plane is found to show the lowest corrosion rate due to the densest packing, however, since the faster oxidation of other planes could lead to a protected surface, the actual influence on the corrosion rate cannot be directly predicted[38,39]. Since the properties are highly dependent on structure and microstructure, they can be influenced for the same alloy by changing the sputtering parameters, leading to higher densities or differences in the film growth depending on the energy available for diffusion of the atoms[29,32,40–42].

In this study, Mg–Li thin films with a pure hcp or an α + β structure (Mg–Li phase diagram, Fig. 1) are prepared via magnetron sputtering. To gain insight into the corrosion process dependent on the specific structure present in the thin films, studies with respect to their growth and microstructure are carried out to allow a correlation with influences on the corrosion rate. Additionally, the possibilities to influence and tune those to meet specific requirements given for applications are discussed.

Results

Composition and microstructure. The compositions of the prepared Mg–Li thin films are marked with red dashed lines at mass fractions of 1.6% (m/m), 3% (m/m), 5.5% (m/m) and 9.5% (m/m) in the phase diagram in Fig. 1 (fractions given in Supplementary Table 1). As shown, two sample types are prepared with Li mass fractions leading to pure hexagonal phase, while the other two theoretically consist of α and β phase with approximately 89% (Mg–5.5Li) or 22% (Mg–9.5Li) α phase.

Very low iron contaminations are measured for all film compositions. Representative XRD diffractograms for all compositions are displayed in Fig. 2a in comparison to pure Mg prepared by the same procedure. While pure Mg exhibits a strong texture with a main peak of (002) at 34.3°, including 1.6% (m/m) Li leads to less preferred growth and for Mg–3Li, a random orientation is identified (Supplementary Fig. 1). For both materials in the α + β phase, the hexagonal phase shows a preferred orientation of (110). Additional bcc can be identified as small peaks in the diffractogram, and additional studies of the reciprocal space allow the identification of strong (110) peaks for Mg–9.5Li at an angle of $\chi = 32°–40°$, indicating a strongly textured β-phase. While the lattice parameter *a* is only slightly decreased from Mg–1.6Li to higher Li mass fractions, *c* is reduced, especially for the increase of Li from 1.6% (m/m) to 3% (m/m) (peak shift in Fig. 2a, calculated lattice parameters in Supplementary Table 2). When the second phase is present, the parameters do not decrease further since the added Li is included in the additional phase. Of interest are as well the peaks at, e.g., 21.3°, 23.3°, 29.4° and 34.1° for Mg–5.5Li and Mg–9.5Li which indicate the existence of Li_2CO_3 (Supplementary Table 3). Because of the formation of this additional phase, the amount of β-phase is reduced.

Investigations via EDX show a layer including carbon and oxygen on the surface of Mg–9.5Li, thus, the Li_2CO_3 identified by XRD can mainly be assigned to a film formed on the surface of the samples when those are stored in air. The formation of Li_2CO_3 in humid air for β-phase Li is also shown in previous studies[23,28]. A layer of Li_2O is formed on the surface of alloys with high Li content and can react further to Li_2CO_3 if CO_2 is present in the surrounding atmosphere[23]. There is no significant compositional change over the layer thickness for, e.g., Mg–1.6Li (Fig. 2b). Cross-sectional images of the different Mg–Li alloy freestanding thin films with a thickness of 10 µm are given in Fig. 3a for analysis of the microstructure. Mg–1.6Li exhibits a columnar growth with a constant diameter of approximately 500 nm to 1 µm over the whole film thickness. This structure is also identified for pure Mg films with the strong (001) texture prepared via magnetron sputtering[30]. For Mg–3Li, smaller grains are formed close to the substrate while columns start after a few 100 nm with increasing diameter up to 1.5 µm to 2 µm with a few columns exhibiting a diameter of around 4 µm. Less columnar growth is visible for Mg–5.5Li and cannot be identified for the highest Li mass fraction. The surface, however, still exhibits a structure which leads to the identification of grain sizes of approximately 1.5–2 µm. The difference in the cross-sectional images can not only be assigned to a change of columns to a different microstructure because of additional phases but also to less preferred fracture at the grain boundaries during bending. This is influenced by, e.g., voids formed due to the self-shadowing of the columns. For Mg–9.5Li, oxidation of the samples also plays a major role in the visible structure since the samples are highly affected. While a thin oxide film is formed for all films and is apparent in the surface images in Fig. 3a, only for films with higher Li content (Mg–9.5Li) the oxide grows significantly until the film is completely oxidized (Fig. 2c).

To classify the microstructures further, they can be compared with the structure-zone model[41,43]. The substrate temperature during the deposition was (49–54) °C for Mg–1.6Li, (54–66) °C for Mg–3Li and (60–66) °C for

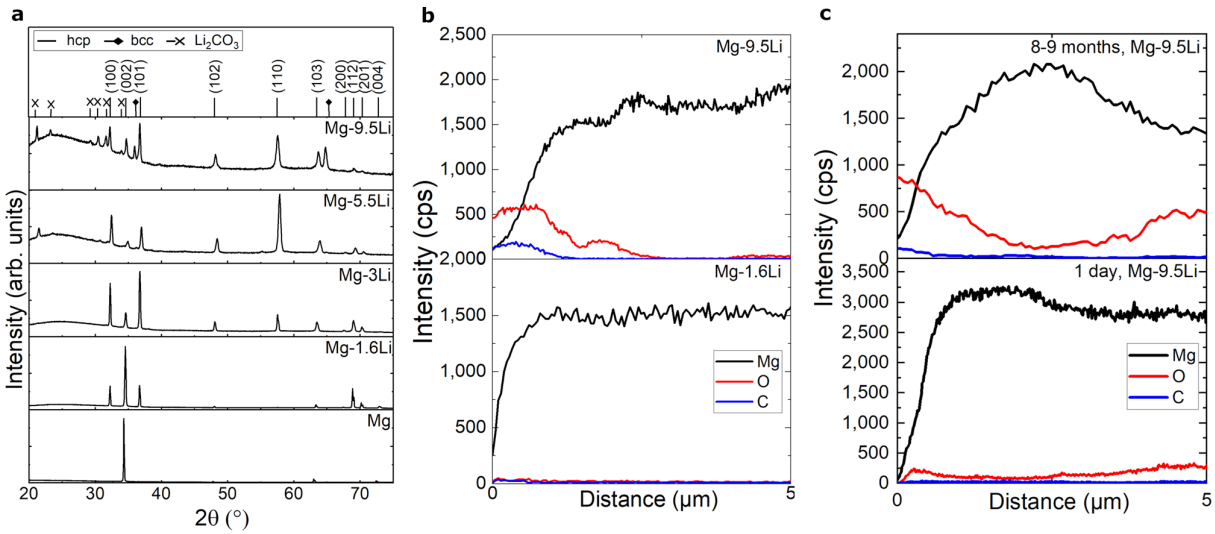

Figure 2. Structure and composition of freestanding thin films (**a**) XRD diffractograms for Mg, Mg–1.6Li, Mg–3Li, Mg–5.5Li, Mg–9.5Li thin films. The positions of the hcp and bcc Mg–Li phases and Li_2CO_3 are marked. Additionally, the orientation of the corresponding planes for the hcp phase are indicated, (**b**) EDX line scans of cross sections of Mg–1.6Li and Mg–9.5Li thin films as used for corrosion measurements, (**c**) EDX line scans of cross sections of Mg–9.5Li freestanding thin films after 1 day and 8–9 months.

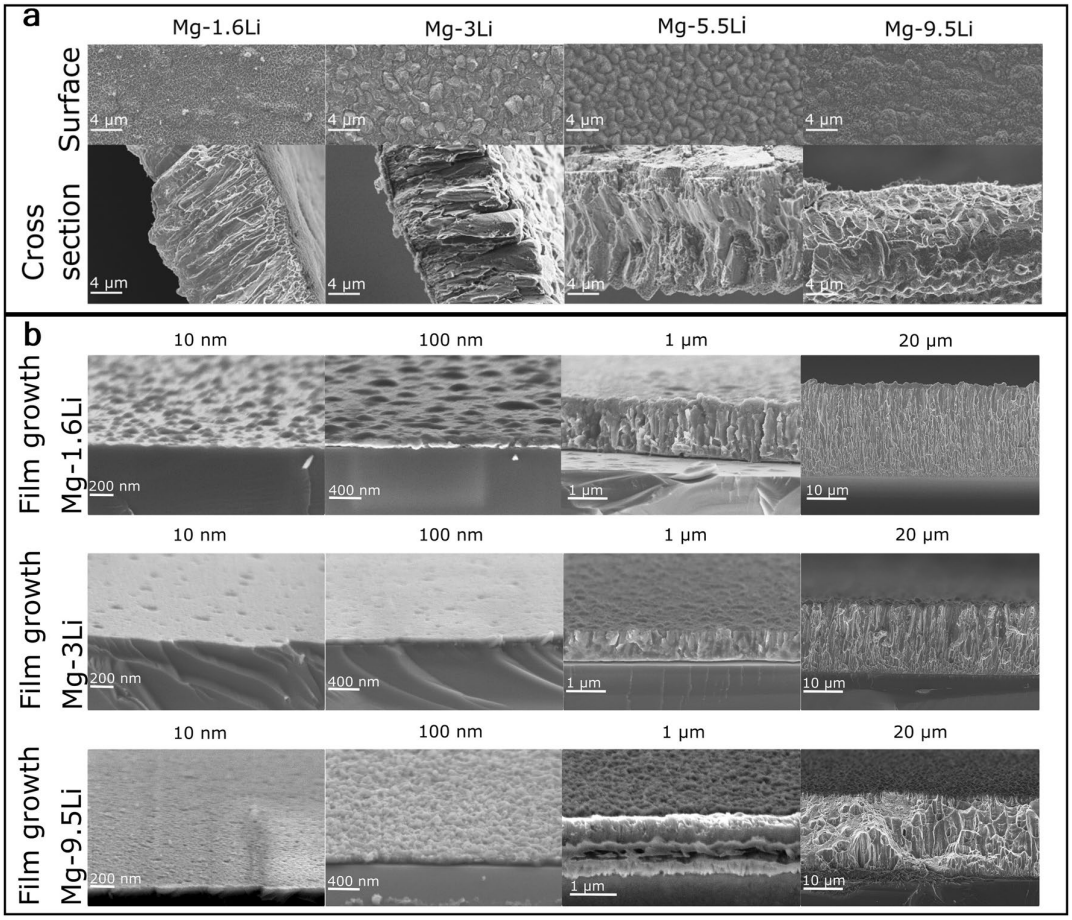

Figure 3. SEM images (**a**) Surface and cross-section of freestanding Mg–Li thin films. (**b**) Side view or cross-section of Mg–Li films (Li: 1.6% (m/m), 3% (m/m), 9.5% (m/m)) on Si substrate with thicknesses of 10 nm, 100 nm, 1 µm and 20 µm.

Mg–5.5Li and Mg–9.5Li samples. This leads to $T/T_m = 0.36$ for Mg–1.6Li and $T/T_m = 0.39$ for Mg–9.5Li as the highest and lowest possible values, leading in theory to structures in the T-zone, changing into zone 2. For higher zones, the grain boundaries get denser, and the defect density decreases, therefore fewer voids occur which could influence the fracture at grain boundaries. Additionally, a shift from straighter fibres to more complex structures at lower layers for Mg–3Li is in good agreement with the microstructural cross-sections.

Film growth. To identify and understand the differences in microstructure, the growth of Mg–1.6Li, Mg–3Li and Mg–9.5Li films is additionally analysed. The sputter times were chosen according to the sputtering rates for 10 µm to result in approximately 10 nm, 100 nm, 1 µm and 20 µm. The results are displayed in Fig. 3b.

The growth for the lowest Li mass fraction starts with island growth, similar to pure Mg[44]. The film covers the whole surface for a thickness > 10 nm, resulting in columnar growth. The energy of the particles from the sputtering process itself and the low temperature of the substrate do not allow sufficient diffusion for a more homogeneous growth[45]. The columnar growth is additionally in good accordance with the structure formed with the preferred orientation of (001) because the fastest growth for hexagonal faces is in direction of the c-axis[45].

The film growth process is studied to be highly influenced by including alloying elements[44]. For Mg–3Li, the layer formation starts with layer growth, including only few defects in a 10 nm thick layer. After approximately (400–500) nm, the growth changes to columnar growth. This change can be attributed to film stress which accumulates over the layer and changes the energetically favourable growth. Pores and voids can already be identified after the column growth for a layer thickness of 1 µm. Even though columnar growth is visible, the homogeneity of the signal on the reciprocal space mapping from XRD shows that a random orientation is formed throughout the whole film (Supplementary Fig. 1). Since the growth is not as strictly orientated as for Mg–1.6Li, it leads to an increase in column diameter and void formation.

For Mg–9.5Li, the film growth at the beginning cannot be directly identified as island growth, however, at a film thickness of approximately 100 nm, a grain-like surface with a high roughness is visible. Even though these samples were measured directly after preparation and the oxidation of the samples is thus minimal, a colour change of the samples showed a slight oxidation even for the fastest possible measurement and therefore

influences especially the thinnest layers. For the thick films, samples with only minor oxidation exhibit columnar structures. However, the sample is only partially breaking at the grain boundaries and, thus, the structure is less pronounced.

Tensile testing. The mechanical properties were studied by tensile testing perpendicular to the growth direction of the films. Since Mg–5.5Li freestanding thin films are very brittle, possibly partially due to oxidation, no tensile test measurement is possible. Thus, except for the poor mechanical stability, no further analysis of the properties is possible for this sample type. Exemplary stress–strain curves for the other tested Mg–Li alloys are shown in Fig. 4 and the strengths and elongations are listed in Table 1.

In comparison to pure Mg samples with the same sample shape and measured with the same set-up[30], adding Li lowers the tensile strength and especially the yield strength. For Mg, the main slip system is basal slip but pyramidal slip is also proposed to be available in a smaller amount due to higher energies[29,30,46]. For the (001) orientated samples, the alignment of the planes in one direction leads to a sharp change from elastic to plastic deformation. Including additional orientations hinders the gliding between grains, however, since not only the orientation but also the lattice structure is influenced by the addition of Li, this does not increase the tensile strength directly but increases the difference between tensile strength and yield strength. While the maximum strain for Mg–1.6Li is similar to pure Mg samples, it is decreased for Mg–3Li and Mg–9.5Li. Examination of the cross-section after tensile testing shows a moderately ductile fracture and no preferred breakage at the grain boundaries, therefore excluding this as a main influencing factor on the fracture mechanism during tensile test, even though Mg–1.6Li exhibits fracture at the grain boundaries during the fracture by bending.

Corrosion rate. Exemplary potentiodynamic polarisation curves for all studied Mg–Li alloys and Mg are shown in Fig. 5 after 5 min of immersion. For Mg, the intrinsic corrosion rate measured by weight loss measurements in concentrated chlorine solution of highly pure Mg ingots is 0.3 mm/year[47]. Similar values have also been found for high purity Mg in Hanks' balanced salt solution over long measurement times[48,49]. The corrosion rates of Mg–Li in this study will be compared to Mg thin films sputtered with the same technique and similar purity of the starting target to analyse the influence of Li on the structure and activity, and, thus, the change of corrosion rate. It has to be noted that pure Mg in this case is not actual ultra-high purity Mg which is proven to have a lower corrosion rate than the Mg used here which might include impurities[50].

Even though Li has a lower electrochemical potential than Mg thin films prepared by the same process[31], the corrosion potential E_{corr} is slightly increased for Mg–1.6Li, Mg–3Li and Mg–5.5Li, however, the difference to Mg is due to the high standard deviation not significant for Mg–3Li and Mg–5.5Li (Table 2). The highest E_{corr} is measured for Mg–9.5Li. However, the higher potential does not directly correspond to a decrease in corrosion

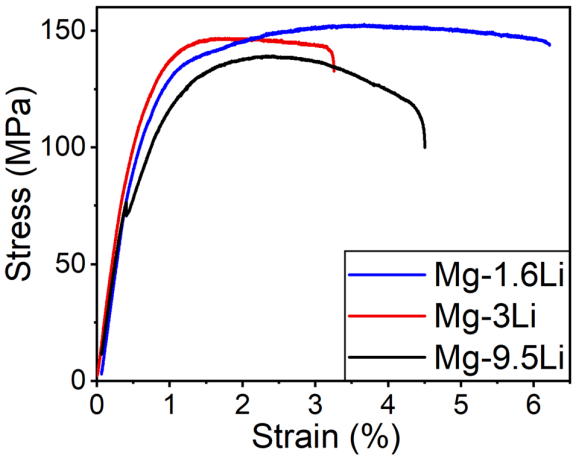

Figure 4. Exemplary stress strain curves of Mg–1.6Li, Mg–3Li and Mg–9.5Li dog-bone shaped thin films.

Mg–Li alloy	σ_{max} (MPa)	$R_{p0.2}$ (MPa)	ε_{max} (%)
Mg–1.6Li	148 ± 10	110 ± 10	6.1 ± 0.9
Mg–3Li	144 ± 10	116 ± 8	3.0 ± 0.8
Mg–9.5Li	138 ± 10	101 ± 20	3.4 ± 0.9
Mg[30]	171	153 ± 8	7 ± 4

Table 1. Average values and standard deviation of tensile strength σ_{max}, yield strength $R_{p0.2}$ and elongation at break ε_{max} in comparison to pure Mg samples[30].

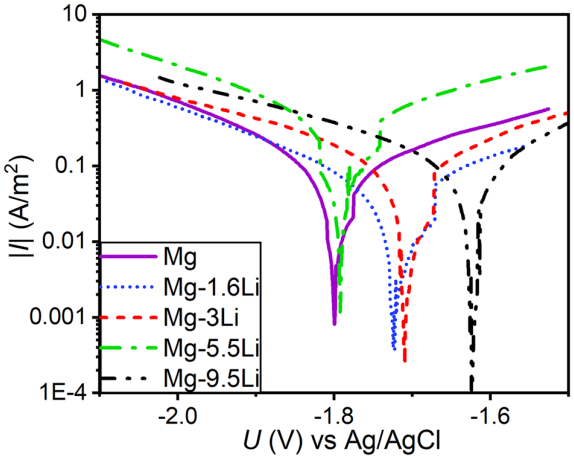

Figure 5. Exemplary Tafel plots obtained by potentiodynamic polarization measurements vs Ag/AgCl reference electrode in Hanks' balanced salt solution at a pH of 7.4 ± 0.2 and 37 ± 1 °C for Mg, Mg–1.6Li, Mg–3Li, Mg–5.5Li and Mg–9.5Li thin films.

	E_{corr} (V)	i_{corr} (A/m²)	CR_{EC} (mm/year)	CR_{WL} (mm/year)
Mg	− 1.81 ± 0.05	0.05 ± 0.01	0.12 ± 0.02	1.32 ± 0.37
Mg–1.6Li	− 1.73 ± 0.02	0.06 ± 0.02	0.13 ± 0.03	0.80 ± 0.14
Mg–3Li	− 1.76 ± 0.04	0.12 ± 0.04	0.27 ± 0.07	3.75 ± 0.68
Mg–5.5Li	− 1.77 ± 0.08	0.30 ± 0.13	0.67 ± 0.29	20.25 ± 0.33
Mg–9.5Li	− 1.63 ± 0.06	0.12 ± 0.03	0.26 ± 0.05	2.70 ± 0.38

Table 2. Corrosion potential E_{corr}, corrosion current density i_{corr} and corrosion rate CR_{EC} resulting from Tafel plots obtained by potentiodynamic polarisation and corrosion rate CR_{WL} measured by weight loss measurements after 2 h for Mg and Mg–Li alloys (Li: 1.6% (m/m), 3% (m/m), 5.5% (m/m), 9.5% (m/m)).

rate for this samples. The corrosion current densities i_{corr} and, thus, corrosion rates CR_{EC} are determined via Tafel extrapolation[51,52] of the nearly linear branches in Fig. 5 and listed in Table 2. The corrosion rate was calculated by the following equation using the determined i_{corr}, the molar mass M, Faraday constant F, number of electrons n and density ρ[52]:

$$CR_{EC} = \frac{i_{corr} \cdot M}{n \cdot F \cdot \rho}.$$

Even though the potentiodynamic polarisation thus does not measure the steady state of the corrosion, it allows a comparison of corrosion rates determined for the different MgLi alloys. While for Mg–1.6Li the current density is similar to pure Mg, it is doubled when increasing the Li content to 3% (m/m). Mg–5.5Li exhibits the highest corrosion current density with 0.30 ± 0.13 A/m². Of interest is the decrease in corrosion rate when increasing the Li mass fraction further to Mg–9.5Li which is similar to the corrosion rate of Mg–3Li.

To get further insight into the corrosion over time, weight loss studies are carried out over 2 h (Table 2). While the corrosion rate for Mg–1.6Li is lower than for pure Mg films, the same trend as for the electrochemical measurements with faster corrosion up to Mg–5.5Li and a corrosion rate of Mg–9.5Li similar to Mg–3Li is determined. Since for the weight loss measurements, the corrosion product is removed and, thus, included in the corrosion rate, this indicates that not only more material is transformed into a corrosion product layer and not released into the solution, but also that the corrosion of the material underneath is hindered. To understand the development of the corrosion rate over time, the weight loss measurements are repeated for Mg and Mg–1.6Li for 1 h and 4 h. After 1 h, the corrosion rates for both sample types are higher than after 2 h, and the difference between both sample types is even more pronounced with $CR_{Mg,1h}$ = 2.22 ± 0.37 mm/year and $CR_{Mg\text{-}1.6Li,1h}$ = 1.24 ± 0.15 mm/year. The corrosion rate after 4 h is similar for both materials ($CR_{Mg,4h}$ = 0.89 ± 0.44 mm/year; $CR_{Mg\text{-}1.6Li,4h}$ = 0.85 ± 0.27 mm/year) but lower than after 1 h and 2 h. Thus, over time the corrosion rate decreases, possibly due to passivation. It has to be noted that the difference of the rate over immersion time is also influenced by of the smaller influence of surface changes occurring due to the cleaning steps. Since the weight of the sample was limited to (3–4) mg, a slight attack of the film with the chromic acid is impacting the identified corrosion rate, especially for small overall weight changes due to short immersion times. This also leads to an increased corrosion rate measured by weight loss for thin films in comparison to larger bulk samples measured under the same conditions. The

attack on Mg and Mg–1.6Li was checked to be similar after cleaning and, thus, a comparison between the thin films is possible and the faster stabilisation and passivation because of Li addition can be assumed and is not influenced by this effect.

Discussion

The addition of Li highly influences the film growth, phases and, thus, microstructure and orientation of the Mg based thin films formed during sputtering. Changing from a strict columnar growth with a preferred (001) orientation to random orientations and the formation of Li_2CO_3 and oxides on the surface does not only influence the microstructure but also the resulting material properties. Thus, the properties also partially differ from results for Mg–Li bulk materials. The decrease of the tensile strength is in good agreement with literature: Mg–Li alloys show additional non-basal deformation, specifically more pronounced pyramidal and prismatic slip and twinning[46,53,54]. Because of the change in lattice structure, increasing the Li mass fraction lowers the tensile strength further. However, even though addition of Li is described to increase the maximum elongation due to the additional slip systems[53], this is not the case for the thin films in this study. The change in microstructure and orientation and void formation for Mg–3Li and the formation of brittle carbonates (and possibly oxides) for higher Li mass fractions could influence the mechanical properties and therefore hinder the improved elongation.

Degradation of hcp Mg–Li. For Mg–Li films in the hcp phase, an influence of the activity of lithium and the change in microstructure can influence the degradation. For the lowest Li fraction, a similar or lower corrosion rate was found during weight loss measurements in comparison to magnesium thin films prepared by sputtering with similar purity. This allows the assumption that effects on the corrosion rate are influenced by the Li content and no additional factors when comparing to bulk samples or samples with high purity. The lower corrosion rate for Mg–1.6Li at shorter times can be influenced by a faster formation of a protective corrosion product layer. Since the layer is not more stable or passivating than for Mg, the corrosion rates are converging for longer immersion times. However, this decrease does not occur for Mg–3Li. For α-phase Mg–Li alloys, Li et al. found a decrease in the corrosion rate from Mg–1Li to Mg–3Li for textured bulk materials, and therefore the opposite effect to the results presented in this study[17]. The average grain size of the investigated samples stays the same, but less groove-like corrosion and pitting occur. This is attributed to changes in the orientation and surface films[17]. Since an effect of the structure and microstructure was shown for bulk materials, it can be assumed that the change in microstructure and orientation from Mg–1.6Li to Mg–3Li also changes the properties of thin films in this study significantly. The change in structure for the thin films with an increase in grain size and a change in orientation differs from the change in structure for the bulk samples, the increase in Li included leads to an increase in corrosion rate instead of a decrease. This could also be influenced by the changes in void formation which is increased from Mg–1.6Li to Mg–3Li and, thus, might additionally increase the corrosion rate.

For Mg–3Li films, which have a random orientation of grains, the corrosion rate is higher than for Mg–1.6Li with a preferred orientation in the [001] direction. However, due to the change in Li content, the increase cannot be attributed to the orientation directly. To exclude additional influences, Mg–1.6Li films with a thickness of 20 µm and two different textures—(001) and (110) (Supplementary Fig. 2)—were prepared and analysed.

For both sample types, the texture is less preferred than for pure Mg, but either more (001) or (110) planes are aligned parallel to the surface, differing from a random orientation. Since the microstructure of both films is similar, the orientation can be assumed to be the main influencing factor. While the corrosion potential is less negative for (110) samples, those samples also exhibit a doubled corrosion current density (Table 3). Thus, the passivity is higher for (110) orientated samples, but the corrosion rate is confirmed to be slower for (001) planes. Oxidation and corrosion layers formed can strongly influence the corrosion rate, thus, the corrosion potential can give an insight into the activity of the surface. The properties of the passivating films such as density and thickness are influenced by orientation and the oxidation layers are often thinner but more stable for basal planes[38,55], leading to a more negative potential but still decreasing possibly the corrosion rate. Processes such as pitting are found preferably on the basal planes as well[38,56] because of a lower passivity. However, the (001) planes of the bulk material show the lowest corrosion rate according to previous studies due to the highest packing density of atoms[37,39]. Thus, the change of corrosion rate by change of orientation cannot be directly described by just taking the theoretical corrosion rates of planes into account but the orientation influences the corrosion rate of Mg–Li thin films, leading to lower corrosion rates for (001) oriented planes in this study. Therefore, it can be assumed that the increase in corrosion rate from Mg–1.6Li to Mg–3Li is influenced not only by the presence of additional Li but also the change in orientation.

Degradation of mixed phase Mg–Li. The main effect for the highest corrosion rate being measured for Mg–5.5Li can be assigned to the inclusion of additional phases and therefore micro-galvanic coupling. The increase of the Li mass fraction and second phase should, thus, lead to an even more pronounced increase

	E_{corr} (V)	i_{corr} (A/m²)	CR_{EC} (mm/year)
Mg–1.6Li (002)	− 1.79 ± 0.03	0.08 ± 0.01	0.19 ± 0.02
Mg–1.6Li (110)	− 1.68 ± 0.04	0.16 ± 0.01	0.36 ± 0.02

Table 3. Corrosion potential E_{corr}, corrosion current density i_{corr} and corrosion rate CR_{EC} resulting from Tafel plots for Mg–1.6Li films with orientations of (002) and (110).

in corrosion for Mg–9.5Li. The deviation from the expected behaviour is mainly discussed to occur due to a more protective layer formed for the cubic phase which can already cover most of the surface for mixed-phase materials with a high amount of β phase and/or small grain sizes and uniform distribution[57]. The lower activity of Mg–9.5Li and increase of the corrosion potential are in good agreement with the prevention of further fast corrosion due to a passivation layer. The Li_2CO_3 formed in air on the surface of the film (Fig. 2) for Mg–9.5Li does not necessarily lead to a protective effect and lowering of the corrosion rate since Li_2CO_3 is water soluble[28]. The formation of a stable protective layer with the increase of Li content for samples in the β phase is discussed previously as the effect of the formation of Li_2CO_3 during corrosion or MgO doped with Li[23,26–28]. However, the formation of Li_2CO_3 is not specific for films with higher Li.

Since the experiments are carried out in Hanks' balanced salt solution containing carbonates, phosphates and calcium, for all films the formation of calcium phosphates and carbonates could possibly decrease the corrosion rate. EDX studies shortly after corrosion for several days in the solution identify the corrosion products for all alloys as mainly oxygen rich, hinting at the formation of mainly oxides and hydroxides (Supplementary Fig. 3). Since the Li mass fraction is approximately 11% (m/m) in the β phase, the critical fraction of Li for doped MgO to be stable is reached (> 4.8–5.9% (m/m)) and could therefore protect the surface[28]. Further studies of the surface films and corrosion behaviour in detail are necessary to understand the corrosion process for thin films with different amounts of Li.

By comparing the different Mg–Li alloy compositions, the importance of not only the phases and microstructure but also all subsequent factors evolving by oxidation and during degradation such as protective layers are identified as the main influencing factors on the corrosion behaviour. For possible applications, the hcp phase alloys prove to be of interest due to the corrosion rate similar to pure Mg and adjustable Li release by choice of the right mass fraction of Li. Due to the better mechanical properties, Mg–1.6Li might be preferred for the use for implants if the Li release is sufficient. For treatment with a higher concentration of Li while still maintaining a relatively low degradation rate, Mg–9.5Li showed to be an interesting candidate, however, the stability over time and the influence of protective layers need to undergo further studies for reproducible use of this alloys.

Conclusion

It was shown that freestanding Mg–Li thin films can be prepared via a combination of lithography, sacrificial layer technique and magnetron sputtering. The first studies show that the structures and properties differ depending on the Li mass fraction:

1. For hexagonal Mg–Li thin film alloys (Mg–1.6Li, Mg–3Li), the growth process and subsequent microstructure is changing from an island film growth and columnar growth to film growth and a mixed grain/columnar structure with increasing Li content. Additionally, the preferred growth with one preferred orientation for Mg is less pronounced for higher Li mass fractions.
2. For mixed-phase α + β Mg–Li thin film alloys (Mg–5.5Li, Mg–9.5Li), higher Li fractions lower the corrosion rate, possibly due to protective surface film formation. Since the thin films have a total thickness in the µm range, the formation of carbonates and oxides in air can lead to an oxidation of the whole film.
3. Even though theoretically more available gliding systems should increase the ductility for increasing Li content, this is not found for the thin film samples due to the microstructure prepared by sputtering. The tensile strength is lowered in comparison to pure Mg.
4. For Mg–1.6Li thin films, the corrosion rate is similar to Mg thin film samples. However, a faster passivation leads to a faster stabilisation of the corrosion rate over immersion time. The change in microstructure and orientation leads to increasing corrosion rates with increasing Li content for hexagonal Mg–Li. When including a second phase and therefore galvanic coupling, a high increase in the corrosion rate is found, however, the formation of protective layers for higher Li mass fractions (Mg–9.5Li) improves the corrosion resistance significantly. No final statement on the composition of the protective layers is possible with the experiments in this study.

Materials and methods

Film preparation. Mg–Li alloy films were prepared on silicon substrates and as freestanding thin films following the process developed by Haffner et al.[58], consisting of a combination of UV-lithography, sacrificial layer technique with etching and sputtering. Mg–Li targets (FHR) with Li mass fractions of 2.5% (m/m), 5% (m/m), 9% (m/m) and 14% (m/m) were used. All samples were prepared in a Von Ardenne CS730S cluster machine with a base chamber pressure of $< 5 \times 10^{-7}$ mbar and 25 sccm Ar gas flow. The sputtering parameters were chosen to prepare films with low film stress at the thickness of between 10 and 20 µm and are listed in Supplementary Table 4.

A 4″ silicon (Si) wafer is coated with photoresist and structured using a mask aligner (MA6/BA6, Süss MicroTec). The structures are prepared as 15 mm × 15 mm squares for corrosion measurements and dog-bone shaped structures with a strut length of 7 mm, parallel length of 5.5 mm and a width of 0.5 mm for tensile testing. After sputtering aluminium (Al) as a hard mask, the Si wafer is etched around the Al coated structures in a deep etching step via a Bosch process (ICP-RIE SI 500, SenTech). Aluminium nitride (AlN) is deposited as a sacrificial layer before the deposition of the Mg–Li alloys. During the sputtering process, the substrate temperature was measured with temperature measuring strips. After the preparation of the final layer, Al and AlN are selectively etched in a 20%(m/m) potassium hydroxide (KOH) solution and the freestanding films are cleaned in isopropanol and distilled water. For studying the film growth of Mg–Li alloys, films on Si substrate (15 mm × 15 mm) with a thickness of 10 nm, 100 nm, 1 µm and 20 µm were deposited.

Characterisation. The chemical composition of the samples was determined using high resolution inductively coupled plasma mass spectrometry (HR-ICP-MS, Element XR, Thermo Fisher Scientific) and atomic absorption spectroscopy (AAS, Flame AAS Agilent 240 AA, Agilent Technologies) on a minimum of three freestanding thin films per composition. For ICP-MS measurements, thin films were dissolved in ultra-pure subboiled 2%(v/v) HNO_3. The resulting solutions were further diluted with ultra-pure DI water (MilliQ, QPod Element) at a dilution factor (DF) of 10 for the measurement of Li and Fe, and DF 2000 for the measurement of Mg. Indium (2.5 µg/L) was added to every sample solution for internal standardisation. All isotopes Li-7, Fe-56, and Mg-25 were measured in Medium Resolution mode (MR, 4000 R.P.). Accuracy of the results was monitored with certified reference materials "Trace elements in water" NIST SRM1643f and NIST SRM1640a. Measurement uncertainty as estimated from replicate analyses of sample solutions was 2–12%rel. for Li, and 0.1–9%rel. for Mg. For AAS, a 1 vol% HNO_3 solution and dilution factors of 3–20 for Li measurements and 200 for Mg measurements were used.

The samples were additionally analysed by X-ray diffraction (Smart Lab 9 kW, Rigaku) and SEM/EDX (Ultra 55 Plus, Zeiss and ULTIM MAX 65, Oxford Instruments). The XRD scan to identify the crystallographic structure and phases was performed with a parallel beam and monochromatic Cu kα radiation on a θ/2 θ-scan with a range of 20°–90° with a speed of 5–10°/min and a step size of 0.03°. Additional reciprocal space maps were measured by combining 2D scans for sample tilt angles of $\chi = 0°$, 15°, 30° and 45°. For studying the microstructure, cross-sections were prepared by bending the samples until fracture. SEM images are taken with an accelerating voltage of 3 kV and EDX is performed with 10 kV.

The mechanical properties were determined by uniaxial tensile testing in a BETA 5–5/6 × 10 Messphysik set-up with a strain rate of 0.4%/min. For each composition, a minimum of six dog-bone shaped samples with a thickness of approximately 20 µm were measured and the tensile strength, yield strength and elongation at fracture were compared.

Corrosion tests. Corrosion experiments were carried out in a 155 mmol Hanks` balanced salt solution (Hanks' balanced salts H1387, Sigma-Aldrich) with added sodium bicarbonate (0.35 g/l). For both corrosion measurements, the pH was kept around 7.4 (± 0.2) using a CO_2 regulation and the temperature was held at approximately 37 °C. For each measurement type and composition, a minimum of three samples were tested. For electrochemical measurements, a three-electrode set-up with an Ag/AgCl reference electrode and Pt mesh counter electrode connected to a VersaSTAT 3-300 potentiostat (AMETEKSI) was used to measure linear potentiodynamic polarisation. The sample was included as the working electrode in a sample holder with an exposed area of 0.916 cm^2. After holding the sample at the open circuit potential (E_{OCV}) for 5 min, the measurements were carried out from − 0.3 V to + 0.3 V around E_{OCV} with a scan rate of 1 mV/s. Further details regarding the setup can be found in Ref.[52]. Additionally, the weight loss during 2 h of corrosion was measured by immersion tests of the samples in the solution with the same exposed area as for electrochemical measurements. The samples were cleaned from corrosion products using chromic acid solution for 15 s. Different time lengths of treatment were tested beforehand and an appropriate time for releasing the corrosion product without attacking the underlying film material in a significant amount was chosen. The sample weight was determined before exposure and after cleaning to calculate corrosion rates. For identification of corrosion products, freestanding thin films are fully immersed in the solution at RT (24 ± 2 °C) for several days without pH control and the cross-sections are analysed via EDX as described for structural measurements.

Data availability

The datasets generated during and/or analysed during the current study are available from the corresponding author on reasonable request.

Received: 1 May 2023; Accepted: 26 July 2023
Published online: 03 August 2023

References

1. Zhao, D. *et al.* Current status on clinical applications of magnesium-based orthopaedic implants: A review from clinical translational perspective. *Biomaterials* **112**, 287–302 (2017).
2. Moravej, M. & Mantovani, D. Biodegradable metals for cardiovascular stent application: Interests and new opportunities. *Int. J. Mol. Sci.* **12**, 4250–4270 (2011).
3. Testa, L. *et al.* Sustained safety and clinical performance of a drug-eluting absorbable metal scaffold up to 24 months: Pooled outcomes of BIOSOLVE-II and BIOSOLVE-III. *EuroIntervention* **13**, 432–439 (2017).
4. Lee, J.-W. *et al.* Long-term clinical study and multiscale analysis of in vivo biodegradation mechanism of Mg alloy. *Proc. Natl. Acad. Sci. U. S. A.* **113**, 716–721 (2016).
5. Campos, C. M. *et al.* Bioresorbable drug-eluting magnesium-alloy scaffold for treatment of coronary artery disease. *Int. J. Mol. Sci.* **14**, 24492–24500 (2013).
6. Zaatreh, S. *et al.* Fast corroding, thin magnesium coating displays antibacterial effects and low cytotoxicity. *Biofouling* **33**, 294–305 (2017).
7. Vallée, A., Vallée, J.-N. & Lecarpentier, Y. Parkinson's disease: Potential actions of lithium by targeting the WNT/β-catenin pathway, oxidative stress, inflammation and glutamatergic pathway. *Cells* **10**, 230 (2021).
8. Can, A., Schulze, T. G. & Gould, T. D. Molecular actions and clinical pharmacogenetics of lithium therapy. *Pharmacol. Biochem. Behav.* **123**, 3–16 (2014).
9. Volkmann, C., Bschor, T. & Köhler, S. Lithium treatment over the lifespan in bipolar disorders. *Front. Psychiatry* **11**, 377 (2020).
10. Haussmann, R., Noppes, F., Brandt, M. D., Bauer, M. & Donix, M. Minireview: Lithium: A therapeutic option in Alzheimer's disease and its prodromal stages?. *Neurosci. Lett.* **760**, 136044 (2021).
11. Kirkland, A., Sarlo, G. & Holton, K. The role of magnesium in neurological disorders. *Nutrients* **10**, 730 (2018).
12. Gitlin, M. Lithium side effects and toxicity: Prevalence and management strategies. *Int. J. Bipolar Disord.* **4**, 27 (2016).

13. Nayeb-Hashemi, A. A., Clark, J. B. & Pelton, A. D. The Li–Mg (Lithium–Magnesium) system. *Bull. Alloy Phase Diagr.* **5**, 365–374 (1984).
14. Li, C. Q. *et al.* Natural ageing responses of duplex structured Mg–Li based alloys. *Sci. Rep.* **7**, 40078 (2017).
15. Hsu, C.-C., Wang, J.-Y. & Lee, S. Room temperature aging characteristic of MgLiAlZn alloy. *Mater. Trans.* **49**, 2728–2731 (2008).
16. Wang, B. J., Xu, D. K., Cai, X., Qiao, Y. X. & Sheng, L. Y. Effect of rolling ratios on the microstructural evolution and corrosion performance of an as-rolled Mg-8 wt.%Li alloy. *J. Magnes. Alloys* **9**, 560–568 (2021).
17. Li, C., He, Y. & Huang, H. Effect of lithium content on the mechanical and corrosion behaviors of HCP binary Mg–Li alloys. *J. Magnes. Alloys* **9**, 569–580 (2021).
18. Li, C. Q. *et al.* Composition and microstructure dependent corrosion behaviour of Mg–Li alloys. *Electrochim. Acta* **260**, 55–64 (2018).
19. Dobkowska, A., Adamczyk-Cieslak, B., Mizera, J., Kubásek, J. & Vojtěch, D. Corrosion behaviour of magnesium lithium alloys in NaCl solution. *Solid State Phenom.* **227**, 87–90 (2015).
20. Dong, L. *et al.* Corrosion behavior of a eutectic Mg–8Li alloy in NaCl solution. *Electrochem. Commun.* **129**, 107087 (2021).
21. Wang, B.-J. *et al.* Research progress on the corrosion behavior of magnesium–lithium-based alloys: A review. *Acta Metall. Sin. Engl. Lett.* **32**, 1–9 (2019).
22. Taheri, M., Danaie, M. & Kish, J. R. TEM examination of the film formed on corroding Mg prior to breakdown. *J. Electrochem. Soc.* **161**, C89 (2013).
23. Xu, W. *et al.* A high-specific-strength and corrosion-resistant magnesium alloy. *Nat. Mater.* **14**, 1229–1235 (2015).
24. Zeng, R.-C., Sun, L., Zheng, Y.-F., Cui, H.-Z. & Han, E.-H. Corrosion and characterisation of dual phase Mg–Li–Ca alloy in Hank's solution: The influence of microstructural features. *Corros. Sci.* **79**, 69–82 (2014).
25. Yan, Y., Qiu, Y., Gharbi, O., Birbilis, N. & Nakashima, P. N. H. Characterisation of Li in the surface film of a corrosion resistant Mg–Li(-Al-Y-Zr) alloy. *Appl. Surf. Sci.* **494**, 1066–1071 (2019).
26. Hou, L. *et al.* Investigating the passivity and dissolution of a corrosion resistant Mg-33at.%Li alloy in aqueous chloride using online ICP-MS. *J. Electrochem. Soc.* **163**, C324–C329 (2016).
27. Chen, X.-B., Li, C. & Xu, D. Biodegradation of Mg–14Li alloy in simulated body fluid: A proof-of-concept study. *Bioact. Mater.* **3**, 110–117 (2018).
28. Yan, Y. M. *et al.* On the in-situ aqueous stability of an Mg–Li–(Al–Y–Zr) alloy: Role of Li. *Corros. Sci.* **164**, 108342 (2020).
29. Schlüter, K. *et al.* Mechanical properties and corrosion behaviour of freestanding, precipitate-free magnesium WE43 thin films. *Int. J. Mater. Res.* **104**, 286–292 (2013).
30. Jessen, L. K., Zamponi, C. & Quandt, E. Mechanical properties of magnetron sputtered free standing Mg–Ag alloy films. *Front. Mater.* **6**, 236 (2019).
31. Jessen, L. K., Zamponi, C., Willumeit-Römer, R. & Quandt, E. Magnetron sputtered freestanding MgAg films with ultra-low corrosion rate. *Acta Biomater.* **98**, 81–87 (2019).
32. Schlüter, K., Reverey, J., Hort, N., Zamponi, C. & Quandt, E. Mechanical behaviour and corrosion performance of thin film magnesium WE alloys. *Mater. Sci. Forum* **690**, 286–289 (2011).
33. Schlüter, K. *et al.* Corrosion performance and mechanical properties of sputter-deposited MgY and MgGd alloys. *Corros. Sci.* **78**, 43–54 (2014).
34. Garcés, G., Cristina, M. C., Torralba, M. & Adeva, P. Texture of magnesium alloy films growth by physical vapour deposition (PVD). *J. Alloys Compd.* **309**, 229–238 (2000).
35. Schlüter, K., Zamponi, C., Piorra, A. & Quandt, E. Comparison of the corrosion behaviour of bulk and thin film magnesium alloys. *Corros. Sci.* **52**, 3973–3977 (2010).
36. Blawert, C. *et al.* Different underlying corrosion mechanism for Mg bulk alloys and Mg thin films: Different underlying corrosion mechanism for …. *Plasma Process. Polym.* **6**, S690–S694 (2009).
37. Song, G.-L. & Xu, Z. Effect of microstructure evolution on corrosion of different crystal surfaces of AZ31 Mg alloy in a chloride containing solution. *Corros. Sci.* **54**, 97–105 (2012).
38. Gerashi, E., Alizadeh, R. & Langdon, T. G. Effect of crystallographic texture and twinning on the corrosion behavior of Mg alloys: A review. *J. Magnes. Alloys* **10**, 313–325 (2022).
39. Liu, M., Qiu, D., Zhao, M.-C., Song, G. & Atrens, A. The effect of crystallographic orientation on the active corrosion of pure magnesium. *Scr. Mater.* **58**, 421–424 (2008).
40. Wu, G., Dai, W., Song, L. & Wang, A. Surface microstructurization of a sputtered magnesium thin film via a solution–immersion route. *Mater. Lett.* **64**, 475–478 (2010).
41. Lee, M. H., Bae, I. Y., Kim, K. J., Moon, K. M. & Oki, T. Formation mechanism of new corrosion resistance magnesium thin films by PVD method. *Surf. Coat. Technol.* **169–170**, 670–674 (2003).
42. Störmer, M., Blawert, C., Hagen, H., Heitmann, V. & Dietzel, W. Structure and corrosion of magnetron sputtered pure Mg films on silicon substrates. *Plasma Process. Polym.* **4**, S557–S561 (2007).
43. Messier, R., Giri, A. P. & Roy, R. A. Revised structure zone model for thin film physical structure. *J. Vac. Sci. Technol. Vac. Surf. Films* **2**, 500–503 (1984).
44. Pursel, S. M., Petrilli, J. D., Horn, M. W. & Shaw, B. A. *Effect of Alloy Addition and Growth Conditions on the Formation of Mg-Based Bioabsorbable Thin Films* (eds. Smith, G. B. & Lakhtakia, A.) 704113 (2008). https://doi.org/10.1117/12.796918.
45. Blawert, C. *et al.* Correlation between texture and corrosion properties of magnesium coatings produced by PVD. *Surf. Coat. Technol.* **202**, 2236–2240 (2008).
46. Agnew, S. R., Yoo, M. H. & Tomé, C. N. Application of texture simulation to understanding mechanical behavior of Mg and solid solution alloys containing Li or Y. *Acta Mater.* **49**, 4277–4289 (2001).
47. Atrens, A. *et al.* Review of Mg alloy corrosion rates. *J. Magnes. Alloys* **8**, 989–998 (2020).
48. Johnston, S. *et al.* The influence of two common sterilization techniques on the corrosion of Mg and its alloys for biomedical applications: Influence of two common sterilization techniques. *J. Biomed. Mater. Res. B Appl. Biomater.* **106**, 1907–1917 (2018).
49. Johnston, S. *et al.* Investigating Mg biocorrosion in vitro: Lessons learned and recommendations. *JOM* **71**, 1406–1413 (2019).
50. Hofstetter, J. *et al.* Assessing the degradation performance of ultrahigh-purity magnesium in vitro and in vivo. *Corros. Sci.* **91**, 29–36 (2015).
51. Geary, A. L. Electrochemical polarization. *J. Electrochem. Soc.* (1957).
52. Jurgeleit, T., Quandt, E. & Zamponi, C. Magnetron sputtering a new fabrication method of iron based biodegradable implant materials. *Adv. Mater. Sci. Eng.* **2015**, 1–9 (2015).
53. Haferkamp, H. *et al.* Entwicklung und Eigenschaften von Magnesium-Lithium-Legierungen. 6 (2001).
54. Zou, Y. *et al.* Deformation mode transition of Mg 3Li alloy: An in situ neutron diffraction study. *J. Alloys Compd.* **685**, 331–336 (2016).
55. Bland, L. G., Gusieva, K. & Scully, J. R. Effect of crystallographic orientation on the corrosion of magnesium: Comparison of film forming and bare crystal facets using electrochemical impedance and Raman spectroscopy. *Electrochim. Acta* **227**, 136–151 (2017).
56. McCall, C. R., Hill, M. A. & Lillard, R. S. Crystallographic pitting in magnesium single crystals. *Corros. Eng. Sci. Technol.* **40**, 337–343 (2005).
57. Wang, *et al.* Developing improved mechanical property and corrosion resistance of Mg–9Li alloy via solid-solution treatment. *Metals* **9**, 920 (2019).

58. Haffner, D., Zamponi, C., de Miranda, R. L. & Quandt, E. Micropatterned freestanding magnetron sputtered Mg-alloy scaffolds. *BioNanoMaterials* **16**, (2015).

Acknowledgements
The authors thank Dr. Heike Helmholz from the Institute for Metallic Biomaterials of the Helmholtz Centre hereon for her support with the AAS measurements. This work was supported by the DFG in the framework of the research training group 2154—Materials for Brain (project 270394294).

Author contributions
L.H. and L.K.J. conception and design of the study, L.H. writing-original draft, analysis of results; L.H., F.W., K.B. and U.W. performing experiments, E.Q, R.W.-R. conception of general project, E.Q., R.W.-R. and D.G.-S. supervision of the work. All authors reviewed the manuscript.

Funding
Open Access funding enabled and organized by Projekt DEAL.

Competing interests
The authors declare no competing interests.

Additional information
Supplementary Information The online version contains supplementary material available at https://doi.org/10.1038/s41598-023-39493-9.

Correspondence and requests for materials should be addressed to E.Q.

Reprints and permissions information is available at www.nature.com/reprints.

Publisher's note Springer Nature remains neutral with regard to jurisdictional claims in published maps and institutional affiliations.

3.2 Influence of sputtering parameters on the corrosion rate of Mg-3Li

As discussed in the publication in chapter 3.1, the corrosion rate can not only be influenced by the Li content itself but also by the structure, e.g., the orientation. To investigate this influence further, the impact of a structure change by adjustment of sputtering parameters and, thus, the direct tuning of the corrosion rate during the sputtering process, is discussed in the following study.

Power [W]	Pressure [10^{-3} mbar]	Sputtering rate [nm/s]
50	2.3	1.78
100	1.5 2.3 4 6	3.19
150	2.3	4.70

Table 3.1: Set of sputtering parameters for magnetron sputtering of Mg-3Li to analyse the influence of power and pressure change on the structure and corrosion rate of the thin films.

The properties of thin films prepared by magnetron sputtering can be influenced by changing the parameters such as pressure, power or gas flow. In this study, a variation of power (50-150 W) and pressure (1.5-6·10^{-3} mbar) for Mg-3Li is exemplarily investigated to identify possible influences on the structure of the film and the resulting corrosion rate (sputtering parameters table 3.1). Figure 3.1 shows the corrosion rates for all tested parameter combinations.

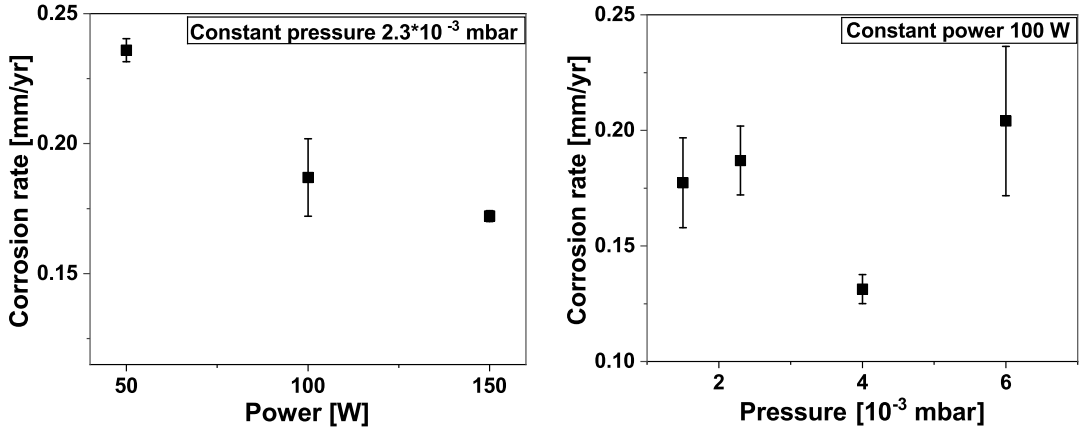

(a) (b)

Figure 3.1: Comparison of corrosion rates for Mg-3Li thin films on substrate sputtered with different sputtering parameters (for power change: a) constant pressure of 2.3·10^{-3} mbar, for pressure change: b) constant power of 100 W).

Since the film stress varies, all corrosion studies were performed on substrate. Different corrosion potentials between -1.70 V and -1.79 V are measured for all parameter sets, but

no direct dependence on power or pressure can be assigned. The lowest corrosion rate is determined for samples prepared with a power of 100 W and pressure of $4{\cdot}10^{-3}$ mbar. Especially for the highest pressure of $6{\cdot}10^{-3}$ mbar, the potentiodynamic polarisation measurement is more unstable with high fluctuations, including steps from possible pitting and depassivation, therefore leading to higher errors. Since not all parameter combinations are tested, this study does not aim to determine the lowest or highest possible corrosion rate but instead to identify possible correlations between parameters, microstructure and corrosion rate, therefore showing tuning possibilities.
Film stress analysis by producing freestanding thin films and comparing the rolling ratios shows that changing the parameters leads to significant film stress (figure 3.2).

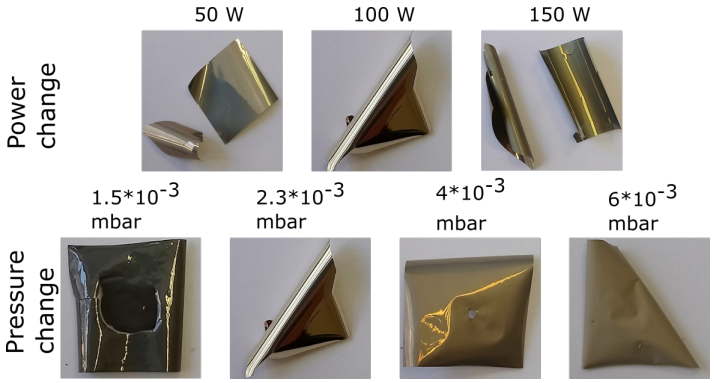

Figure 3.2: Comparison of freestanding Mg-3Li sputtered at different pressure and power (for power change: constant pressure of $2.3{\cdot}10^{-3}$ mbar, for pressure change: constant power of 100 W). The film stress can be identified by the rolling of the films.

For a pressure of $2.3{\cdot}10^{-3}$ mbar, the lowest film stress is exhibited for 50 W samples; higher power leads to compressive stress. At 150 W, both compressive and tensile stress samples can be found, depending on the position on the wafer during sputtering. The surface of all samples, but especially for 100 W, are shiny and, therefore, smooth. At 100 W, a change of pressure leads to flat and stable films for a pressure of $4{\cdot}10^{-3}$ mbar with compressive stress for the other films, thus not allowing a direct trend. For all pressures sputtered at 100 W, the surface is smooth. However, a colour change for the lowest pressure indicates a change in the sample surface (figure 3.2).
Factors such as grain size, roughness, and grain boundaries could also influence the corrosion rate. As discussed by Qu et al., smaller grains can decrease the biodegradation rate of pure Mg [124]. The improved corrosion resistance could be influenced by an improved oxide layer or grain boundaries acting as corrosion barriers [124, 203]. However, if the surroundings do not allow for sufficient passivation due to high corrosion rates [122], the corrosion rate can also be increased. Grain boundaries offer possible attack points for corrosion if the structure is not dense due to increased surface area. Here, the grain size decreases with increasing sputtering power, and the structure is denser, with smaller grain structures apparent on the surface. This reduces the area of easy attack. Due to the additional energy at a higher power, more diffusion of atoms is possible, hindering a strong shadowing. At much higher energies, this can additionally lead to a shift from the T zone to zone 2 with stronger columnar growth [204]. However, in the samples discussed here, microstructural analysis of cross-sections of all sample types does not show a significant change in the microstructural type (figure 3.3).
Increasing the pressure can lead to lower energy of the incident sputtered atoms and, thus, more lattice defects [29]. However, other studies describe that a pressure change does not

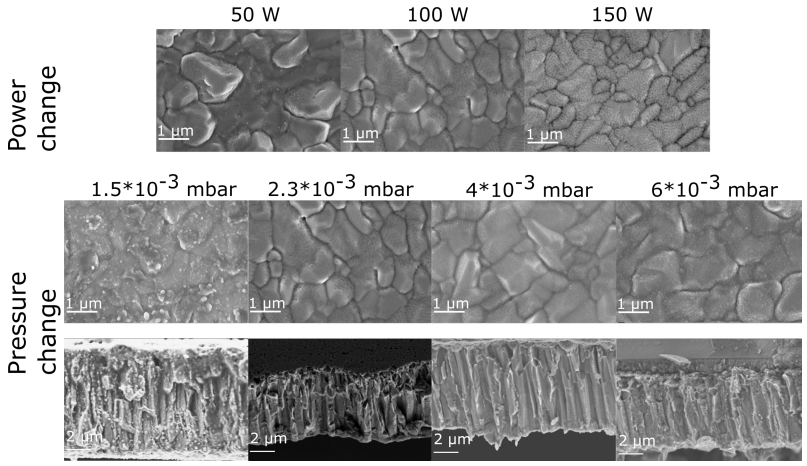

Figure 3.3: Microstructure of Mg-3Li thin films sputtered at different pressure and power (for power change: constant pressure of $2.3{\cdot}10^{-3}$ mbar, for pressure change: constant power of 100 W).

influence the corrosion rate [102] or can lower the corrosion rate by leading to finer granular structures [205]. For samples prepared at the lowest pressure of $1.5{\cdot}10^{-3}$ mbar, the SEM images confirm the change in the surface properties, which was already apparent due to the colour change. The sputtering at such pressures is less stable, and smaller particles or droplets can be found on the surface and in the film. However, since no significant change of the corrosion rate to the pressure of $2.3{\cdot}10^{-3}$ mbar is measured, this cannot be the main influence for a corrosion rate change. For samples sputtered at the pressure of $4{\cdot}10^{-3}$ mbar, thin columnar structures are formed. Even though the surface is not flat, no significant gaps and no rough sub-structure on the grains are formed.
Since the Mg-3Li samples for a pressure of $4{\cdot}10^{-3}$ mbar and a power of 100 W showed the lowest corrosion rate and low film stress, freestanding thin films were prepared for corrosion measurements, leading to corrosion rates of 0.14±0.02 mm/yr in comparison to 0.27±0.07 mm/yr for the standard sputtering parameters at 50 W described in the chapter 3.1. For both samples, a similar Li fraction (3.5±0.5 wt% vs 3.9±0.1 wt%, measured by AAS) is found. Therefore, this cannot be a main influence on the change in corrosion rate. The main difference shown in cross-sectional images of the microstructure is analysed to be a denser structure and smaller columns, indicated by fewer voids at grain boundaries, and a flatter surface structure with less pronounced grain boundaries (figure 3.4 a). The comparison of exact XRD peak heights for freestanding thin films is difficult since they cannot be fixed completely flat. However, no significant change in orientation can be observed and stronger signals and, thus, more low-indexed planes parallel to the surface can be found for the 100 W sample (figure 3.4 b). Thus, by changing the sputtering parameters, the same corrosion rate as for Mg-1.6Li in freestanding thin films can be achieved for Mg-3Li.

As a result, no direct trend, such as a decrease in corrosion rate with increasing power or decreasing pressure, can be identified. Still, the possibility of influencing the corrosion rate is confirmed. Multiple factors, including a preferred orientation, grain size, void formation, surface roughness and low film stress, affect the corrosion rate. Thus, the parameters have to be chosen accordingly for each alloy type. To allow a controlled tuning of the properties, the influence of the parameters on the plasma and, therefore, film growth needs to be further analysed.

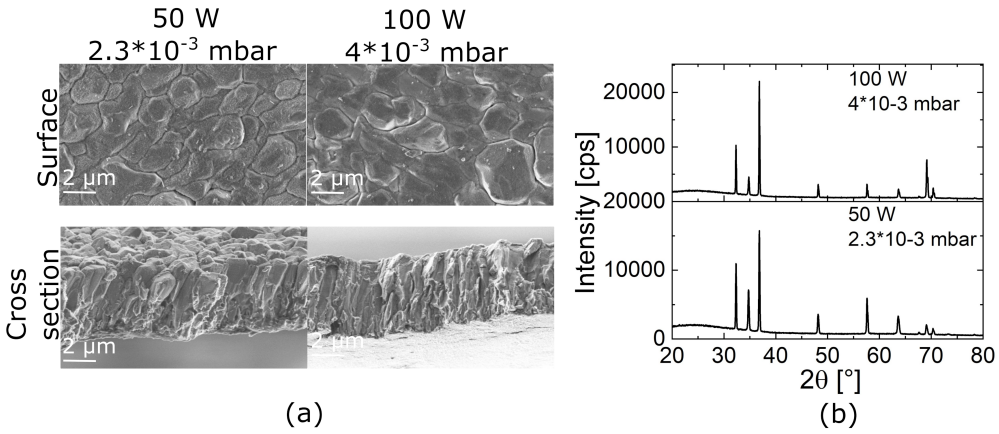

Figure 3.4: Comparison of SEM and XRD analysis of Mg-3Li sputtered with two sets of sputtering parameters (50 W, $2.3{\cdot}10^{-3}$ mbar and 100 W, $4{\cdot}10^{-3}$ mbar) producing stress-free films.

3.3 Analysis of long-term corrosion in different solutions

The corrosion experiments of the studies are carried out mainly in HBSS over shorter periods of time due to the measurement set-up (potentiodynamic polarisation or weight loss in sample holder). To identify further influencing factors and see the corrosion long term, freestanding samples of Mg, Mg-1.6Li and Mg-3Li are placed in HBSS without heating (18-23 °C) or pH control (pH range of 7-8.5). The pictures of Mg-1.6Li are shown in figure 3.5. After a colour change due to the formation of corrosion product on the surface, holes occur due to inhomogeneous corrosion.

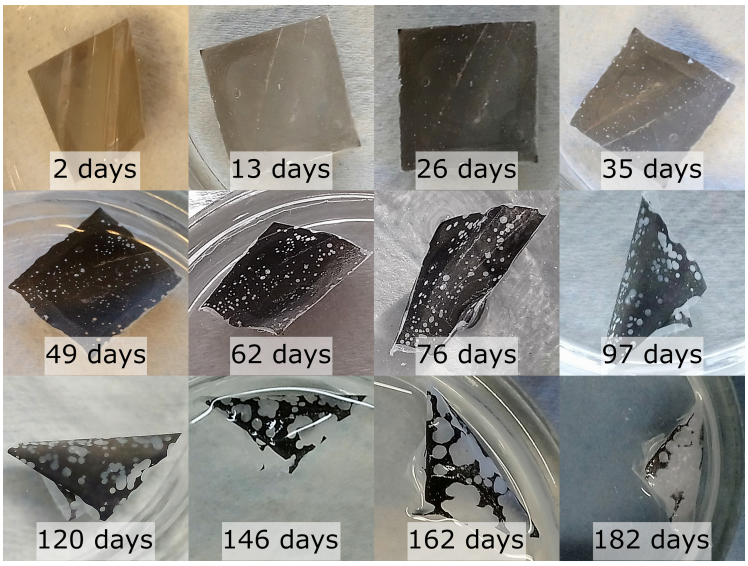

Figure 3.5: Exemplary photos of corrosion of Mg-1.6Li over 182 days in HBSS.

As can be seen in figure 3.6, for all three sample types, the corrosion does not take place homogeneously over the whole surface but holes are formed due to defects and pitting. Due to the rolling of mainly Mg-3Li and Mg, the corrosion rate cannot be directly identified but after around 55-60 days, Mg-1.6Li has the largest remaining area of thin film (dark

film area), indicating a lower corrosion rate as already described in the paper in 3.1. For

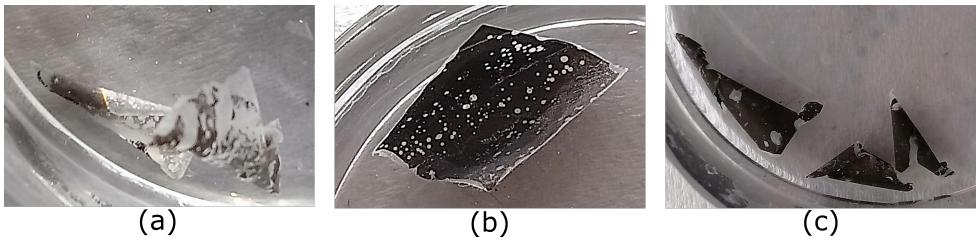

Figure 3.6: Corroded samples of a) Mg (55 days), b) Mg-1.6Li (62 days), c) Mg-3Li (57 days) in HBSS.

all samples, the formation of a white corrosion product partially retaining the shape of the thin film is found. To further identify change of the film during the corrosion, XRD and SEM analysis on the corroded samples were performed. In figure 3.7, the formation of a corrosion product layer can be easily identified by a change in microstructure. This surface layer, however, is not dense and is cracked throughout the whole film. In the area of the white corrosion product, the microstructure is completely changed, only leaving a porous material.

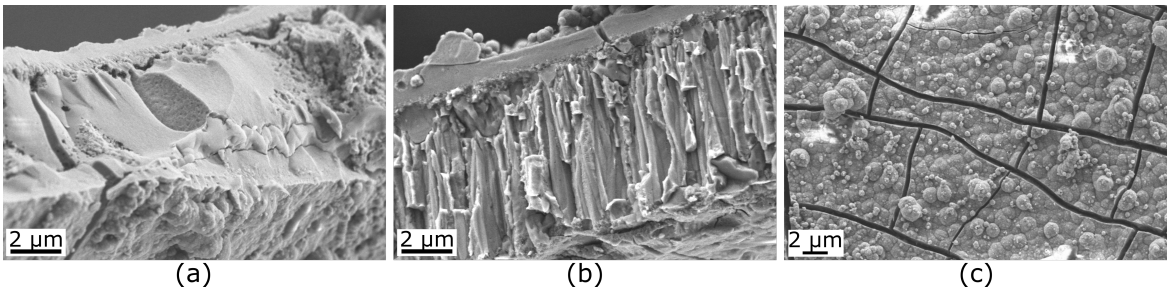

Figure 3.7: SEM of Mg-1.6Li samples after 63 days in HBSS. a) Cross section of white, corroded area, b) cross section of dark area, c) surface.

To identify the change of the film, XRD analysis was carried out on both the dark (possibly remaining metal alloy) and white (pure corrosion product) area of Mg, Mg-1.6Li and Mg-3Li samples. In figure 3.8, both are directly compared to the spectra of uncorroded thin films. In the grey regions, the Mg or MgLi can still be identified for all samples but is much lower or not present for the white regions due to the corrosion. Instead, MgO and carbonate containing compounds ($MgCO_3$ or $Mg_xCa(CO_3)_{x+1}$) can be found on both MgLi alloys with additional influences of salts such as NaCl since the samples could not be completely cleaned due to instability after corrosion. It can be assumed that the white area is not only a salt accumulation of NaCl singe it mimics the shape of the metal film before (see figure 3.6), thus, corrosion products of the thin films are included. The signal in general is lower due to the reduced amount of material. In addition, XRD only detects crystalline material, thus, any amorphous components cannot be determined. A possible inclusion of Ca into the corrosion product hints to the importance of the solution on the corrosion process as discussed in section 2.3.2. HBSS is chosen since it includes the many elements which are present in the human body such as Na, Ca, Mg, K, Cl, S or P and glucose (H1387, Sigma-Aldrich with added sodium bicarbonate). Other studies for Mg corrosion are carried out in simple NaCl salt solutions (e.g. [156, 165]) or other simulating body fluids (e.g. [163, 187]). To see the effect of the salts on the corrosion of MgLi, samples

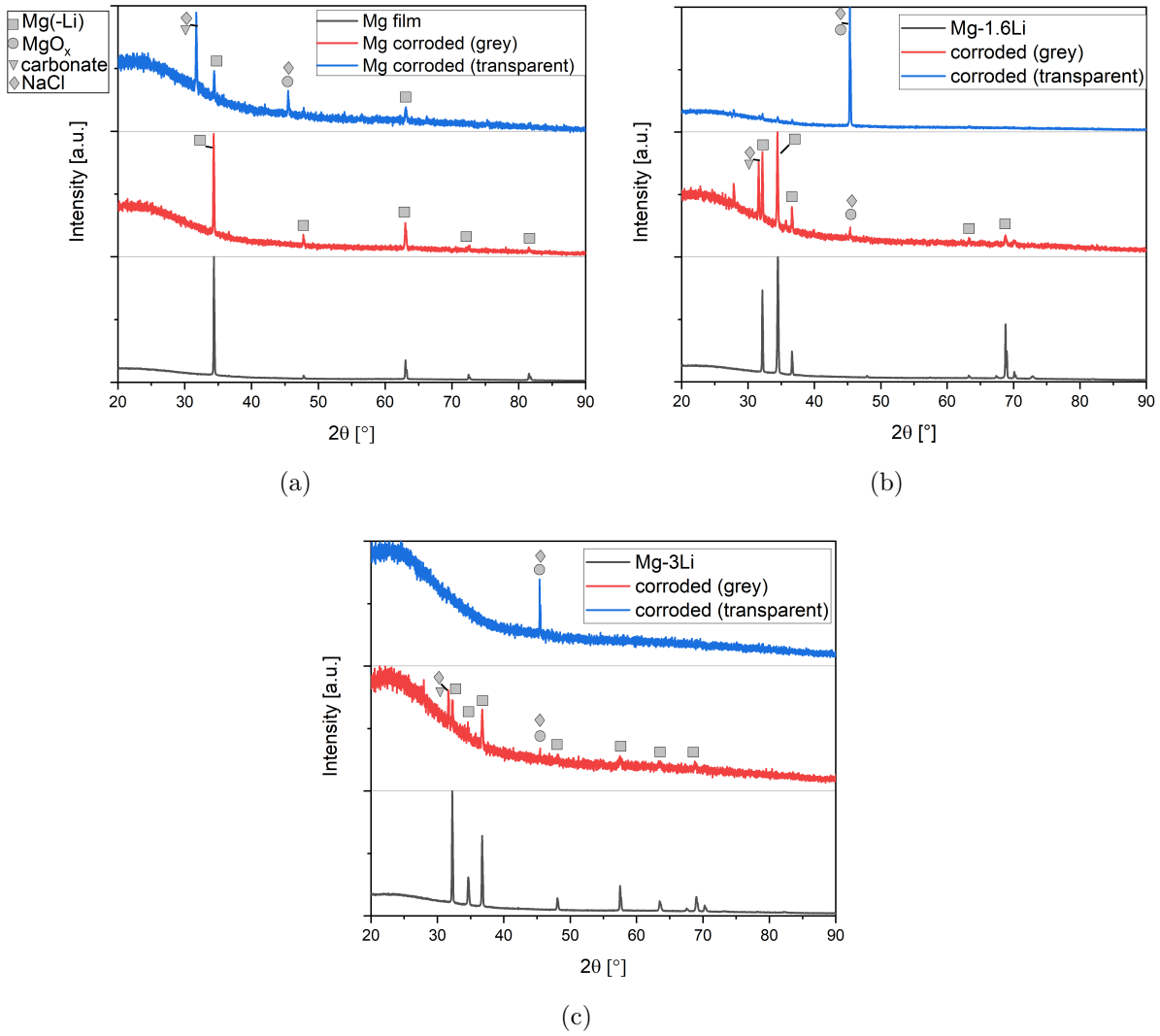

Figure 3.8: XRD of a) Mg after 56 days, b) Mg-1.6Li samples after 66 days, c) Mg-3Li after 74 days corrosion in HBSS on white and grey sample area. Additionally, XRD diffractograms of the samples before corrosion are shown.

of Mg-1.6Li were placed in HBSS, DMEM (Dulbecco's modified Eagle's medium, DMEM, 31966047, Thermo Fisher, with 10 % fetal bovine serum, S0615, Merck), aCSF (artificial cerebrospinal fluid) and distilled water as a comparison without temperature and pH control.

In figure 3.9, images of the samples after short immersion and after longer immersion are shown. For samples in both distilled water and DMEM, the sample is nearly completely corroded before 10 days in solution while samples in both aCSF and HBSS are more stable with large areas intact or more homogeneously corroded after over 50 days. An estimation therefore leads to a corrosion rate <0.6 mm/yr in DMEM and water, <0.1 mm/yr in aCSF and <0.05 mm/yr in HBSS. Since the film is, however, not corroding homogeneously, this only gives an estimation of the influence of corrosion and no direct corrosion rates.

The composition of aCSF is similar to HBSS, containing mainly salts and glucose including carbonates, phosphates and Na, Ca, Mg, Cl. The DMEM used in this studies overall has a higher concentration of salts than in HBSS and additionally includes amino acids and vitamins. The concentration of Ca and carbonates and phosphate containing components

is higher, thus, an easier formation of such components on the formation of a passivating layer cannot be the deciding factor. The organic components can in theory also decrease the corrosion rate [135]. One possible explanation is a change in pH. DMEM is found to buffer a change in pH better than HBSS [135], thus, due to the lack of pH control, an increase in pH can be more pronounced in HBSS, leading to lower corrosion rates.

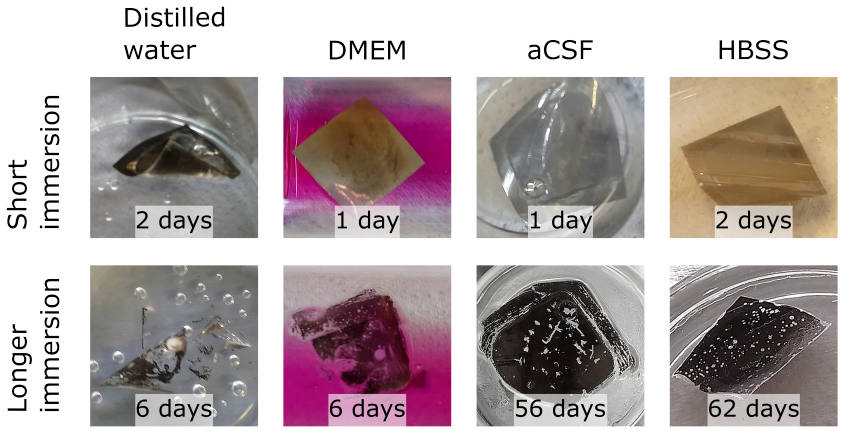

Figure 3.9: Mg-1.6Li samples in different solutions after short (1-2 days) and longer corrosion (for fast corroding samples 6 days, for slow corroding samples around 60 days).

3.4 Publication: Investigation of in-situ ion release and surface film formation of hcp Mg-Li thin films

In addition to the influences of the microstructure on the corrosion rate of the hcp α-MgLi alloys (Mg-1.6Li and Mg-3Li), which are discussed in 3.1, the ion release of the samples can give further insight into changes of the corrosion with a change in Li content. Therefore, both long-term (3 days) and short-term studies (in-situ study during the first 30 min-1 h of immersion) were carried out to analyse the release of both Mg and Li over time.
For comparison, thin films with 5.5 wt% of Li were added with a composition very close to the boundary between hcp and mixed phase.
The difference in corrosion process previously suspected by the change in corrosion rate to an increased corrosion rate with Li fraction and microgalvanic coupling for Mg-5.5Li were confirmed, and a process of preferred ion release over time was proposed.
Further, a Li-rich layer on the surface of the α-phase samples stored in air was found, which is released directly after contact in solution and, thus, increases the Li concentration during the start of the treatment if not pre-treated. Therefore, the formation of Li_2CO_3 on the surface of α-MgLi confirms that the corrosion rate reduction for β-MgLi might not only be influenced by Li_2CO_3 as discussed in section 2.3.5.

Own contributions to the following article
(concept - 75 %, planning - 80 %, experiments - 75 %, analysis - 90 %, writing - 90 %):

- Sample preparation
- Set-up and corrosion for preparation of long-term study
- Online ICP-MS measurements
- Interpretation and discussion of the results
- Writing of the manuscript

Corrosion Science 238 (2024) 112361

Contents lists available at ScienceDirect

Corrosion Science

journal homepage: www.elsevier.com/locate/corsci

Investigation of in-situ ion release and surface film formation of hcp Mg-Li thin films

Lisa Hanke [a], Lukas Kalchgruber [b], Ulrike Westernströer [c], Dieter Garbe-Schönberg [c], Eckhard Quandt [a], Markus Valtiner [b,*]

[a] Inorganic Functional Materials, Institute for Materials Science, Kiel University, Kiel, Germany
[b] Applied Interface Physics, Institute of Applied Physics, Vienna University of Technology, Vienna, Austria
[c] Marine Climate Research, Institute of Geosciences, Kiel University, Kiel, Germany

ARTICLE INFO

Keywords:
A Magnesium
A Sputtered films
B ICP- MS
B XPS
C Surface films

ABSTRACT

In this work, the dissolution process of magnetron sputtered Mg-Li thin films was investigated by in-situ flow cell/ICP-MS measurements and ex-situ ICP-MS measurements after longer immersion and additional XPS measurements. High Li concentrations are released due to a Li rich carbonate layer formed in air. The depletion of Li leads to preferred Mg release before preferred Li release occurs due to the higher activity of Li and incorporation of Mg in corrosion products. This data provides a baseline for developing release profiles for medical application, more generally, it unravels details of the corrosion mechanism of lightweight MgLi alloys.

1. Introduction

Biodegradable materials such as magnesium (Mg) are of interest for several medical applications to reduce permanent implants' side effects, improve bone healing or release bioactive components [1–4]. A key point of interest is the understanding and control of the degradation rate of such implant materials to verify the lifetime of the implants, avoid adverse effects from fast corroding materials and allow for the adjustment of the material properties to facilitate a better treatment [5–7]. Understanding the degradation process becomes even more crucial if the degradation products, e.g., corrosion products and pH change [4] or ion release [8], are used as therapeutically active species. A material of interest for ion release studies is magnesium-lithium. While the release of lithium (Li) from different materials is already studied [9–12], it was recently proposed to use Mg-Li thin films as a reservoir implant releasing Li for the local treatment for neurological applications [8,13] such as the treatment of bipolar disorder, Alzheimer's or Parkinson's disease [14–17]. The therapy with Li is associated with several side effects and has a small therapeutic window [15,18]. Thus, the control of the concentration is of high importance. Mg can be used as the base material for implants not only because it is already widely studied as a biodegradable and biocompatible material and used in clinical trials and medical applications [2,19] but also because it shows possible positive therapeutic effects [19,20]. The treatment with Mg-based materials is already established for particles loaded with additional drugs or using the degradation products, such as hydrogen. Here, both the benefit of a biodegradable carrier and the effect of Mg itself are taken advantage of [21–24].

Mg-Li alloys can be differentiated in α-Mg-Li, α+β-Mg-Li and β-Mg-Li with α as the hexagonal closed packed (hcp) Mg-rich phase and β as the body centred cubic (bcc) Li-rich phase. Generally, the highest corrosion rate is found in the mixed phase α+β due to the microgalvanic coupling of those phases, while single phases show a lower corrosion rate [25,26]. For hcp α-phase Mg-Li with low Li content, the corrosion process is discussed to be similar to pure Mg with the formation of oxide and hydroxide layers [27,28] and filiform corrosion occurring [26,29]. Li carbonate containing protective layers were also found for Mg-5Li-1Al samples in the hcp phase [30]. For neurological applications, implants need to be produced in small sizes. The properties of such thin films are highly affected by surface effects and can differ from bulk material [31,32]. As previously shown [8], similar to bulk material, Mg-Li thin films with low Li fraction show a corrosion rate similar to Mg thin films in a medium chosen to simulate physiological conditions, while the corrosion rate increases for higher Li fractions.

The ion release of Mg-Li-Zn alloys [33] and Mg-Li-(Al)-(RE) [34] was tested to identify the corrosion rate and influence on cells after longer immersion time for applications as stent material. Zhou et al. found an increase in both Li and Mg release for Mg-8.5 wt% Li in comparison to

* Corresponding author.
E-mail address: markus.valtiner@tuwien.ac.at (M. Valtiner).

https://doi.org/10.1016/j.corsci.2024.112361
Received 13 May 2024; Received in revised form 29 July 2024; Accepted 8 August 2024
Available online 13 August 2024

Mg-3.5 wt% Li [34]. The released Mg and Li concentration from Mg-Li thin films with 1.6 wt% and 9.5 wt% Li in Dulbecco's modified Eagle's medium also showed an increased release of Li and Mg with increasing Li content due to a higher corrosion rate [13]. The in-situ measurement of ion release can give further insights not only into the element concentration available after release but also into the corrosion process itself. Based on the concept of AESEC (atomic emission spectroelectrochemistry) [35–37], combinations of flow cells and inductively coupled plasma – optical emission spectrometry (ICP-OES) or inductively coupled plasma - mass spectrometry (ICP-MS) have been used to analyse Mg and Mg-Li corrosion. In addition to identifying the change in ion release by changing pH, contaminations or determining the stoichiometry of participating ions [38–41], the formation of surface films can also be studied by these techniques. Studies were carried out on β-Mg-Li based alloys to determine the passivation layer formed by analysing the released ion concentration of each element dependent on the applied voltage or after scratching to increase the corrosion rate of those alloys and determines the layer formation before and during immersion [42–44]. By identifying the change in ratio of released Mg and Li, the formation of Li_2CO_3 or MgO doped with Li was proposed.

While the formation of surface films and the ion release have been analysed by surface measurements and in-situ studies for films with higher Li content, for α-Mg-Li, Mg-like corrosion has mainly been assumed, and the influence of Li during the process is often overlooked. Thus, this study aims to gain insight into the process of surface film formation before and during the corrosion of α-Mg-Li in simulated physiological medium, especially for magnetron-sputtered thin films. Since the films with lower Li content proved to be biocompatible and released a concentration in the therapeutic window during the previous study by Bhat et al. [13], a detailed understanding by in-situ studies of films with low Li fraction is also important for the application.

The start of immersion was analysed by online ICP-MS. The addition of an electrochemical set-up in the flow cell allowed the further studying if non-equilibrium conditions are applied to enhance the corrosion rate and identify passivation. The surface composition is determined for further analysis of the surface on as prepared samples and after corrosion. Additionally, 3-day immersion studies were carried out in a medium chosen to simulate physiological conditions, and the released ion concentration was identified after solution extraction to provide information regarding the ion concentration over longer immersion times. Thus, by combining both techniques, the degradation process over different time scales can be described and the profile of ion release for possible treatments can be determined.

2. Material and methods

2.1. Film preparation

Thin films of Mg-Li alloys were fabricated in a Von Ardenne CS730S cluster machine from targets (FHR Anlagenbau GmbH) with Li content of 2.5 wt%, 5 wt% and 9 wt% by magnetron sputtering. A base chamber pressure of $<5*10^{-7}$ mbar, a gas flow of 25 sccm Ar and pressures ($2.3–3.3*10^{-3}$ mbar) adjusted to fabricate samples with low film stress were chosen. As the substrate, 1.5 cm×1.5 cm and 1 cm×1 cm Si chips with additional Al/AlN layers were used. The Al/AlN was added to ensure the same film growth as for the preparation of freestanding thin films for which the AlN is necessary as a sacrificial layer. The Li weight fraction in the prepared films with a thickness of 20 µm (±10 %) resulted in 1.6 wt% (1.60±0.06 wt%), 3 wt% (3.07±0.12 wt%) and 5.5 wt% (5.15±0.69 wt%) of Li [8]. Thus, two sample types (Mg-1.6Li, Mg-3Li) with a hcp α-MgLi phase and one sample type (Mg-5.5Li) with mixed α-MgLi, β-MgLi and Li_2CO_3 were prepared [8].

To study the degradation of the thin films over longer immersion times, freestanding thin films with the same compositions were prepared by UV-lithography, sacrificial layers of AlN and the magnetron sputtering of the Mg-Li alloys. For further information regarding the preparation method see Haffner et al. [45].

2.2. In-situ study

A set-up combining a flow cell and an ICP-MS (inductively coupled plasma - mass spectrometer, Agilent 7900 ICP-MS, Agilent Technologies) was used to measure the ion release from Mg-Li thin films in-situ. The set-up and flow cell were previously described in detail [46]. A flow cell with a three-electrode set-up with an Ag/AgCl reference electrode (RE) and a Pt counter electrode was connected to a Biologic VSP-300 potentiostat. The sample size in contact with solution was determined by the O-ring size of the flow cell with a diameter of 3 mm. 15 mmol HBSS (Hanks' balanced salts H1387, Sigma-Aldrich with added sodium bicarbonate (0.35 g/L), solution diluted with distilled water from 155 mmol) was used and pumped through the flow cell by pressurised nitrogen. A Ga standard was added after the flow cell as a control. The composition of the solution was measured using an ICP-MS. The Mg and Li concentrations were calibrated with a multi-element calibration standard 2a (Agilent) and ICP multi-element standard solution XVI. The overall flow speed of the solution was determined by measuring the overall volume of the solution collected in a flask after the ICP-MS at the end of each measurement. Changes in the flow speed during the measurement could be corrected using signals of other elements included in the solution, but not in the sample, such as Ca.

By considering the exposed area (determined by the O-ring size), the dissolution rate j_m is then defined as the dissolved mass of the specific element per time and area. The dissolution current density was calculated by $i = j_m \cdot z \cdot F/M$ with the molar mass M, Faraday constant F and z the valence number of the ions.

The flow cell was connected in parallel to a direct tube of the solution to the ICP-MS and the measurements were started with the measurement of pure solution before switching to the flow cell to analyse the ion release beginning at the start of the degradation. The first degradation is shown at the time t=0 s. Since the signal is often noisy, additional to the raw data, a smoothed signal is shown additionally in plots to identify the general trend.

The first tests were carried out without applying an additional potential (at open circuit potential, E_{OCV}) for 50–60 min. The E_{OCV} was monitored using the potentiostat. To analyse the degradation further, additional samples were held at fixed voltages (Fig. 1a) of +0.2 V vs. E_{OCV}, −0.9 V vs. Ag/AgCl and −0.5 V vs. E_{OCV} for 15 min (constant voltage, CV) after 10 min of immersion (OCV). Additionally, linear sweeps of voltage (LSV) were applied from E_{OCV} to −0.5 V vs. Ag/AgCl

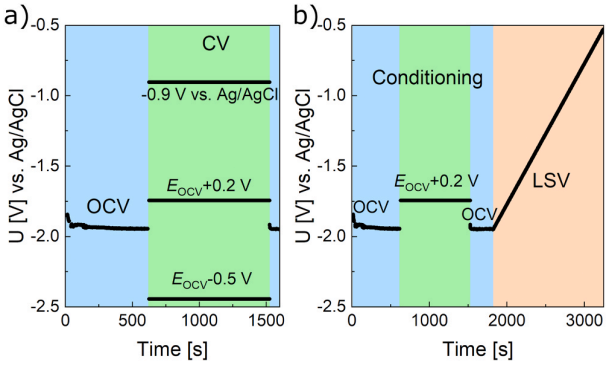

Fig. 1. Exemplary voltage profile applied and measured at flow cell during in-situ ICP-MS measurements: a) For constant voltage (CV) measurements, one of three different potentials is applied after 10 min of open circuit potential measurements (OCV). b) For linear scan voltammetry (LSV) measurements, after OCV, CV at E_{OCV}+0.2 V for 15 min and a further 5 min of OCV for conditioning, the voltage is continuously increased from E_{OCV} up to −0.5 V vs. Ag/AgCl reference electrode.

with a sweep speed of 1 mV/s after 10 min E_{OCV}, 15 min +0.2 V vs. E_{OCV} and 5 min E_{OCV} (see Fig. 1b) for stabilisation.

2.3. 3-day immersion

Freestanding thin films of three Mg-Li alloys were placed in beakers with 100 mL of 155 mmol Hanks' balanced salt solution (HBSS, Hanks' balanced salts H1387, Sigma-Aldrich with added sodium bicarbonate (0.35 g/L)) at a pH of 7.4±0.2 (continuous measurement using a pH meter and adjusted by CO_2 influx) and a temperature of 37±1 °C. After 1 h, 4 h, 24 h and 72 h, 15 mL of solution were extracted, and 15 mL of HBSS from the same starting solution were added. The maximum immersion time was chosen due to the fast degradation for samples with low thickness with both sides exposed to the solution and formation of holes for longer immersion times. The extracted solution was then diluted with ultra-pure DI water (MilliQ, QPod Element) at a dilution factor (DF) of 10 for the measurement of Li and Fe, and DF 2000 for the measurement of Mg for high-resolution inductively coupled plasma - mass spectrometry (HR-ICP-MS, Element XR, Thermo Fisher Scientific) as described in [8]. The Mg and Li concentrations of the blank solution and after corrosion at each time point were determined. The solution partially evaporated over the measurement time. Thus, a beaker with a blank solution was heated simultaneously in a similar set-up to assess the evaporation over the measurement duration. The data from the measurement was used to calculate the released masses (measured concentration and calculations described in supplementary).

2.4. Surface composition characterisation

Four samples per alloy type were used to analyse the sample's surface composition before corrosion, after contact with the solution and after corrosion. One sample was measured as prepared, one was dipped into HBSS (155 mmol) shortly before measurement, and two samples were corroded for 1 h in HBSS. For the two corroded samples, one is stored in air and one in ethanol between corrosion and measurement. All samples were analysed using X-ray photoelectron spectroscopy (XPS) measurements. An Axis Supra spectrometer from Kratos Analytical at the Ceitec Nano Research Infrastructure was utilised. An aluminium anode that produced Al Kα X-rays was used as a radiation source. Since the samples have low conductivity on the surface due to oxide formation and, thus, can show a peak shift due to charging effects, they were measured with charge neutralisation. The samples were mounted on copper tape. The data was evaluated using the software CasaXPS (Version 2.3.23PR1.0). After subtracting a Shirley-type background, the binding energy scale was calibrated by shifting the C 1 s main peak to 284.8 eV.

3. Results

3.1. In-situ ion release at the start of immersion

The ion release of two hcp Mg-Li thin films with Li fractions of 1.6 wt % and 3 wt% were measured in-situ in 15 mmol HBSS by placing samples in a flow cell directly connected to an ICP-MS. In addition to the two hcp Mg-Li alloys, Mg-5.5Li films with very low content of the additional β-phase [9] were analysed for comparison to a mixed-phase material with a higher corrosion rate.

For the first tests, no voltage was applied. Fig. 2 shows the release of Mg and Li directly after contact with the solution exemplarily for one sample per alloy. For all samples, a high release of Li directly after contact is detected, while no such peak can be found in the Mg release. The peak shows a very sharp increase and decrease. This behaviour can be explained by a Li-rich, easily soluble layer on the surface. The distribution of ions in the solution during transport to the ICP-MS might influence the peak width and, therefore, it might be broader than the actual released profile [36]. The height of the peak in the dissolution current density of Li i_{max} increases with increasing Li fraction in the film (Fig. 2b). This height can be influenced by the Li fraction at the surface due to, e.g., a thicker or more complete layer of a Li-rich component and the rate of degradation.

Fig. 2b shows the current density of Mg and Li ions after the direct contact at an immersion time of 3000 s (average of values between 2800 s and 3200 s, $i_{0,Mg}$, $i_{0,Li}$). Mg and Li release increase with increasing Li fraction, showing a higher corrosion rate. The ratio of released Mg and Li ions can be determined to identify not only the change in rate but also changes in the degradation process and the Li release. It is given in

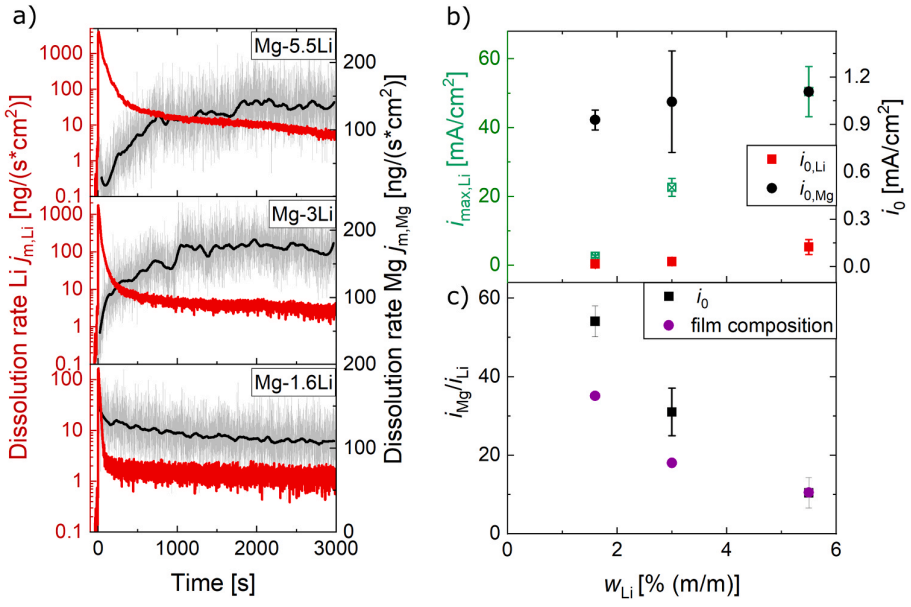

Fig. 2. Ion release of Mg-Li alloys at E_{OCV}. a) Dissolution rate j_m of Mg and Li over 3000 s starting at the contact of the sample with 15 mmol HBSS. For better visualisation of both the peak at the start and the later release, the rate for Li is plotted logarithmically. b) Height of peak at the beginning of Li release ($i_{max,Li}$) and dissolution current density of Mg and Li after 3000 s ($i_{0,Li}$, $i_{0,Mg}$). c) Calculated ratio of $i_{0,Mg}/i_{0,Li}$ (see b) and ratio calculated from the composition of the entire film.

Fig. 2c, additional to the ratio available in the bulk of the film itself determined from the average composition in the overall alloy thin film. For Mg-1.6Li, a higher Mg fraction is released. The difference to the bulk values then shrinks until a ratio similar to bulk is found for Mg-5.5Li. Thus, a preferred release of Mg or a depletion of Li in the layer under the direct (Li-rich) surface can be assumed for Mg-Li with low Li content. It has to be noted that this ratio is determined after relatively short times and, therefore, does not give information about the release from the bulk of the thin film after longer immersion times.

In Fig. 3, the Mg:Li ratio over the 50 min of immersion is shown for Mg-1.6Li and Mg-3Li to identify the influence of time. The time resolved analysis can give further insight into a possible formation of passivation or a change of surface to bulk. After the first peak of Li release, a ratio higher than in the film is directly present and relatively stable or slightly increasing for Mg-1.6Li, while an increase in the ratio is measured for Mg-3Li. The slower and ongoing increase could be influenced by a longer influence of a likely Li-rich layer (as determined by the Li peak measured at the beginning) for Mg-3Li before a higher Mg release is reached, either due to depletion of Li or the preferred release of Mg. The steady state as observed for Mg-1.6Li is not found for Mg-3Li during the first 50 min of immersion.

The E_{OCV} measured during these experiments determined after 2000 s- 3000 s of immersion decreases from -1.71 ± 0.07 V for Mg-1.6Li to -1.86 ± 0.01 V for Mg-3Li. Since Li has a lower electrode potential than Mg, it is expected that the overall potential of the MgLi alloy is reduced with increasing Li content.

Fig. 4 shows the ion release under anodic and cathodic polarisation and, therefore, under an either enhanced (+0.2 V vs. E_{OCV}) or suppressed (-0.5 V vs. E_{OCV}) degradation. The potentials were applied for 15 min after immersion at E_{OCV} for stabilisation (see Fig. 1a). Additionally, samples were held at −0.9 V vs. Ag/AgCl (anodic polarisation) since previous studies on β-Mg-Li found a change in composition and, thus, dissolution of a passivating layer above −1.05 V vs. Ag/AgCl [43]. The current measured by the flow cell decreases to around −0.009 mA at −0.5 V vs. E_{OCV} and increases to about 0.01 mA at +0.2 V vs. E_{OCV} and to 0.02–0.03 mA at −0.9 V vs. Ag/AgCl for both sample types (supplementary figure 1). For Mg-3Li, a continuous further decrease/increase is determined during the application of the constant voltage. In Fig. 4, a step-like increase in both Mg and Li release for an anodic polarisation is found with the highest increase in dissolution rate at −0.9 V vs. Ag/AgCl due to the enhanced dissolution kinetics. For Mg release, both anodic polarisations lead to similar dissolution rate changes. While the Mg signal is nearly completely suppressed at cathodic polarisation, especially for Mg-3Li, no identifiable step and a continuing release of Li is measured. This can be affected by the lower electrode potential of Li and the continuing influence of the first strong release peak. The ratio of dissolution current density of Mg:Li for an enhanced potential increases, thus indicating an increased Mg release, especially for −0.9 V vs. Ag/AgCl (supplementary table 2).

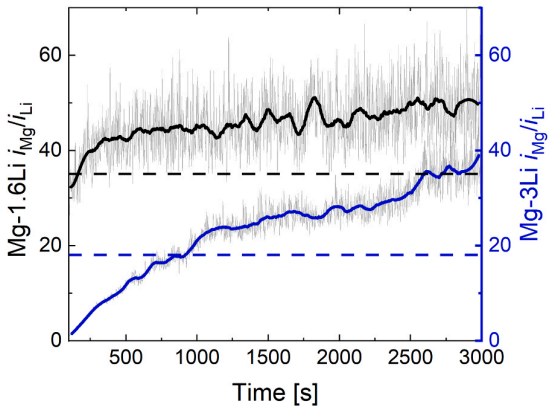

Fig. 3. Ratio of dissolution current density of Mg and Li i_{Mg}/i_{Li} for Mg-1.6Li and Mg-3Li at E_{OCV} over 3000 s. Due to the high release of Li at the beginning, the ratio is shown starting at 100 s. The ratio in the bulk, calculated from the composition of the alloy, is given by dashed lines.

A continuous voltage increase from E_{OCV} to −0.5 V vs. Ag/AgCl is performed on all sample types (LSV). For conditioning, the samples are previously held at a voltage of +0.2 V vs. E_{OCV} for 15 min (Fig. 1b) to enhance the corrosion and, therefore, the formation of corrosion products and passivation layers. Fig. 5a shows the electrical current density measured for one sample per type. For all types, a region of passivation can be found. Exemplary release rate curves vs. the applied voltage are given in Fig. 5b (data sets of 2 samples per type vs. time can be found in supplementary figure 2). In general, the release increases with enhanced voltage. Additionally, a plateau or a change in release around a potential of −1.25 V to −0.75 V occurs before the ion release further increases. For Mg-1.6Li and Mg-3Li, a stabilisation or even decrease of release of both Mg and Li occurs. While the release increase starts again at around -0.75 V for Mg-1.6Li, for Mg-3Li, an additional drop or change in slope is visible around this voltage. Mg-5.5Li only shows short continuous release before the dissolution rate increases with a similar slope as before the passivation region. The difference in the release profiles is even more visible when comparing the ratio of i_{Mg}/i_{Li} (Fig. 5c). The ratio increases slightly for Mg-1.6Li from around −1.2 V and shows a sharp increase and decrease around the threshold voltage for Mg-3Li. A continuous increase over the whole measurement is shown for Mg-5.5Li. Thus, even though a change in the release profile of the individual ions occurs for the mixed-phase material, this does not affect the released ratio in the passivation region specifically. The composition of a passivating layer does not differ from the ratio in the thin film for the material with a second phase. For pure hcp, in both cases, a shift to more Mg release can be found, even though the ratio is already higher than present in the bulk material. A short increase in the ratio for Mg-3Li could hint at a higher concentration of Mg in the surface film but no increased availability for corrosion, while Mg-1.6Li shows a preferred release of Mg even of the material itself after reaching −1 V.

3.2. Release over 3 days

The release of Mg and Li of the three different types of Mg-Li thin films during an immersion time of 3 days in HBSS at a pH of 7.4 and a temperature of 37 °C is analysed by ICP-MS measurements on extracted solution. Fig. 6a and 6b show the dissolved Li and Mg mass (overall released mass until the point of measurement) and the dissolved mass normalised with the element mass available in the as-prepared film.

A higher Li fraction in the film leads to more Li mass released. The Li content of Mg-1.6Li and Mg-3Li is continuously dissolved, and when the Li content of the samples itself is taken into account, no significant difference is determined. Thus, the release in Li is proportional to the Li amount in the film for those samples. The Li release slows down after longer immersion times, hinting at a possible decrease in corrosion rate or passivation over time. For Mg-5.5Li, a much higher release and higher deviation of measured ion masses can be determined compared to the other alloys.

The Mg release in Fig. 6b does not show substantial differences between the alloys. Since Mg is the main component in the weight of all alloys, dividing by the mass in the film also does not significantly influence the results. While after immersion times of up to 24 h, Mg-1.6Li and Mg-3Li show similar release, the release after 72 h for Mg-3Li is lower. However, the data for Mg-3Li after 72 h also shows the highest standard deviation. In Fig. 6c, the fraction of released Mg in comparison to Li mass is given for further insight into the ion release process. Additionally, the calculated fractions are marked by dashed lines for each alloy. For both Mg-1.6Li and Mg-3Li, the ratio decreases during immersion, with Mg-1.6Li samples having a higher Mg fraction after 1 h than present in the film, while Mg-3Li already shows a release similar to

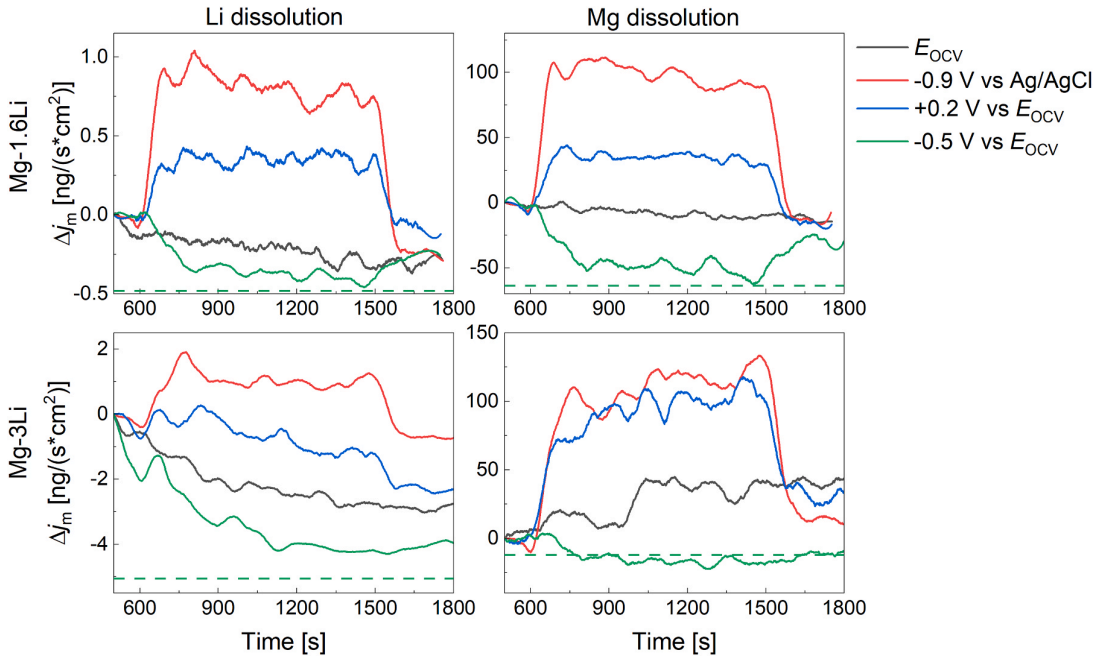

Fig. 4. Change of dissolution rate (Δj_m) of Li (a,c) and Mg (b,d), measured for Mg-1.6Li (a,b) and Mg-3Li (c,d) while holding the samples at constant voltages (E_{OCV} (Mg-1.6Li: −1.77 V, Mg3Li: −1.94 V vs. Ag/AgCl), E_{OCV} +0.2 V (Mg-1.6Li: −1.74 V, Mg3Li: −1.72 V vs. Ag/AgCl), E_{OCV} −0.5 V (Mg-1.6Li: −2.23 V, Mg3Li: −2.39 V vs. Ag/AgCl), −0.9 V vs. Ag/AgCL reference electrode) for 15 min after 10 min E_{OCV} measurement. The change is defined as the difference to the dissolution rate at E_{OCV} after 500 s. Additionally, the dashed line marks the dissolution rate change to reach a total dissolution rate j_m=0 ng/(s*cm^2) for a voltage of E_{OCV}-0.5 V to identify if the dissolution is completely suppressed.

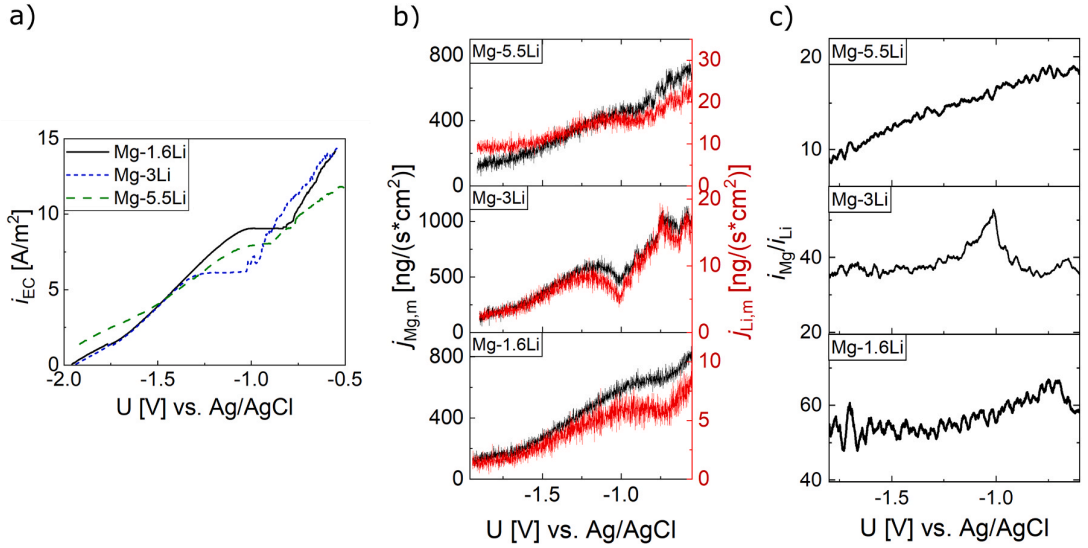

Fig. 5. LSV from E_{OCV} to −0.5 V vs. Ag/AgCl of Mg-1.6Li, Mg-3Li and Mg-5.5Li thin films. a) Current density measured in a flow cell with the potentiostat. b) Dissolution rate of Mg and Li over applied voltage. c) Ratio of dissolution current density of Mg and Li calculated from dissolution rates over applied voltage.

the ratio in the sample. The preferred Li release is then visible for both alloy types from 4 h to 72 h of immersion. Thus, while the short-term in-situ measurement showed a preferred Mg release after the first peak of Li release, which is also visible in the first hour of measurement here, this changes to a preferred release of Li, possibly due to the higher activity of Li. Due to the higher availability of Li in Mg-3Li, the first preferred Mg release is shorter, and thus, after 1 h, the preferred release changed. Mg-5.5Li again shows the highest deviations but, in general, a higher Li than Mg release after the beginning with an increasing ratio due to a very high preferred Li release in the first hour, which was already shown during the short-term degradation. While the single-phase degradation is therefore driven by the overall degradation and the preferred release of the more active species is available but influenced by a Li-depleted start of corrosion, an addition of a second phase might change the behaviour to a strong release of the highly reactive second phase by galvanic coupling.

By taking into account the results of enhanced preferred Mg dissolution after a pitting potential is applied in in-situ measurements, the

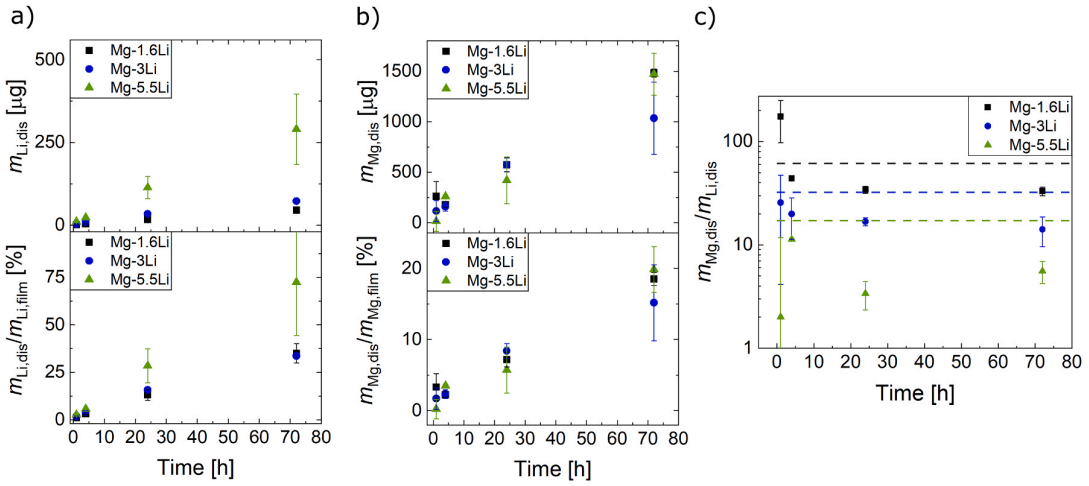

Fig. 6. 3-day ion release study in HBSS (155 mmol) at a pH of 7.4 and a temperature of 37 °C, determined by ICP-MS measurements on extracted solution. a) Total Li mass dissolved until measurement time and percentage of mass released with respect to the overall mass of Li available in the film. b) Total Mg mass released until measurement time and percentage of mass released with respect to the overall mass of Mg available in the film. c) Ratio of dissolved Mg and Li mass. The mass ratio present in the thin films (calculated from film composition) is marked with dashed lines.

change of preferred release might also be additionally influenced by a formation of corrosion products mainly containing Mg and, therefore, reducing the Mg release in comparison to Li over time.

3.3. Surface composition

As identified in the release studies, the surface composition and films

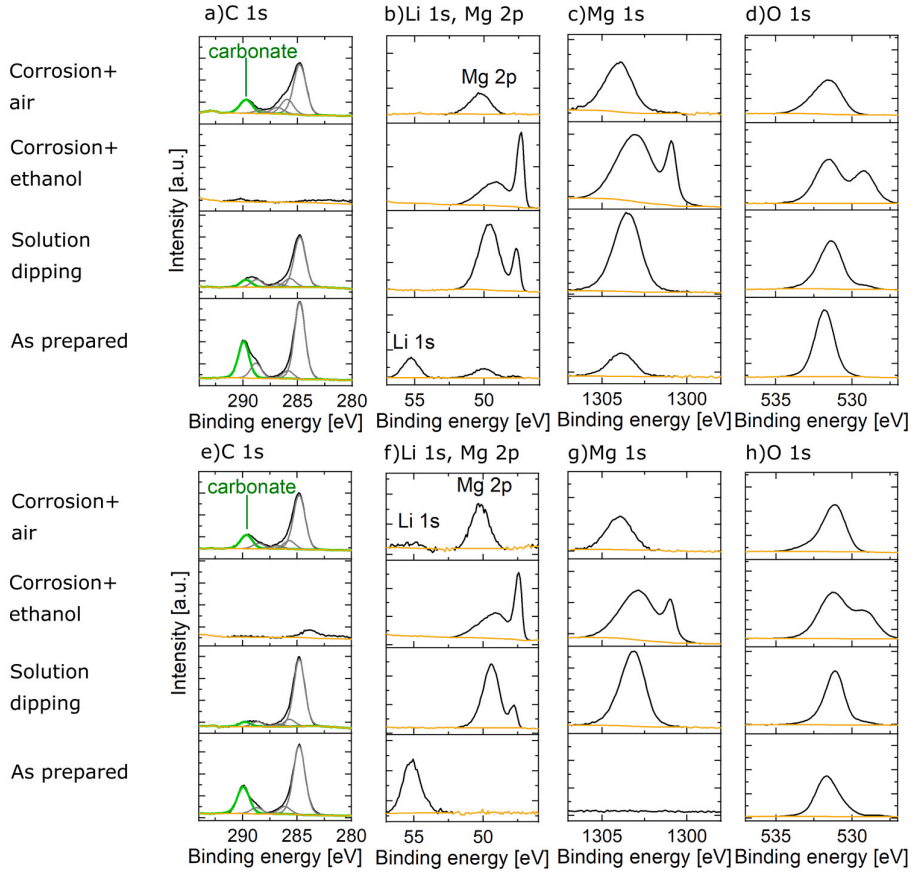

Fig. 7. XPS data of Mg-1.6Li (a-d) and Mg-3Li (e-h). a,e) C 1 s (the carbonate peal is marked on the left), b,f) Li 1 s and Mg2p, c,g) Mg 1 s, d,h) O 1 s. For each sample and measured signal, 4 samples are compared: as prepared (sputtered sample), sample dipped in solution shortly before the measurement, sample corroded for 1 h in solution and stored in air and sample corroded for 1 h in solution and stored in ethanol before measurement.

formed on as prepared and corroded samples play a significant role in the degradation process.

The surface composition is analysed by XPS on the as-prepared samples, after dipping them in solution and after corrosion for 1 h. The C 1 s, O 1 s, Mg 1 s and Li 1 s (+Mg 2p) spectra are given in Fig. 7a-d for Mg-1.6Li and Fig. 7e-h for Mg-3Li. In the as-prepared state, only for Mg-1.6Li, a Mg signal is measured on the surface. Both sample types show a strong Li 1 s peak, indicating an accumulation of Li-rich phases on the surface. The C 1 s signal also shows a carbonate peak in the as-sputtered state. For Mg-1.6Li, mainly one sharp peak (mainly hydroxide) is found in the O 1 s spectrum, while for Mg-3Li, an additional shoulder at lower binding energies indicates the presence of oxides.

The effect of contact with solution on the surface composition is studied by dipping a sample into the solution shortly before measurement. After the first contact with the solution, the Li signal disappears for both sample types while a Mg peak is now identified for both samples. Together with the sharp release of Li at the beginning of the in-situ measurements, this leads to the assumption that a Li-rich layer exists on the surface before the immersion, which makes the Li ions readily available for dissolution. The layer is thicker or more complete for films with higher Li fraction, enhancing the Li and reducing the Mg signal of Mg-3Li in comparison to Mg-1.6Li. Thus, first contact with the solution leads to a decrease of Li and carbonate content on the surface, leading to the assumption of a Li_2CO_3 layer present before, which is water soluble.

Measurements on samples corroded for 1 h in solution are carried out after storing the sample in ethanol or air for transport. As shown in Fig. 7, this influences the sample surface significantly. A strong Mg peak is still present for samples stored in ethanol to prevent contact with air, and no strong Li accumulations occur on the surface. In addition to a broadened Mg peak, a sharp additional peak (Mg-1.6Li, Mg-3Li) of Mg metal is found, thus, the oxide/hydroxide layer on the surface is thinner than 5 nm. The O 1 s signal consists of two prominent peaks at around 531.5 eV and 529 eV. While the peak at higher energy is present already on the as-prepared samples, the peak at lower energy is shown especially for Mg-3Li as a more minor shoulder after dipping the sample in solution; therefore, it is not only a signal influenced by ethanol storage. The C signal for all sample types is strongly reduced. Storing the samples in air leads to a C 1 s and O 1 s signal similar to the as prepared samples. The O 1 s signal also slightly broadened with a shoulder at higher energies, indicating the presence of carbonates. For Mg-3Li, a Li peak and carbonate can be detected. In comparison, Mg-1.6Li samples do not show any Li signal with a slight reduction and broadening in the Mg peak. Thus, the Li compound containing surface layer is formed after corrosion and contact in air, but the formation speed is dependent on the Li available for the formation since Li is present close to the surface and less diffusion is necessary for the formation.

Thus, contact with solution and corrosion does not increase the Li and carbonate content on the surface during the corrosion time of 1 h of the thin films, but contact with air does for hcp Mg-Li alloys.

Additional elements in corrosion products, such as Ca and P, can be detected on the corroded samples (stored in ethanol) (Fig. 3 supplementary). The presence of Ca and phosphates is discussed to reduce the corrosion of Mg alloys, also with additional carbonates, in a medium with added salts to simulate physiological conditions [47].

4. Discussion

4.1. Surface in air

In general, for Mg materials, a layer of MgO which partially reacts to $Mg(OH)_2$ is formed in air [27]. Yan et al. propose for Mg-Li alloys that the $Mg(OH)_2$ can react further to Mg carbonate containing compounds if stored in air, which leads to a reduction in $Mg(OH)_2$ [48]. However, for the samples in this study, the Mg signal in general is reduced and completely absent for Mg-3Li, thus, another compound is attributing to the surface composition. High Li and carbonate signals were found on the sample surface. Therefore, the formation of a Li and carbonate-containing layer is found on all sample types with a thicker or more complete layer for Mg-3Li. Li_2CO_3 is a common component formed in air on Mg-Li alloys with high Li concentration and β-phase [42,49]. For high Li concentrations, a large amount of Li is available close to the surface and can readily react. Additionally, further Li can be transported to the surface, leading to a Li-depleted zone under the surface layer [49]. However, since the PBR (Pilling-Bedworth ratio) is between 1 and 2 for all Li fractions, it can also form stably on all α-Mg-Li [26]. To support this assumption, it should be noted that Xiang et al. also found Li_2CO_3 films on a Mg-5Li-1Al hcp alloy [30].

The occurrence of a surface layer consisting mainly of Li components is also proven in the in-situ release studies by the sharp release of Li at the beginning of immersion. The peak height increases from Mg-1.6Li<Mg-3Li <Mg-5.5Li, indicating a higher amount of Li components formed when the Li content is increased, which is not necessarily dependent on the phase. Since Li_2CO_3 is water soluble [42], the layer dissolves and, therefore, does not influence the corrosion resistance of both Mg-1.6Li and Mg-3Li. The dissolution is also proven by the disappearance of the Li signal in XPS after a first short immersion. Even though it can be theoretically formed in solution, this highly depends on the availability of Li ions and carbonate and the pH [50]. Here, the measurements were performed at a pH of around 7.4, while Li_2CO_3 is more stable for alkaline solutions. The diffusion of Li to the surface can then lead to a Li-depleted, Mg-rich area underneath the surface layer, which also adds to the strong Mg signal detected by XPS after the short-term immersion.

After corrosion, samples were stored again for approximately 7 days in air. Since, for both alloys, the samples stored in ethanol after corrosion showed no Li and low carbonate signal, the change can be attributed to the exposure to air. Yan et al. found that exposure to air after corrosion leads to the formation of Li_2CO_3 on the sample surface of a bcc Mg-Li-based alloy after 60 h [48] and starts already after less than 3 hours [42]. The thickness of the Li_2CO_3 films on Mg-Li will further grow over time since more Li is transported to the surface [48]. The formation, however, is not limited to β-phase materials. While the Li diffusion coefficient in hcp Mg is lower than in β-Mg-Li [51,52], Li is still available close to the surface and can react with CO_2 from the air. Additionally, it was found that Li segregates at grain boundaries for Mg-Li alloys, also for hcp Mg-Li [53], therefore enabling fast transport due to grain boundary diffusion. Since the columnar growth or long grains for both Mg-1.6Li and Mg-3Li offer many grain boundaries and sometimes void formation [8] leading to the film surface, this can further facilitate the transport. The amount of Li available is then influenced by the Li fraction in the film. Mg-3Li presents a Li and carbonate signal on the surface after corrosion and storage in air, even though the Li signal is very low. Therefore, the formation depends on the Li content present in the hcp Mg-Li due to the higher availability close to the surface. It can be assumed that this not only increases the layer thickness as discussed for the as-prepared samples but also the speed of a detectable layer; thus, the formation of such a layer on corroded Mg-1.6Li samples after longer storage time might be possible.

4.2. Ion release and degradation

The ion release due to the degradation of the Mg-Li thin films was tested directly after the immersion in-situ and over longer time. The degradation can change over time due to the release and depletion of one element or the further prevention of fast corrosion due to corrosion products forming protective layers on the surface. For single-phase hcp Mg-Li, a corrosion similar to Mg is expected. For Mg, a thin, dense layer of MgO and a thicker, porous layer of $Mg(OH)_2$ is formed on the surface, which is more stable in an alkaline solution [50]. The pH close to the surface increases during the corrosion, stabilising such layers. The corrosion is driven by filiform corrosion with a cathodic corrosion front [26]. By adding Li, in general, the hydrogen evolution effect of Mg alloys

decreases and even though the passivation is not strong, additional compounds such as Li_2CO_3 or LiOH have been found on the surface of Mg-Li based samples [29,30].

In general, the Li release is expected to increase with the Li content available in the film, which was found for both short-term and long-term measurements. However, the release is influenced by not only the Li content but also the degradation process, in the simplest case, the corrosion rate. In a previous study, the corrosion rate of Mg-1.6Li was determined to be the lowest, while the corrosion rate increased due to the change in orientation, higher activity of Li and galvanic coupling because of the formation of a second phase for Mg-5.5Li [8]. A higher Li content leads to a higher corrosion rate and, thus, to a higher release in both Mg and Li ions. This can be even more pronounced if the increase in Li content also changes the orientation of the material and the microstructure [8]. This is in agreement with the higher overall ion release and, thus, corrosion rate measured herein.

Both α-Mg-Li alloys show a preferred Mg release after the first peak of Li release in the first hour, and there is a nearly direct start of Mg release after immersion. Thus, after the dissolution of Li-rich compounds, Li is no longer released preferentially, and a larger amount of Mg is available, possibly due to the depletion after Li reacting on the surface. In the 3-day measurements, both α-phase materials show a similar trend of release with a higher release of Mg at the beginning, as already mentioned for in-situ measurements. However, the results show a preferred dissolution of Li over longer immersion times, possibly due to the lower electrochemical potential [50]. The preferred dissolution of Li is also observed in the ion release studies at constant voltage. While the Mg release is nearly completely suppressed for both materials at cathodic polarisation, Li release still occurs, especially for Mg-3Li. Thus, the release is not a continuous release of both materials present in the phase but preferred of one material even though no two different phases can be found. Since the Li was found to be accumulating at the grain boundaries [53], it is possible that these Li-rich areas are corroding preferentially; however, further studies would be needed to prove the effect on the ion release directly.

The corrosion of α-Mg-Li, thus, changes from surface to bulk of the thin films and can be described by three phases (Fig. 8): 1. Li release from Li containing surface film formed in air, 2. Preferred release of Mg from Mg-rich area under the surface, 3. Continuous release from the bulk of the film with preferred Li dissolution. The release of Mg is reduced over time while the Li release is less reduced; thus, in addition to the higher activity of Li, the incorporation of Mg in corrosion products might additionally reduce the Mg release and lead to a higher concentration of Li in comparison to Mg. The anodic polarisation by sweeping to values above passivation and the start of pitting shows an increase of Mg release, thus indicating the presence of a Mg-rich corrosion product. The formation of the corrosion products can then change decrease corrosion over time [54] together with additional components such as phosphates (Ca, P) formed due to the additional salts in the solution. Li-containing components have not been found in the outer layer after corrosion without storage in air, and after 1 h of immersion, only a thin layer of oxides and hydroxides is formed. Thus, the Mg metal underneath is still detectable. Further measurements would be necessary to identify the composition of the corrosion products in detail which is not

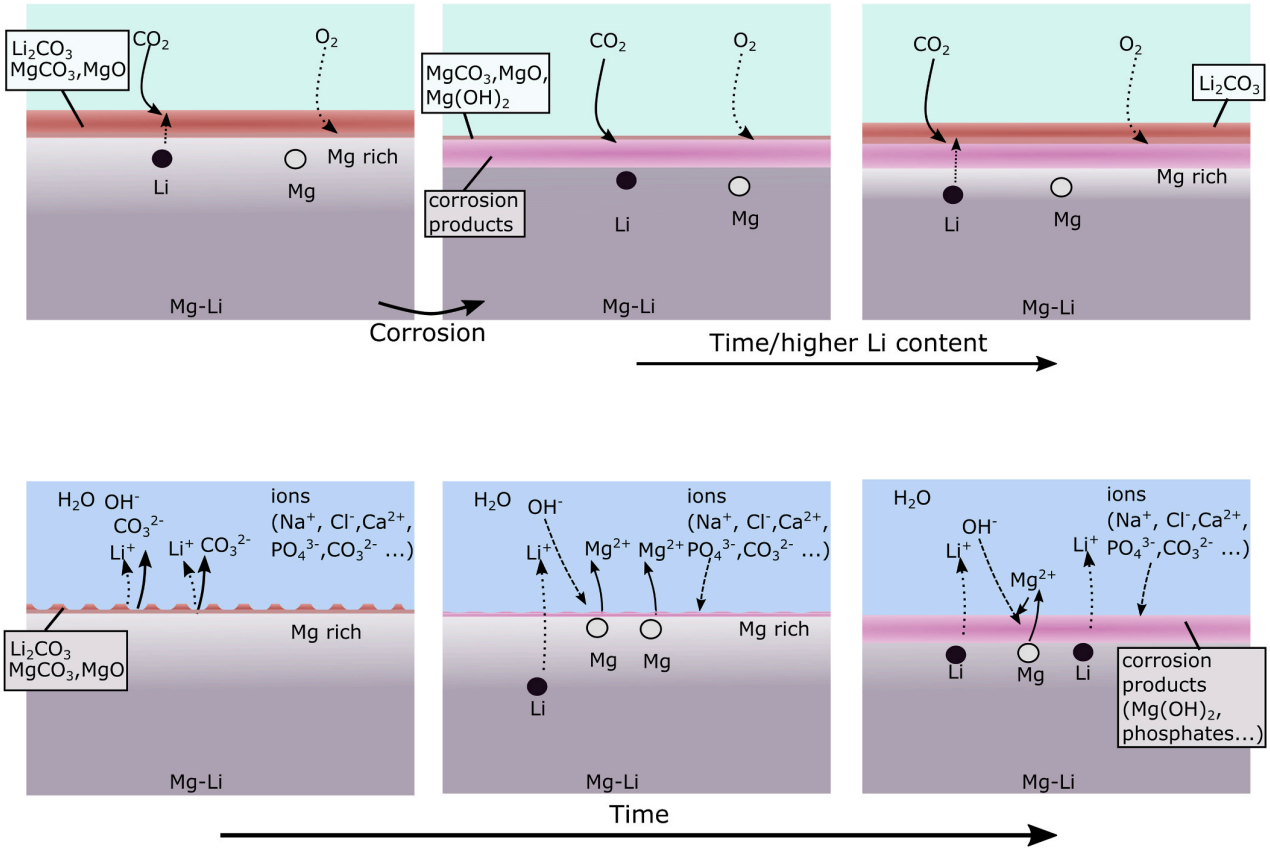

Fig. 8. Schematics of possible processes of the surface layer formation and degradation of hcp Mg-Li thin films a)-c) in air and d)-f) in solution. a) Formation of a Li_2CO_3 and MgO containing surface layer in air on as sputtered samples, b) formation of Mg-rich surface layers in air after short storage time and low Li content after corrosion and c) development of Li_2CO_3 on corroded samples after longer storage time in air for films with higher Li content. d) The start of the contact with solution leads to a dissolution of the Li-rich carbonate layer, followed by e) preferred, strong Mg release in short-term corrosion, before f) the release switches to preferred Li release, possibly due to preferred Li release and formation of corrosion products.

part of this study.

For the application of such films, the Li release needs to be determined over time. While the therapeutic range is discussed to be around 0.4–1.2 mM [55], this cannot be directly compared to the concentrations reached in the 3-day studies due to the influence of cells or placement *in vivo* on the corrosion rate [56], and the actual volume of solution and the flow on the final concentration. However, this study and the preferred release of Li identify that the Li concentration available cannot be directly derived from the degradation rate of the films and will change, especially during the beginning of placement and after long immersion times when Li is depleted. Especially the first Li-rich layer might lead to higher Li concentrations, and removal of such layer by, e.g., previous immersion in solution might be necessary.

5. Conclusions

Mg-Li thin films in the hcp phase were studied with respect to the surface chemistry and degradation by a combination of in-situ and ex-situ techniques for determining the ion release and additional analysis of the surface composition by XPS. A process of the formation of surface layers in air and during corrosion and preferred ion release is described:

- It was found that both sputtered hcp alloys (Mg-1.6Li and Mg-3Li) formed Li carbonate containing compounds on the surface after long-term exposure to air. This layer is also formed if corroded samples are exposed to air. However, the development is mainly visible for Mg-3Li films after 7 days due to the higher Li content and, thus, availability of the element.
- During degradation in Hanks' balanced salt solution, this surface layer is dissolved, monitored by a high release in Li and reduction in both carbonate and Li signal in XPS. The layer does, therefore, not contribute to the passivity and influence on the corrosion resistance of the hcp thin films.
- While a higher Mg concentration can be found during the first hour of immersion, a higher Li concentration than present in the film is determined over a longer time due to the preferred release of Li and the formation of Mg-rich corrosion products (containing oxides and hydroxides), which form a passivating layer and decrease the corrosion rate.

The corrosion process and ion release are time-dependent and change from direct contact in solution to long-term corrosion. The combination of in-situ short-term and studies with longer immersion times, as described in this work, is therefore beneficial to gain a more comprehensive picture of the complex degradation behaviour of the thin films.

Understanding the degradation process and reactions in air is also of interest for other applications of MgLi in fields such as lightweight construction. For the medical field specifically, the ion release results also highlight the importance of carefully analysing the ion release when discussing such thin films for application as biodegradable reservoirs for treatments with dissolving elements. For an optimisation of the treatment, it is not sufficient to determine the Li release by degradation rate since a change over time occurs. The change in the ratio of both ions must also be considered if both can influence the therapeutic effect of the other element involved. Furthermore, a treatment or solution dipping before tests *in vitro* or *in vivo* might be beneficial to avoid the impact of the high Li release at the start.

CRediT authorship contribution statement

Ulrike Westernströer: Investigation. **Dieter Garbe-Schönberg:** Supervision, Resources. **Lisa Hanke:** Writing – review & editing, Writing – original draft, Investigation, Formal analysis, Conceptualization. **Lukas Kalchgruber:** Writing – review & editing, Methodology, Investigation. **Eckhard Quandt:** Writing – review & editing, Supervision, Funding acquisition. **Markus Valtiner:** Writing – review & editing, Supervision, Resources, Methodology.

Declaration of Competing Interest

The authors declare that they have no known competing financial interests or personal relationships that could have appeared to influence the work reported in this paper.

Data Availability

Data will be made available on request.

Acknowledgements

This work was supported by the DFG in the framework of the research training group 2154 – Materials for Brain (project 270394294). We also acknowledge the CzechNanoLab project LM2018110 funded by MEYS CR for the financial support of the XPS measurements at CEITEC Nano Research Infrastructure.

Appendix A. Supporting information

Supplementary data associated with this article can be found in the online version at doi:10.1016/j.corsci.2024.112361.

References

[1] J.-W. Lee, H.-S. Han, K.-J. Han, J. Park, H. Jeon, M.-R. Ok, H.-K. Seok, J.-P. Ahn, K. E. Lee, D.-H. Lee, S.-J. Yang, S.-Y. Cho, P.-R. Cha, H. Kwon, T.-H. Nam, J.H.L. Han, H.-J. Rho, K.-S. Lee, Y.-C. Kim, D. Mantovani, Long-term clinical study and multiscale analysis of in vivo biodegradation mechanism of Mg alloy, Proc. Natl. Acad. Sci. U. S. A. 113 (2016) 716–721, https://doi.org/10.1073/pnas.1518238113.

[2] V. Tsakiris, C. Tardei, F.M. Clicinschi, Biodegradable Mg alloys for orthopedic implants – a review, J. Magnes. Alloy. 9 (2021) 1884–1905, https://doi.org/10.1016/j.jma.2021.06.024.

[3] G. Uppal, A. Thakur, A. Chauhan, S. Bala, Magnesium based implants for functional bone tissue regeneration – A review, J. Magnes. Alloy. 10 (2022) 356–386, https://doi.org/10.1016/j.jma.2021.08.017.

[4] S. Zaatreh, D. Haffner, M. Strauß, K. Wegner, M. Warkentin, C. Lurtz, C. Zamponi, W. Mittelmeier, B. Kreikemeyer, R. Willumeit-Römer, E. Quandt, R. Bader, Fast corroding, thin magnesium coating displays antibacterial effects and low cytotoxicity, Biofouling 33 (2017) 294–305, https://doi.org/10.1080/08927014.2017.1303832.

[5] A. Atrens, M. Liu, N.I. Zainal Abidin, Corrosion mechanism applicable to biodegradable magnesium implants, Mater. Sci. Eng. B 176 (2011) 1609–1636, https://doi.org/10.1016/j.mseb.2010.12.017.

[6] X. Li, X. Liu, S. Wu, K.W.K. Yeung, Y. Zheng, P.K. Chu, Design of magnesium alloys with controllable degradation for biomedical implants: from bulk to surface, Acta Biomater. 45 (2016) 2–30, https://doi.org/10.1016/j.actbio.2016.09.005.

[7] L. Wei, Z. Gao, Recent research advances on corrosion mechanism and protection, and novel coating materials of magnesium alloys: a review, RSC Adv. 13 (2023) 8427–8463, https://doi.org/10.1039/D2RA07829E.

[8] L. Hanke, L.K. Jessen, F. Weisheit, K. Bhat, U. Westernströer, D. Garbe-Schönberg, R. Willumeit-Römer, E. Quandt, Structural characterisation and degradation of Mg-Li thin films for biodegradable implants, Sci. Rep. 13 (2023) 12572, https://doi.org/10.1038/s41598-023-39493-9.

[9] Y. Sun, H. Zhang, Y. Zhang, Z. Liu, D. He, W. Xu, S. Li, C. Zhang, Z. Zhang, Li–Mg–Si bioceramics provide a dynamic immuno-modulatory and repair-supportive microenvironment for peripheral nerve regeneration, Bioact. Mater. 28 (2023) 227–242, https://doi.org/10.1016/j.bioactmat.2023.05.013.

[10] L. Li, X. Peng, Y. Qin, R. Wang, J. Tang, X. Cui, T. Wang, W. Liu, H. Pan, B. Li, Acceleration of bone regeneration by activating Wnt/β-catenin signalling pathway via lithium released from lithium chloride/calcium phosphate cement in osteoporosis, Sci. Rep. 7 (2017) 45204, https://doi.org/10.1038/srep45204.

[11] F. He, X. Yuan, T. Lu, Y. Wang, S. Feng, X. Shi, L. Wang, J. Ye, H. Yang, Preparation and characterization of novel lithium magnesium phosphate bioceramic scaffolds facilitating bone generation, J. Mater. Chem. B 10 (2022) 4040–4047, https://doi.org/10.1039/D2TB00471B.

[12] A.E. Kocman, I. Dag, T. Sengel, E. Soztutar, M. Canbek, The effect of lithium and lithium-loaded hyaluronic acid hydrogel applications on nerve regeneration and recovery of motor functions in peripheral nerve injury, Rend. Lince-.-. Sci. Fis. E Nat. 31 (2020) 889–904, https://doi.org/10.1007/s12210-020-00919-5.

[13] K. Bhat, L. Schlotterose, L. Hanke, H. Helmholz, E. Quandt, K. Hattermann, R. Willumeit-Römer, Magnesium-lithium thin films for neurological applications–An *in vitro* investigation of glial cytocompatibility and

neuroinflammatory response, Acta Biomater. 178 (2024) 307–319, https://doi.org/10.1016/j.actbio.2024.02.018.
[14] A. Vallée, J.-N. Vallée, Y. Lecarpentier, Parkinson's disease: potential actions of lithium by targeting the WNT/β-catenin pathway, oxidative stress, inflammation and glutamatergic pathway, Cells 10 (2021) 230, https://doi.org/10.3390/cells10020230.
[15] A. Can, T.G. Schulze, T.D. Gould, Molecular actions and clinical pharmacogenetics of lithium therapy, Pharmacol. Biochem. Behav. 123 (2014) 3–16, https://doi.org/10.1016/j.pbb.2014.02.004.
[16] C. Volkmann, T. Bschor, S. Köhler, Lithium treatment over the lifespan in bipolar disorders, Front. Psychiatry 11 (2020) 377, https://doi.org/10.3389/fpsyt.2020.00377.
[17] O.V. Forlenza, V.J.R. De-Paula, B.S.O. Diniz, Neuroprotective effects of lithium: implications for the treatment of Alzheimer's disease and related neurodegenerative disorders, ACS Chem. Neurosci. 5 (2014) 443–450, https://doi.org/10.1021/cn5000309.
[18] M. Gitlin, Lithium side effects and toxicity: prevalence and management strategies, Int. J. Bipolar Disord. 4 (2016) 27, https://doi.org/10.1186/s40345-016-0068-y.
[19] J.A.M. Maier, L. Locatelli, G. Fedele, A. Cazzaniga, A. Mazur, Magnesium and the brain: a focus on neuroinflammation and neurodegeneration, Int. J. Mol. Sci. 24 (2023) 223, https://doi.org/10.3390/ijms24010223.
[20] A.E. Kirkland, G.L. Sarlo, K.F. Holton, The role of magnesium in neurological disorders, Nutrients 10 (2018) 730, https://doi.org/10.3390/nu10060730.
[21] C. Xu, S. Wang, H. Wang, K. Liu, S. Zhang, B. Chen, H. Liu, F. Tong, F. Peng, Y. Tu, Y. Li, Magnesium-based micromotors as hydrogen generators for precise rheumatoid arthritis therapy, Nano Lett. 21 (2021) 1982–1991, https://doi.org/10.1021/acs.nanolett.0c04438.
[22] T.A. Ranathunge, D.G.G.P. Karunaratne, R.M.G. Rajapakse, D.L. Watkins, Doxorubicin loaded magnesium oxide nanoflakes as pH dependent carriers for simultaneous treatment of cancer and hypomagnesemia, Nanomaterials 9 (2019) 208, https://doi.org/10.3390/nano9020208.
[23] A. Nyabadza, C. Shan, R. Murphy, M. Vazquez, D. Brabazon, Laser-synthesised magnesium nanoparticles for amino acid and enzyme immobilisation, OpenNano 11 (2023) 100133, https://doi.org/10.1016/j.onano.2023.100133.
[24] W. Zhou, Y. Zhang, S. Meng, C. Xing, M. Ma, Z. Liu, C. Yang, T. Kong, Micro-/nano-structures on biodegradable magnesium@PLGA and their cytotoxicity, photothermal, and anti-tumor effects, Small Methods 5 (2021) 2000920, https://doi.org/10.1002/smtd.202000920.
[25] L. Dong, X. Liu, J. Liang, C. Li, Y. Dong, Z. Zhang, Corrosion behavior of a eutectic Mg–8Li alloy in NaCl solution, Electrochem. Commun. 129 (2021) 107087, https://doi.org/10.1016/j.elecom.2021.107087.
[26] C.Q. Li, D.K. Xu, X.-B. Chen, B.J. Wang, R.Z. Wu, E.H. Han, N. Birbilis, Composition and microstructure dependent corrosion behaviour of Mg-Li alloys, Electrochim. Acta 260 (2018) 55–64, https://doi.org/10.1016/j.electacta.2017.11.091.
[27] M. Taheri, M. Danaie, J.R. Kish, TEM examination of the film formed on corroding Mg prior to breakdown, J. Electrochem. Soc. 161 (2013) C89–C94, https://doi.org/10.1149/2.017403jes.
[28] B.-J. Wang, J.-Y. Luan, D.-K. Xu, J. Sun, C.-Q. Li, E.-H. Han, Research progress on the corrosion behavior of magnesium–lithium-based alloys: a review, Acta Metall. Sin. Engl. Lett. 32 (2019) 1–9, https://doi.org/10.1007/s40195-018-0847-9.
[29] C. Li, Y. He, H. Huang, Effect of lithium content on the mechanical and corrosion behaviors of HCP binary Mg–Li alloys, J. Magnes. Alloy. 9 (2021) 569–580, https://doi.org/10.1016/j.jma.2020.02.022.
[30] Q. Xiang, B. Jiang, Y. Zhang, X. Chen, J. Song, J. Xu, L. Fang, F. Pan, Effect of rolling-induced microstructure on corrosion behaviour of an as-extruded Mg-5Li-1Al alloy sheet, Corros. Sci. 119 (2017) 14–22, https://doi.org/10.1016/j.corsci.2017.02.009.
[31] C. Blawert, V. Heitmann, N. Scharnagl, M. Störmer, J. Lutz, A. Prager-Duschke, D. Manova, S. Mändl, Different underlying corrosion mechanism for Mg bulk alloys and Mg thin films, Plasma Process. Polym. 6 (2009) S690–S694, https://doi.org/10.1002/ppap.200932405.
[32] K. Schlüter, C. Zamponi, A. Piorra, E. Quandt, Comparison of the corrosion behaviour of bulk and thin film magnesium alloys, Corros. Sci. 52 (2010) 3973–3977, https://doi.org/10.1016/j.corsci.2010.08.011.
[33] Y. Liu, Y. Wu, D. Bian, S. Gao, S. Leeflang, H. Guo, Y. Zheng, J. Zhou, Study on the Mg-Li-Zn ternary alloy system with improved mechanical properties, good degradation performance and different responses to cells, Acta Biomater. 62 (2017) 418–433, https://doi.org/10.1016/j.actbio.2017.08.021.
[34] W.R. Zhou, Y.F. Zheng, M.A. Leeflang, J. Zhou, Mechanical property, biocorrosion and in vitro biocompatibility evaluations of Mg–Li–(Al)–(RE) alloys for future cardiovascular stent application, Acta Biomater. 9 (2013) 8488–8498, https://doi.org/10.1016/j.actbio.2013.01.032.
[35] K. Ogle, Atomic emission spectroelectrochemistry: real-time rate measurements of dissolution, corrosion, and passivation, Corrosion 75 (2019) 1398–1419, https://doi.org/10.5006/3336.
[36] K. Ogle, S. Weber, Anodic dissolution of 304 stainless steel using atomic emission spectroelectrochemistry, J. Electrochem. Soc. 147 (2000) 1770–1780, https://doi.org/10.1149/1.1393433.
[37] S.O. Klemm, A.A. Topalov, C.A. Laska, K.J.J. Mayrhofer, Coupling of a high throughput microelectrochemical cell with online multielemental trace analysis by ICP-MS, Electrochem. Commun. 13 (2011) 1533–1535, https://doi.org/10.1016/j.elecom.2011.10.017.
[38] S. Lebouil, O. Gharbi, P. Volovitch, K. Ogle, Mg dissolution in phosphate and chloride electrolytes: insight into the mechanism of the negative difference effect, CORROSION 71 (2015) 234–241, https://doi.org/10.5006/1459.
[39] L. Rossrucker, A. Samaniego, J.-P. Grote, A.M. Mingers, C.A. Laska, N. Birbilis, G. S. Frankel, K.J.J. Mayrhofer, The pH dependence of magnesium dissolution and hydrogen evolution during anodic polarization, J. Electrochem. Soc. 162 (2015) C333–C339, https://doi.org/10.1149/2.0621507jes.
[40] S. Thomas, O. Gharbi, S.H. Salleh, P. Volovitch, K. Ogle, N. Birbilis, On the effect of Fe concentration on Mg dissolution and activation studied using atomic emission spectroelectrochemistry and scanning electrochemical microscopy, Electrochim. Acta 210 (2016) 271–284, https://doi.org/10.1016/j.electacta.2016.05.164.
[41] L. Rossrucker, K.J.J. Mayrhofer, G.S. Frankel, N. Birbilis, Investigating the real time dissolution of mg using online analysis by ICP-MS, J. Electrochem. Soc. 161 (2014) C115–C119, https://doi.org/10.1149/2.064403jes.
[42] Y.M. Yan, A. Maltseva, P. Zhou, X.J. Li, Z.R. Zeng, O. Gharbi, K. Ogle, M. La Haye, M. Vaudescal, M. Esmaily, N. Birbilis, P. Volovitch, On the in-situ aqueous stability of an Mg-Li-(Al-Y-Zr) alloy: role of Li, Corros. Sci. 164 (2020) 108342, https://doi.org/10.1016/j.corsci.2019.108342.
[43] L. Hou, M. Raveggi, X.-B. Chen, W. Xu, K.J. Laws, Y. Wei, M. Ferry, N. Birbilis, Investigating the passivity and dissolution of a corrosion resistant Mg-33at%Li alloy in aqueous chloride using online ICP-MS, J. Electrochem. Soc. 163 (2016) C324–C329, https://doi.org/10.1149/2.0871606jes.
[44] Y. Yan, P. Zhou, O. Gharbi, Z. Zeng, X. Chen, P. Volovitch, K. Ogle, N. Birbilis, Investigating ion release using inline ICP during in situ scratch testing of an Mg-Li(-Al-Y-Zr) alloy, Electrochem. Commun. 99 (2019) 46–50, https://doi.org/10.1016/j.elecom.2019.01.001.
[45] D. Haffner, C. Zamponi, R.Lima de Miranda, E. Quandt, Micropatterned freestanding magnetron sputtered Mg-alloy scaffolds, BioNanoMat 16 (2015) 19–22, https://doi.org/10.1515/bnm-2015-0007.
[46] D. Dworschak, C. Brunnhofer, M. Valtiner, Photocorrosion of ZnO single crystals during electrochemical water splitting, ACS Appl. Mater. Interfaces 12 (2020) 51530–51536, https://doi.org/10.1021/acsami.0c15508.
[47] D. Mei, S.V. Lamaka, J. Gonzalez, F. Feyerabend, R. Willumeit-Römer, M. L. Zheludkevich, The role of individual components of simulated body fluid on the corrosion behavior of commercially pure Mg, Corros. Sci. 147 (2019) 81–93, https://doi.org/10.1016/j.corsci.2018.11.011.
[48] Y.M. Yan, O. Gharbi, A. Maltseva, X.B. Chen, Z.R. Zeng, S.W. Xu, W.Q. Xu, P. Volovich, M. Ferry, N. Birbilis, Investigating the structure of the surface film on a corrosion resistant Mg-Li(-Al-Y-Zr) Alloy, CORROSION 75 (2019) 80–89, https://doi.org/10.5006/2995.
[49] W. Xu, N. Birbilis, G. Sha, Y. Wang, J.E. Daniels, Y. Xiao, M. Ferry, A high-specific-strength and corrosion-resistant magnesium alloy, Nat. Mater. 14 (2015) 1229–1235, https://doi.org/10.1038/nmat4435.
[50] R.J. Santucci, M.E. McMahon, J.R. Scully, Utilization of chemical stability diagrams for improved understanding of electrochemical systems: evolution of solution chemistry towards equilibrium, Npj Mater. Degrad. 2 (2018) 1, https://doi.org/10.1038/s41529-017-0021-2.
[51] W. Zhong, J.-C. Zhao, First measurement of diffusion coefficients of lithium in magnesium, Materialia 11 (2020) 100674, https://doi.org/10.1016/j.mtla.2020.100674.
[52] Y. Iwadate, M. Lassouani, F. Lantelme, M. Chemla, Electrochemical study of mass transfer in Li-Mg and Li-Mg-Al alloys, J. Appl. Electrochem. 17 (1987) 385–397, https://doi.org/10.1007/BF01023304.
[53] H. Somekawa, D. Egusa, E. Abe, Grain boundary plasticity in solid solution Mg–Li binary alloy, Mater. Sci. Eng. A 790 (2020) 139705, https://doi.org/10.1016/j.msea.2020.139705.
[54] I.B. Singh, M. Singh, S. Das, A comparative corrosion behavior of Mg, AZ31 and AZ91 alloys in 3.5% NaCl solution, J. Magnes. Alloy. 3 (2015) 142–148, https://doi.org/10.1016/j.jma.2015.02.004.
[55] W. Severus, N. Kleindienst, F. Seemüller, S. Frangou, H. Möller, W. Greil, What is the optimal serum lithium level in the long-term treatment of bipolar disorder – a review? Bipolar Disord. 10 (2008) 231–237, https://doi.org/10.1111/j.1399-5618.2007.00475.x.
[56] A.H.M. Sanchez, B.J.C. Luthringer, F. Feyerabend, R. Willumeit, Mg and Mg alloys: how comparable are in vitro and in vivo corrosion rates? A review, Acta Biomater. 13 (2015) 16–31, https://doi.org/10.1016/j.actbio.2014.11.048.

3.5 Publication: Tailoring of Mg and MgLi thin-film corrosion rates with dielectric barrier discharge plasma treatment

To control the ion release for applications with different release profiles or implant shapes, the possibility of tuning the corrosion rate is advantageous. While chapter 3.2 already discusses the possibility of changing the corrosion rate during the sputtering itself, this only decreases the corrosion rate if still a microstructure with a lower corrosion rate is possible and can be formed.
In general, tuning the corrosion rate for Mg-based alloys means decreasing it since the structures need to be present in the body for a longer time so that the implant can serve its job. To further reduce the corrosion rate of Mg and MgLi thin films, an additional treatment by dielectric barrier discharge plasma was tested. The set-up for the treatment in ambient air is simple, cheap and could be easily upscaled. The surface change by reducing roughness and formation of a carbonate-containing layer reduced the corrosion rate by around 50 % without significantly changing the film's thickness.

Own contributions to the following article
(concept - 50 %, planning - 70 %, experiments - 40 %, analysis - 70 %, writing - 90 %):

- Sample preparation
- XRD, SEM/EDX investigation
- Partially potentiodynamic polarisation measurements
- Interpretation and discussion of the results
- Writing of the manuscript

JVST A
Journal of Vacuum Science & Technology A

ARTICLE

pubs.aip.org/avs/jva

Tailoring of Mg and MgLi thin-film corrosion rates with dielectric barrier discharge plasma treatment

Cite as: J. Vac. Sci. Technol. A **41**, 053109 (2023); doi: 10.1116/6.0002783
Submitted: 22 April 2023 · Accepted: 28 July 2023 ·
Published Online: 18 August 2023

Lisa Hanke,[1] Torge Hartig,[2] Felix Weisheit,[1] Tim Tjardts,[2] Tim Pogoda,[2] Franz Faupel,[2] and Eckhard Quandt[1,a)]

AFFILIATIONS

[1]Chair for Inorganic Functional Materials, Institute for Materials Science, Faculty of Engineering, Kiel University, Kiel, Germany
[2]Chair for Multicomponent Materials, Institute for Materials Science, Faculty of Engineering, Kiel University, Kiel, Germany

Note: This paper is part of the Special Topic Collection including papers from the Pacific Rim Symposium on Surfaces, Coatings and Interfaces (PacSurf 2022).

[a)]**Author to whom correspondence should be addressed:** eq@tf.uni-kiel.de

ABSTRACT

Magnesium and magnesium alloys such as magnesium-lithium are of great interest for the application as biodegradable implants. To control the degradation, a tailoring of the corrosion rate is needed. In this study, the effect of a short (5–20 s) dielectric barrier discharge plasma treatment in ambient air on the corrosion rate of magnetron sputtered Mg and MgLi thin films is presented. The treatment with atmospheric plasma of as sputtered samples leads to a decrease of the corrosion rate of 45%–50% in Hanks' balanced salt solution. The higher corrosion resistance is influenced by a change in surface structure and a formation of an $MgCO_3$ containing film.

I. INTRODUCTION

Magnesium and magnesium alloys are widely studied biodegradable materials as candidates for medical applications. Applications of interest reach from biodegradable orthopedic implants and stents up to the possible field of therapeutical treatment.[1–5] To ensure the duration of the integrity of the implant required by the application or the therapeutic activity, the degradation rate needs to be adjustable. Since the corrosion rate of Mg and Mg alloys is often too high for the applications,[6–9] several strategies to reduce the rate have been developed: These include alloying of the bulk material,[10–12] influencing the microstructure,[12–14] surface treatments, and coatings.[15–17] The surface treatments range from deposition of inorganic[18–20] and organic[21–23] deposition coatings over chemical conversion by immersion in solution[24,25] to ion implantation[26,27] or plasma electrolytic oxidation.[28–30]

In this study, the focus of the application is on miniaturized implants fabricated by MEMS (micro-electro-mechanical systems) technology which can serve as, e.g., biodegradable materials for brain implants, either as structural implants, substrates for additional materials or reservoirs for therapeutically active ions. As an example of degradable films that release ions which can act as treatments, MgLi thin films are studied since Li is used in treatments for mood disorders such as bipolar disorder.[31,32] The possibility to include additional ions in a coating to reduce the corrosion rate specifically for the application as reservoirs is limited since they could influence the therapeutic effect if they are released during the degradation. While small Mg structures with a thickness of 10–100 μm can be prepared by thin-film deposition techniques such as sputtering,[33–35] the addition of a thick coating would additionally counteract the effort to reduce the implant size. Thus, a treatment that leads to a thin layer only consisting of the alloy elements itself, possibly also in the form of, e.g., oxides and carbonates, is beneficial. Possible techniques to form those layers include, e.g., chemical treatment in solution to form MgO or $Mg(OH)_2$,[36,37] ion implantation of nitrogen,[38] or plasma treatments.[39–42] Kocijan *et al.* showed that plasma treatment in O_2 and H_2 leads to pin–hole free oxide layers and, thus, lowering the corrosion rate.[39] The formation of an oxide film is also studied for plasma treatment with Ar/O_2 by Tiyyagura[40] while Nakazawa *et al.* examined the implementation of nitrogen and oxide after the treatment of a Mg surface with an atmospheric plasma jet.[41] Additionally, carbon contaminations on

JVST A
Journal of Vacuum Science & Technology A
ARTICLE
pubs.aip.org/avs/jva

the samples are removed by plasma processes.[39] Li *et al.* show that a dielectric barrier discharge (DBD) plasma treatment can reduce or even prevent the corrosion of MgLi alloys with a Li content of 14.2% (m/m) significantly by the formation of Li_2CO_3 and oxide-containing layers.[42] Atmospheric pressure plasmas are highly interesting to influence surface properties in an economic way. In comparison to other techniques, DBDs can easily be scaled up to surface treatments in industrial scales.[43,44] By DBD treatment oxygen groups or compounds can form on the surface by the interaction with elevated oxygen species from the plasma.[45] In the literature, DBDs are also discussed to clean the surface of Mg from remaining contaminations[46] or to lead to the reaction of carbon-containing components to carbonates additional to the formation of an oxide layer.[47] Since for thin films no prior grinding and polishing can be easily performed, the process can, thus, provide advantages additionally to the reduction of the corrosion rate due to the formation of protective layers including oxides and carbonates.

This study aims to evaluate the effect of a DBD plasma treatment to tailor the corrosion resistance of thin films of Mg and MgLi. Since the MgLi samples in this study have a Li content of only 1.6% (m/m), it does not lead to additional Li rich phases which could lead to high Li concentrated protective surface films as seen in previous studies,[42] but might influence the activity and microstructure. Additionally, the nature of thin films with μm thickness does not allow the implementation of thick protective layers. Thus, the effect of the treatment forming layers below 1 μm thickness on the corrosion rate is studied in Hanks' balanced salt solution to simulate the environment in medical applications. Additionally, the layer formed during the treatment is analyzed regarding the structure and chemical composition. By including Mg and MgLi [1.6%(m/m)], the influence of alloying and varying microstructure can provide a detailed understating of the overall process.

II. EXPERIMENT

A. Sample preparation

Magnesium and magnesium-lithium films were prepared by magnetron sputtering (Von Ardenne CS730S), using targets of pure Mg and MgLi [2.5%(m/m) Li] from FHR. As a substrate, 4 in. silicon wafers were cut into 15×15 mm^2 samples and coated with aluminium (Al) and aluminium nitride (AlN) for comparability to freestanding thin films. The sputtering was carried out with a base pressure of $< 5 \times 10^{-7}$ mbar and an Ar pressure of 2.3 -2.6×10^{-3} mbar with a gas flow of 25 SCCM Ar. A final sample thickness of 10–20 μm of Mg and MgLi thin films with a Li mass fraction of 1.6% (m/m) was reached. For one measurement set, all samples were prepared in the same sputtering process, thus, with the same thickness for untreated and treated samples. Additionally, freestanding thin films were prepared with the same sputtering parameters, following the process described by Haffner *et al.*[34] After structuring on the wafer by UV-lithography and etching, a sacrificial AlN layer was added before the final layer of Mg or MgLi was deposited. For the etching of the sacrificial layer, the samples were afterwards immersed in 20 wt. % KOH solution.

B. DBD treatment

The thin-film samples were treated in the gap of a self-built symmetric volume dielectric barrier discharge setup. All treatments were performed in stagnant ambient air. The freestanding thin films were placed on a Si chip (15×15 mm^2) and fixed on the edges to ensure a flatter surface during the treatment. A laboratory power supply (SM7020-D, Delta Elektronika) and a function generator (DDS function generator 4025, Peak Tech) were connected to the high frequency high voltage power supply (Minipuls 4, GBS Elektronik). The resulting sinusoidal voltage signal of the high frequency high voltage power supply with an output of 1:2000 was monitored via an oscilloscope (UTD2025CL, UNIT). The treatment time of the plasma was controlled by an inhibiting signal by a microcontroller board (Arduino nano every) connected to the high frequency high voltage power supply. The DBD setup connected to the power supply can be seen in Fig. 1.

The parameters of the plasma power supply were chosen to allow the formation of filaments all over the sample surface during the complete treatment time, giving a state of saturation (Table I). An overlay of the plasma filaments at all times of the treatment can be seen in Fig. 1(b). The parameters were adjusted if the setup had to be adapted in between measurements of different sample sets due to functioning reasons to ensure a homogeneous surface treatment. For each sample and measurement type, treatments with different treatment times of 5–25 s were carried out with the same parameters to ensure comparability.

C. Sample analysis

The surface of the thin films was imaged and analysed using a Zeiss Ultra 55 Plus scanning electron microscope (SEM) and an Oxford Instruments ULTIM MAX 65 energy-dispersive x-ray spectroscope (EDX). An accelerating voltage of 3 kV for imaging and 10 kV for EDX measurements was used. Additionally, the structure of the thin films was analysed by x-ray diffraction (Smart Lab 9 kW, Rigaku) with a parallel beam and monochromatic Cu Kα radiation on a $\theta/2\,\theta$-scan with a range of 20°–90° with a speed of 5–10°/min and a step size of 0.03°. The chemical composition of the sample surface was characterized by x-ray photoelectron spectroscopy (XPS). For this purpose, an XPS UHV system from Omicron Electron Spectroscopy Ltd. with a 240 W Al anode was used. Survey scans to screen for the elements present at the surface were conducted at a pass energy of 100 eV, a step-size of 0.5 eV, and averaged over three sweeps. High-resolution scans of the characteristic core hole-level spectra used for the chemical analysis were conducted at a pass energy of 30 eV, 15 sweeps, and a step-size of 0.05 eV. For data analysis, the software CASA XPS (Version 2.3.23PR1.0) was utilized and charge correction was done by shifting the C 1 s main peak to 284.8 eV and adjusting all the corresponding spectra accordingly. The corrosion rate was determined by potentiodynamic polarisation measurements in a 155 mmol Hanks' balanced salt solution (H1387, Sigma-Aldrich with added sodium bicarbonate) at a pH of 7.4 ± 0.2 (CO_2 regulation) and a temperature of 37 ± 1 °C. A VersaSTAT 3–300 potentiostat (AMETEKSI) and a three-electrode setup with an Ag/AgCl reference electrode, a Pt mesh counter electrode, and the sample included into a sample holder with an exposed area of 0.916 cm^2

JVST A
Journal of Vacuum Science & Technology A
ARTICLE
pubs.aip.org/avs/jva

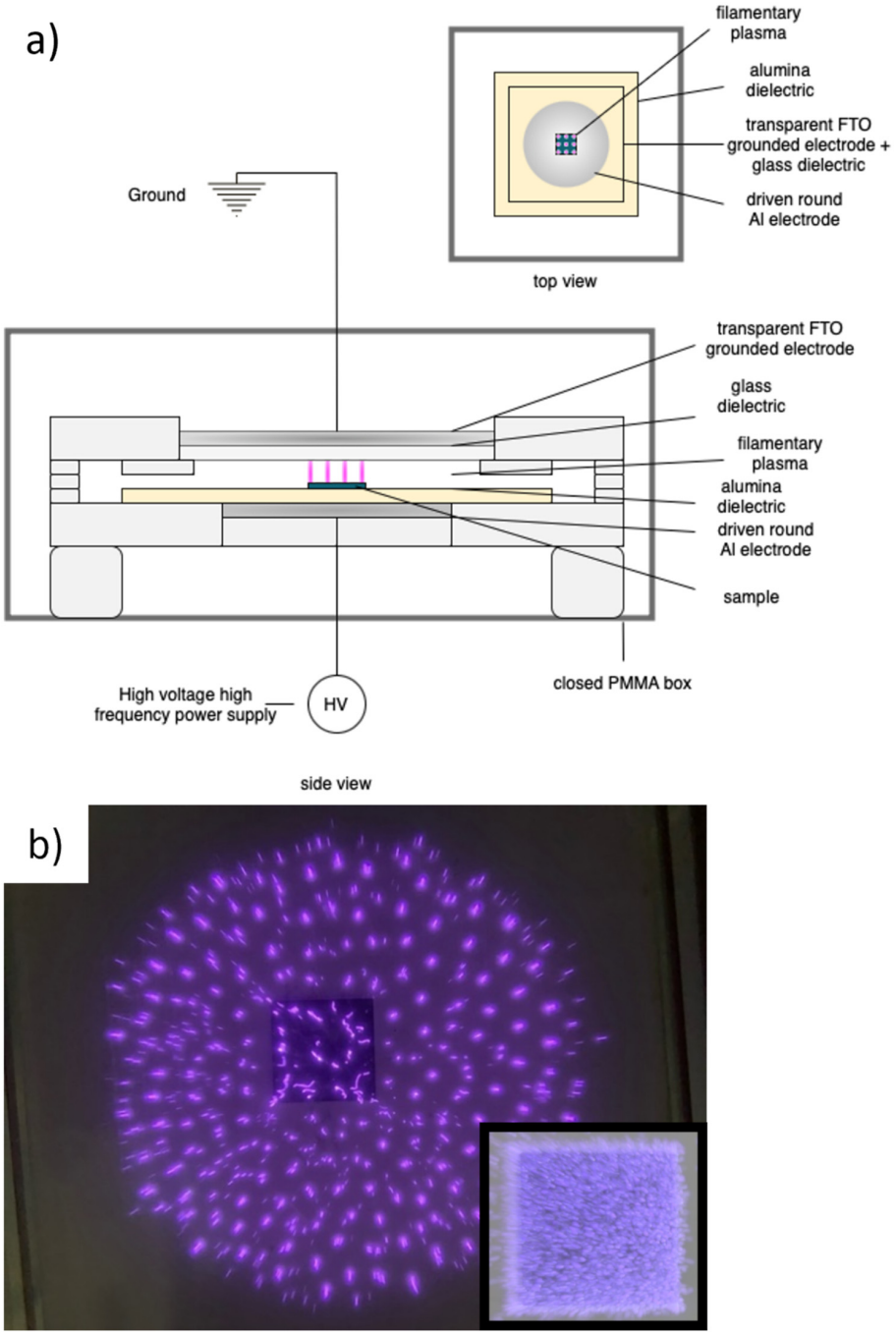

FIG. 1. (a) Scheme of the self-built dielectric barrier discharge system. The electrodes are connected to the high frequency high voltage power supply. The top electrode is a transparent FTO-coating on glass (Sigma Aldrich, 100 × 100 × 2.2 mm^3, 13 Ω/sq) acting as the top dielectric, making the observation of the plasma treatment from the top possible. The bottom electrode is made from aluminum with the bottom dielectric being made from 6 mm thick Al_2O_3. (b) Photo of the DBD treatment of an Mg thin film seen through the top transparent electrode. For the inset, photos (video frames from a video with 30 fps) over a treatment time of 15 s were combined to show all filaments during a treatment, ensuring area saturation.

were used. After 5 min of measuring the open circuit potential (E_{OCV}), a linear voltage sweep from −0.3 V vs E_{OCV} to +0.3 V vs E_{OCV} was performed. Further information can be found in Ref. 48. Additionally, the same measurement was carried out after 1h of immersion time.

III. RESULTS AND DISCUSSION

A. Thin-film characterization

Representative cross sections and surface images of the sputtered thin films of Mg and MgLi are shown in Figs. 2(a)–2(d).

JVST A
Journal of Vacuum Science & Technology A
ARTICLE
pubs.aip.org/avs/jva

TABLE I. The parameters of DBD treatment. Listed are the distance d between both electrodes, the frequency f, and the discharge voltage $U_{discharge}$.

	d (mm)	f (kHz @5Vpp)	$U_{discharge}$ (kVpp)
Mg, MgLi [Fig. 3(b)]	3.9	20	24
MgLi [Fig. 3(c)]	1.9	17	25.3
MgLi [Fig. 3(c), 1 h immersion]	1.9	19	22.8

While for both materials a columnar growth is visible, the surface exhibits different structures for both sample types with a more structured surface for Mg and larger grainlike areas for MgLi. EDX analysis of the surface of the thin film identify an oxide and carbonate signal for both sample types with no significant difference between Mg and MgLi [2%–3%(m/m) C and 0.5%–1%(m/m) O]. No further quantification of oxide or carbonate components is carried out due to the possibility of the influence of contaminations on the exact intensity. In Fig. 2(e), XRD diffractograms show signals of the thin film itself and the substrate. Mg and MgLi have a hexagonal closed packed (hcp) structure with a strong preferred orientation for pure Mg.

Samples of Mg and MgLi on the substrate and freestanding films of MgLi were treated with an atmospheric pressure dielectric barrier discharge plasma in air with a saturation of filamentary discharges, as seen in Fig. 1(b).

B. Corrosion measurements

Exemplary potentiodynamic polarization curves for an untreated and 15 s treated sample after 5 min of immersion are shown for Mg and MgLi in Fig. 3(a). The corrosion current densities and corrosion rates can be determined via Tafel extrapolation.[48,49] The cathodic branch was used for the estimation of the corrosion rate for the following studies due to the larger linear area. The current density of the anodic branch is influenced by additional hydrogen evolution, film formation, and passivation regions,[50–52] thus, a corrosion rate determined on the anodic branch may differ from the rate determined from the cathodic branch. MgLi samples were treated for 5, 10, 15, and 20 s. To exclude the effect of Li on the influence of the plasma treatment, Mg samples were treated for 5 and 15 s for comparison. The corrosion rates for the measurements are shown in Fig. 3(b). A significant decrease in the corrosion rate for both material type is apparent, lowering the corrosion rate (CR) during a treatment of 15 s from $CR_{untreated} = 2.19$ mm/yr to $CR_{treated} = 0.45$ mm/yr for MgLi and from $CR_{untreated} = 1.69$ mm/yr to $CR_{treated} = 0.38$ mm/yr for Mg. Since the effect for both sample types is similar and Li or the different surface structure does not seem to influence the effect of the treatment significantly, further studies were only carried out with MgLi samples.

MgLi thin films with a lower corrosion rate were measured with the corresponding corrosion rates given in Fig. 3(c). The main decrease in corrosion rate already occurs after a treatment time of 5 s with a reduction of the corrosion rate of about 46% (0.23 ± 0.03 mm/yr to 0.13 ± 0.01 mm/yr). Since the corrosion resistance differs only slightly for longer treatments, the times were set to 5 and 15 s. Since the potentiodynamic polarization measurements show the degradation of samples only for the short term,

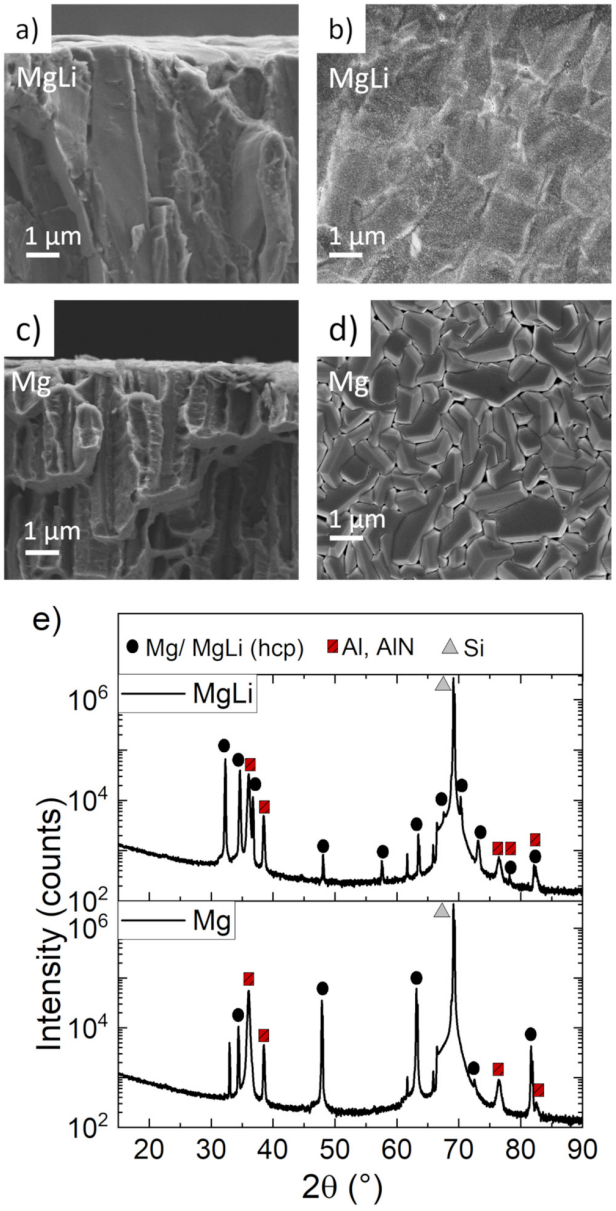

FIG. 2. Thin films as sputtered on the substrate (Si wafer with the added Al + AlN layer) (a) and (b) SEM cross section and image of the surface of MgLi, (c) and (d) SEM cross section and image of the surface of Mg, (e) XRD diffractogram, signals of Mg, Al, AlN, and Si are marked. Peaks without symbol are kβ, WLa, and edge effect signals of the Si substrate.

JVST A
Journal of Vacuum Science & Technology A
ARTICLE
pubs.aip.org/avs/jva

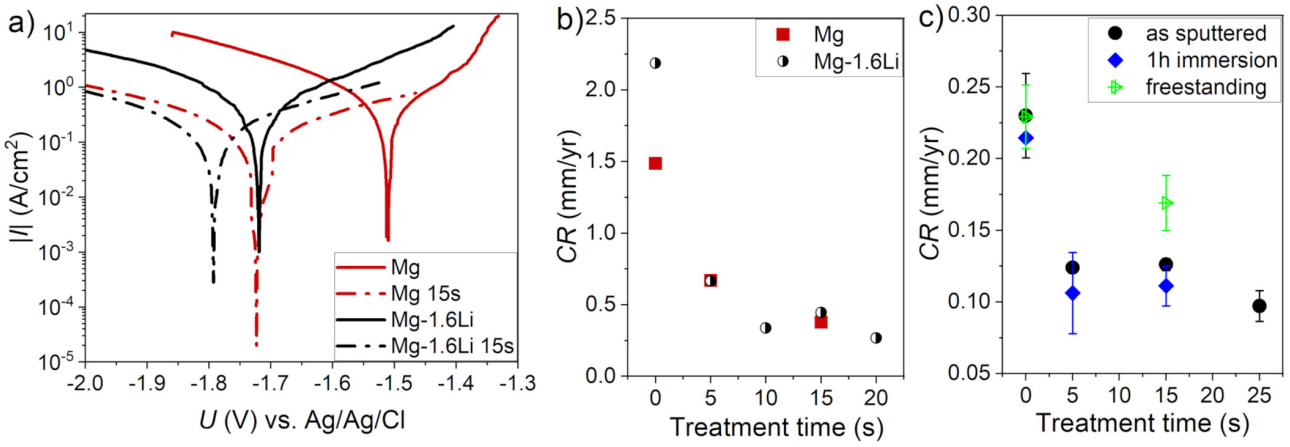

FIG. 3. Potentiodynamic polarization measurements in Hanks' balanced salt solution (p*H* = 7.4 ± 0.2 and T = 37 ± 1 °C). (a) Exemplary Tafel plots for Mg and Mg-1.6Li as sputtered on the substrate and after 15 s DBD plasma treatment. (b) Corrosion rate (*CR*) of as-sputtered Mg and Mg-1.6Li on the substrate. (c) Corrosion rates (*CR*) for Mg-1.6Li thin films as sputtered, after 1 h immersion and freestanding thin films (without preimmersion).

additional measurements are necessary to confirm the improvement of corrosion resistance over longer time periods. Weight-loss measurements over longer terms are difficult due to the low sample weight of thin films and the cleaning resulting in the removal of corrosion products and possible products formed during the treatment, thus, not allowing the final identification of the corroded mass. Therefore, additional potentiodynamic polarization measurements were carried out after 1h of immersion to allow the prior formation of corrosion products on the surface of the film which can protect the film from further corrosion.[53,54]

As shown in Fig. 3(c), the corrosion rate still decreases after the DBD treatment significantly to approximately half of the corrosion rate. Thus, the treatment not only leads to a passivation decreasing the first corrosion before a protective corrosion layer is formed but also leads to a stronger protective layer throughout the degradation.

No significant change in the corrosion potential E_{corr} can be identified for MgLi thin films after the treatment for 15 s in comparison to the untreated samples. While an E_{corr} of -1.85 ± 0.08 V is measured for the untreated samples directly after immersion, E_{corr} for samples with a 15 s treatment measured is -1.85 ± 0.01 V, thus, the potential varies for untreated samples, while it is more stable for the treated samples. After 1h of immersion, the potential is slightly increased to -1.78 ± 0.02 V for untreated samples and -1.79 ± 0.03 V for samples after 15 s of treatment. The increase after longer immersion time can be assigned to the lower activity of the material, possibly due to the depletion of Li on the surface[55] and the formation of other products during corrosion.[53,54] Thus, the DBD treatment itself does not influence the potential of the material.

For possible applications of Mg or Mg-based alloys as implants for small-size applications and not coatings on other materials, the thin films need to have a thickness in the μm range without an additional substrate. The process to produce the thin films used in this study is described by Haffner *et al.*[34] Since the sacrificial layer of Al and AlN is dissolved in KOH, the films are also exposed to KOH for the duration of the lift-off, resulting in a changed surface. A treatment with KOH is reported to lower the corrosion rate even without additional treatment if the sample is anodized due to the formation of more stable MgO and Mg $(OH)_2$;[36] however, this effect is not observed here, possibly due to the insufficient thickness and density of the layer formed during the simple immersion. The effect of the plasma treatment is lower on the freestanding samples; however, a decrease in the corrosion rate is still visible [Fig. 3(c)]. Additional to the change of surface structure, the samples on substrate also had a flatter surface than freestanding thin films which were only attached to Si chips, thus, ensuring a more homogeneous treatment. Thus, an optimization of the treatment and sample fixation for freestanding thin films could improve the degradation rate decrease further.

The corrosion studies prove that only very short DBD plasma treatments of Mg and MgLi are required to significantly influence

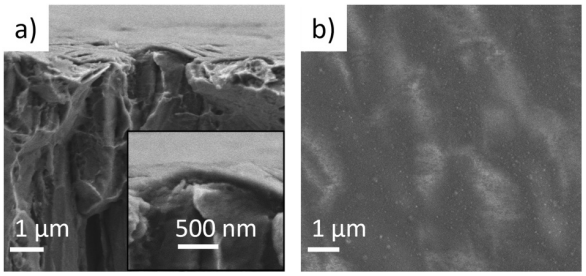

FIG. 4. SEM image of MgLi thin films, (a) cross section (inset shows the surface film with higher magnification) and (b) surface image of the surface film formed after 15 s of DBD treatment.

JVST A
Journal of Vacuum Science & Technology A
ARTICLE
pubs.aip.org/avs/jva

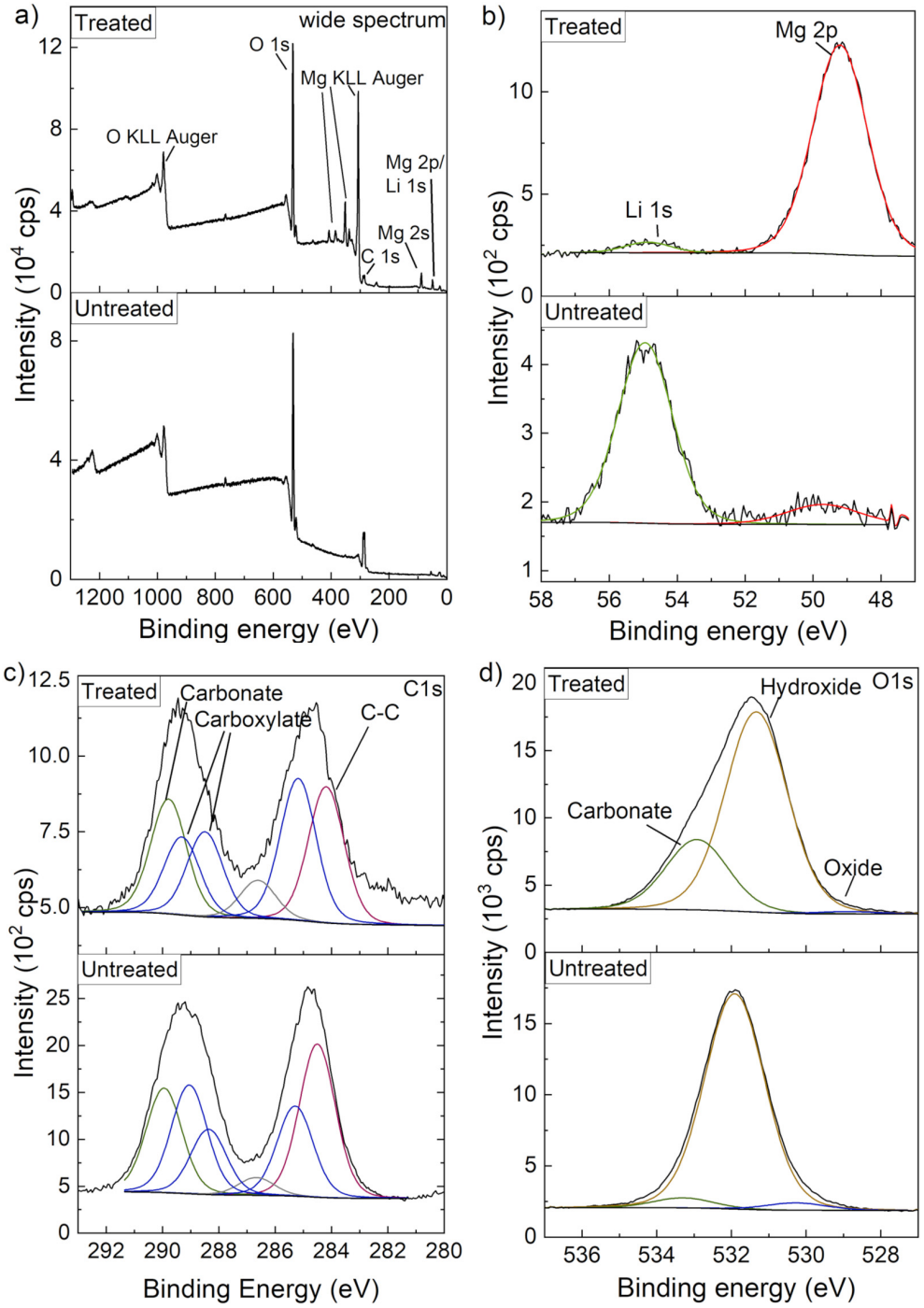

FIG. 5. XPS spectra of untreated and treated MgLi thin films (a) full spectrum, (b) Mg 2p and Li 1 s, (c) C 1 s (positions of carbonates, C–C and carboxylates are marked, see the supplementary material at for spectra with a full description of C compounds, fitted according to Fotea *et al.* (Ref. 62, Fig. S1) and (d) O 1 s regions. See the supplementary material Tables SII and SIII for the corresponding peak positions and full-width-at-half-maximum.

JVST A
Journal of Vacuum Science & Technology A
ARTICLE
pubs.aip.org/avs/jva

the corrosion of the films. Since the treatment mainly influences the surface of the films, a passivation and formation of a protective film is expected to be the reason for the change in the corrosion rate and is, therefore, analyzed further.

C. Surface films

The degradation of Mg-based alloys such as MgLi is highly influenced by surface films formed before or during the corrosion. Those films hinder further ion release or reaction on the surface of the samples. For Mg and MgLi, layers formed in air and during corrosion including many components such as MgO, $Mg(OH)_2$, $MgCO_3$, LiO_2, LiOH, or Li_2CO_3 are discussed to influence the corrosion rate.[54–58]

Surface images and cross sections of 15 s plasma treated samples show the formation of a thin surface film during the treatment as shown in Fig. 4. A more homogeneous surface with reduced roughness in comparison to untreated samples is visible after the DBD treatment. The layer formed during the treatment which can be identified by a structural difference from the main sample in Fig. 4(a) has a thickness in the range of 50−100 nm. Since the formed surface film leads to a flatter surface, it reduces the surface area for corrosion and prevents the start of corrosion at preformed pits such as, e.g., the edges of the surface structures shown in Figs. 2(b) and 2(d). A homogeneous corrosion with less pitting and a smaller active surface can significantly influence the corrosion rate.[59–61] The film can only form by reactions of the elements of the film (Mg and Li) with elements available in air since no additional gases are added. EDX studies show an increase in oxygen and carbon components measured on the surface in comparison to untreated samples, especially on the surface [approximately 3%−4%(m/m) C and 5−5.5%(m/m) O], thus, the film could consist of components such carbonates, oxides, or hydroxides. However, since the film has only a thickness in the nm range, EDX analysis cannot give further insights. Therefore, XPS analysis was carried out on a treated and untreated MgLi sample to identify the components formed during the treatment. The wide spectra and Mg 2p, Li 1 s and C 1 s, O 1 s spectra are shown in Fig. 5. See the supplementary material Table SI for the atomic compositions.

While for the untreated sample, a Li signal but only a small Mg is shown in Fig. 5(b), for the treated sample, a significant increase of the Mg 2p signal can be found. Additionally, the carbon spectrum in Fig. 5(c) shows an overall decrease in carbon-containing components. The lower overall peak width and proportionally higher decrease in carboxylate signal in comparison to carbonates could possibly be the result of the removal or a reaction to carbonate in the layer. The formation of carbonates is also found in the O 1 s spectrum in Fig. 5(d). The lower carbon signal and formation of carbonates could be a result of a cleaning effect, reaction of other compounds to carbonates and carbonate formation during the treatment.[42,46,47]

Different components were discussed in the literature to lead to a protective layer during corrosion of Mg or MgLi.[54–58] For MgLi, Li_2CO_3 formed during DBD treatment or during the corrosion was discussed to influence the corrosion rate for Li alloys with high Li fraction [14.2% (m/m)].[42] Those layers could also be formed for material with low Li fraction.[63] Li_2CO_3 can be formed in air, leading to a higher Li fraction on the sample surface and a Mg deficiency in the surface layer in comparison to the bulk material on samples without treatment.[55] This could lead to the low Mg signal measured by XPS on the untreated sample. Apparently, after the treatment, the surface layer formed does not consist of Li_2CO_3 since the Mg signal is stronger and a decrease in Li is found by XPS. Thus, Li_2CO_3 is not the main important component for the increased corrosion resistance for the MgLi thin films studied. This is also confirmed by the corrosion rate decrease for samples of Mg without Li addition.

Since the surface layer is formed in air, possible elements included could be oxygen, carbon, or nitrogen. For the corrosion of Mg, the formation of MgO and further reaction to $Mg(OH)_2$ occurs. While the layer of MgO is dense but due to a Poisson–Bedworth ratio <1 unstable, the further reaction to $Mg(OH)_2$ when in contact with water leads to a porous layer[64] which can only slightly hinder corrosion. The stability of MgO could be increased by Li doping;[56] however, since there is no or only 1.6%(m/m) Li included, no stability can be assumed. The wide spectrum does not show a significant nitrogen signal and, thus, no components including N can be directly assigned as part of the protective film. The increase of the carbonate signal and the presence of more Mg on the surface of treated samples in comparison to untreated samples could hint to a formation of $MgCO_3$. $MgCO_3$ is stable and can reduce the corrosion rate of Mg[57,65–67] if the layer is dense.

The lower corrosion rate is, thus, a result of a change in surface structure and a formation of a protective layer, possibly including $MgCO_3$. However, as known for the layer formation on Mg and MgLi in air and in corrosion, the protective layers formed are often a system of different layers including different components[55,57,58] and cannot be directly identified as one component only. The combination of a decrease in roughness and a dense layer of stable carbonates and oxides leads to a slower degradation not only for the beginning of the immersion but also leads to an increased corrosion resistance after longer immersion time.

IV. SUMMARY AND CONCLUSIONS

This study presents a fast and simple method to reduce the corrosion rate of Mg-based thin films using dielectric barrier discharge plasma treatment. hcp Mg and MgLi thin films were prepared by magnetron sputtering, leading to different surface roughness and microstructures. After 15 s of DBD plasma treatment, the corrosion rate of all as-sputtered samples was reduced by around 45%–50%, even when the sample was immersed for an hour before the potentiodynamic polarization measurement. Thus, a stable protective layer is formed during the treatment which is also denser and more stable than the passivating films formed during the corrosion. Analysis of the surface by SEM/EDX and XPS shows the removal of loose contaminations and a layer formed on the surface which can influence the corrosion rate by leading to a smoother surface and components including magnesium carbonate preventing fast corrosion. The treatment was also tested on free-standing thin films to confirm the effect of the treatment on samples for the possible application of ion release as therapeutical treatment.

JVST A
Journal of Vacuum Science & Technology A
ARTICLE
pubs.aip.org/avs/jva

The atmospheric DBD plasma treatment presents a cheap and easily industrially scalable way to prevent the burst release of Mg thin films. The effect reaching a plateau after 5 s also makes the method reproducible, as the treatment effect saturates quickly.

ACKNOWLEDGMENTS

This work was supported by the DFG in the framework of the research training group 2154—Materials for Brain (Project No. 270394294).

AUTHOR DECLARATIONS

Conflict of Interest

The authors have no conflicts to disclose.

Author Contributions

Lisa Hanke: Conceptualization (equal); Formal analysis (equal); Investigation (equal); Writing – original draft (equal); Writing – review & editing (equal). **Torge Hartig:** Conceptualization (equal); Investigation (supporting); Methodology (lead); Writing – original draft (supporting); Writing – review & editing (supporting). **Felix Weisheit:** Formal analysis (supporting); Investigation (equal); Writing – review & editing (supporting). **Tim Tjardts:** Formal analysis (supporting); Investigation (supporting). **Tim Pogoda:** Investigation (supporting); Methodology (supporting). **Franz Faupel:** Funding acquisition (equal); Supervision (equal). **Eckhard Quandt:** Funding acquisition (equal); Supervision (equal); Writing – review & editing (supporting).

DATA AVAILABILITY

The data that support the findings of this study are available from the corresponding author upon reasonable request.

REFERENCES

[1]S. Zaatreh *et al.*, Biofouling **33**, 294 (2017).
[2]D. Zhao, F. Witte, F. Lu, J. Wang, J. Li, and L. Qin, Biomaterials **112**, 287 (2017).
[3]M. Moravej and D. Mantovani, Int. J. Mol. Sci. **12**, 4250 (2011).
[4]M. Haude *et al.*, EuroIntervention **13**, 432 (2017).
[5]C. M. Campos *et al.*, Int. J. Mol. Sci. **14**, 24492 (2013).
[6]A. Atrens, G.-L. Song, M. Liu, Z. Shi, F. Cao, and M. S. Dargusch, Adv. Eng. Mater. **17**, 400 (2015).
[7]G. Song and A. Atrens, Adv. Eng. Mater. **5**, 837 (2003).
[8]X. Li, X. Liu, S. Wu, K. W. K. Yeung, Y. Zheng, and P. K. Chu, Acta Biomater. **45**, 2 (2016).
[9]A. Atrens, M. Liu, and N. I. Zainal Abidin, Mater. Sci. Eng. B **176**, 1609 (2011).
[10]N. T. Kirkland, J. Lespagnol, N. Birbilis, and M. P. Staiger, Corros. Sci. **52**, 287 (2010).
[11]Y. Ding, C. Wen, P. Hodgson, and Y. Li, J. Mater. Chem. B **2**, 1912 (2014).
[12]K. Chen, J. Dai, and X. Zhang, Corros. Rev. **33**, 101 (2015).
[13]B. J. Wang, D. K. Xu, X. Cai, Y. X. Qiao, and L. Y. Sheng, J. Magnes. Alloys **9**, 560 (2021).
[14]E. Gerashi, R. Alizadeh, and T. G. Langdon, J. Magnes. Alloys **10**, 313 (2022).
[15]Y. H Sun, R. C. Wang, C. Q. Peng, Y. Feng, and M. Yang, Trans. Nonferrous Met. Soc. China **27**, 1455 (2017).
[16]Z.-Z. Yin, W.-C. Qi, R.-C. Zeng, X.-B. Chen, C.-D. Gu, S.-K. Guan, and Y.-F. Zheng, J. Magnes. Alloys **8**, 42 (2020).
[17]M. S. Uddin, C. Hall, and P. Murphy, Sci. Technol. Adv. Mater. **16**, 053501 (2015).
[18]J. Choi, S. Nakao, J. Kim, M. Ikeyama, and T. Kato, Diam. Relat. Mater. **16**, 1361 (2007).
[19]H. Hoche, C. Blawert, E. Broszeit, and C. Berger, Surf. Coat. Technol. **193**, 223 (2005).
[20]H. Hoche, H. Scheerer, D. Probst, E. Broszeit, and C. Berger, Surf. Coat. Technol. **174–175**, 1018 (2003).
[21]K. Bai, Y. Zhang, Z. Fu, C. Zhang, X. Cui, E. Meng, S. Guan, and J. Hu, Mater. Lett. **73**, 59 (2012).
[22]H. M. Wong, K. W. K. Yeung, K. O. Lam, V. Tam, P. K. Chu, K. D. K. Luk, and K. M. C. Cheung, Biomaterials **31**, 2084 (2010).
[23]J. Park *et al.*, Sci. Rep. **8**, 17743 (2018).
[24]L. Jianrui, G. Yina, and H. Weidong, Surf. Coat. Technol. **201**, 1536 (2006).
[25]X. B. Chen, N. Birbilis, and T. B. Abbott, Corrosion **67**, 035005 (2011).
[26]Y. Zhao, M. I. Jamesh, W. K. Li, G. Wu, C. Wang, Y. Zheng, K. W. K. Yeung, and P. K. Chu, Acta Biomater. **10**, 544 (2014).
[27]M.-I. Jamesh, Lubricants **10**, 255 (2022).
[28]F. Simchen, M. Sieber, A. Kopp, and T. Lampke, Coatings **10**, 628 (2020).
[29]R. O. Hussein, X. Nie, and D. O. Northwood, Corros. Mater. **38**, 54 (2013).
[30]Z. Li, Q. Ren, X. Wang, Q. Kuang, D. Ji, R. Yuan, and X. Jing, Corros. Sci. **157**, 295 (2019).
[31]C. Volkmann, T. Bschor, and S. Köhler, Front. Psychiatry **11**, 377 (2020).
[32]A. Can, T. G. Schulze, and T. D. Gould, Pharmacol. Biochem. Behav. **123**, 3 (2014).
[33]K. Schlüter, Z. Shi, C. Zamponi, F. Cao, E. Quandt, and A. Atrens, Corros. Sci. **78**, 43 (2014).
[34]D. Haffner, C. Zamponi, R. L. de Miranda, and E. Quandt, BioNanoMaterials **16**, 19 (2015).
[35]L. K. Jessen, C. Zamponi, R. Willumeit-Römer, and E. Quandt, Acta Biomater. **98**, 81 (2019).
[36]J. Moreno, J. L. Merlo, A. C. Renno, J. Canizo, F. J. Buchelly, J. I. Pastore, M. R. Katunar, and S. Cere, Electrochim. Acta **437**, 141463 (2023).
[37]A. Yamamoto and H. Tsubakino, Mater. Trans. **44**, 511 (2003).
[38]X. B. Tian, C. B. Wei, S. Q. Yang, R. K. Y. Fu, and P. K. Chu, Surf. Coat. Technol. **198**, 454 (2005).
[39]A. Kocijan, J. Kovač, I. Junkar, M. Resnik, V. Kononenko, and M. Conradi, Materials **15**, 7405 (2022).
[40]H. R. Tiyyagura, H. Puliyalil, G. Filipič, K. C. Kumar, Y. B. Pottathara, R. Rudolf, R. Fuchs-Godec, M. K. Mohan, and U. Cvelbar, Surf. Coat. Technol. **385**, 125434 (2020).
[41]K. Nakazawa, T. Ohashi, S. Saiki, and S. Kikuchi, J. Magnes. Alloys **10**, 1878 (2022).
[42]Y. Li, Z. Kang, X. Zhang, J. Pan, Y. Ren, and G. Zhou, Surf. Coat. Technol. **439**, 128418 (2022).
[43]U. Kogelschatz, Plasma Chem. Plasma **23**, 1 (2003).
[44]R. Brandenburg, Plasma Sources Sci. Technol. **26**, 053001 (2017).
[45]O. Polonskyi, T. Hartig, J. R. Uzarski, and M. J. Gordon, J. Vac. Sci. Technol. A **39**, 063001 (2021).
[46]S. Knust, A. Kuhlmann, T. de los Arcos, and G. Grundmeier, RSC Adv. **9**, 35077 (2019).
[47]L. Cheng, R. Ghobeira, P. Cools, B. Luthringer, M. Asadian, N. De Geyter, Z. Liu, K. Yan, and R. Morent, Surf. Coat. Technol. **410**, 126934 (2021).
[48]T. Jurgeleit, E. Quandt, and C. Zamponi, Adv. Mater. Sci. Eng. **2015**, 294686.
[49]M. Stern and A. L. Geaby, J. Electrochem. Soc. **104**, 56 (1957).
[50]L. Rossrucker, K. J. J. Mayrhofer, G. S. Frankel, and N. Birbilis, J. Electrochem. Soc. **161**, C115 (2014).
[51]A. Atrens, X. Chen, and Z. Shi, Corros. Mater. Degrad. **3**, 566 (2022).
[52]Z. Shi, M. Liu, and A. Atrens, Corros. Sci. **52**, 579 (2010).
[53]B. J. Wang, D. K. Xu, J. H. Dong, and W. Ke, J. Mater. Sci. Technol. **34**, 1756 (2018).
[54]B.-J. Wang, J.-Y. Luan, D.-K. Xu, J. Sun, C.-Q. Li, and E.-H. Han, Acta Metall. Sin. Engl. Lett. **32**, 1 (2019).

JVST A
Journal of Vacuum Science & Technology A
ARTICLE
pubs.aip.org/avs/jva

[55]W. Xu, N. Birbilis, G. Sha, Y. Wang, J. E. Daniels, Y. Xiao, and M. Ferry, Nat. Mater. **14**, 1229 (2015).
[56]Y. M. Yan *et al.*, Corros. Sci. **164**, 108342 (2020).
[57]R.-C. Zeng, L. Sun, Y.-F. Zheng, H.-Z. Cui, and E.-H. Han, Corros. Sci. **79**, 69 (2014).
[58]Y. Yan, Y. Qiu, O. Gharbi, N. Birbilis, and P. N. H. Nakashima, Appl. Surf. Sci. **494**, 1066 (2019).
[59]H. Yang, L. Wu, B. Jiang, W. Liu, J. Song, G. Huang, D. Zhang, and F. Pan, J. Mater. Sci. Technol. **62**, 128 (2021).
[60]R. Walter and M. B. Kannan, Mater. Des. **32**, 2350 (2011).
[61]Z. Yao, Q. Xia, H. Wei, D. Li, Q. Sun, and Z. Jiang, RSC Adv. **5**, 68806 (2015).
[62]C. Fotea, J. Callaway, and M. R. Alexander, Surf. Interface Anal. **38**, 1363 (2006).
[63]C. Q. Li, D. K. Xu, X.-B. Chen, B. J. Wang, R. Z. Wu, E. H. Han, and N. Birbilis, Electrochim. Acta **260**, 55 (2018).
[64]M. Taheri, M. Danaie, and J. R. Kish, J. Electrochem. Soc. **161**, C89 (2014).
[65]Y. Wang *et al.*, Nat. Commun. **9**, 4058 (2018).
[66]M. S. Palanisamy, R. Kulandaivelu, and S. N. T. S. Nellaiappan, New J. Chem. **44**, 4772 (2020).
[67]R. Zeng, W. Qi, F. Zhang, H. Cui, and Y. Zheng, Prog. Nat. Sci. Mater. Int. **24**, 492 (2014).
[68]See the supplementary material for results of the XPS analysis regarding the atomic concentrations, C spectra with all fitted compounds, and binding energy positions for untreated and treated films.

3.6 Addition of an alloying element - MgAgLi

Additional to a change in the surface, the bulk material can be changed by alloying with additional elements. As discussed in section 2.1.2, an alloying element which does not have any negative medical effects has to be chosen. Since MgAg thin films have been studied before [27, 28] to improve both the corrosion rate and mechanical properties, Ag was added to the Mg-1.6Li alloy with 6 wt% of Ag. Mg-6Ag showed the lowest corrosion rate and a high tensile strength and elongation in comparison to other MgAg thin films according to Jessen et al. [27, 28].

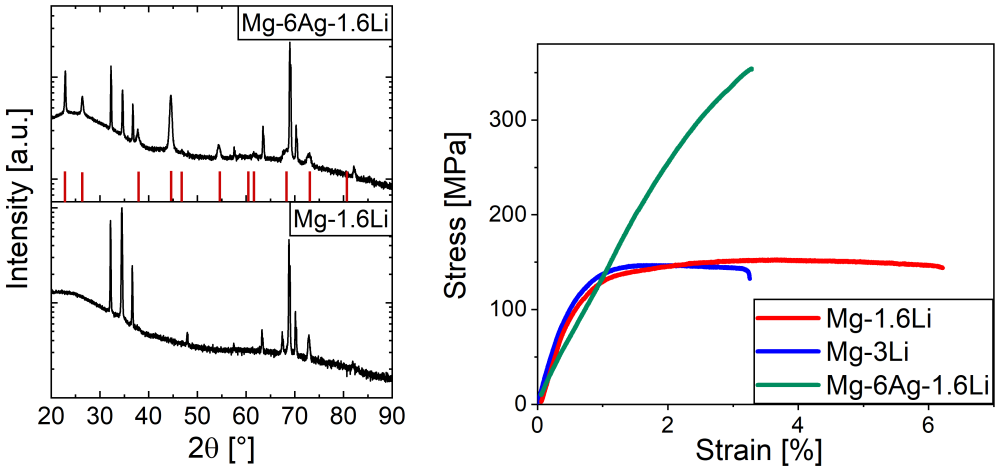

(a) (b)

Figure 3.10: Comparison of Mg-1.6Li and Mg-6Ag-1.6Li. a) Diffractograms of thin films. In red, the positions of a MgAgLi phase (cubic, based on [208]) are marked. b) Exemplary stress-strain curves of Mg-1.6Li, Mg-3Li and Mg-6Ag-1.6Li.

In figure 3.10(a), the diffractogram of Mg-1.6Li and Mg-6Ag-1.6Li are shown. In comparison to Mg-6Ag with a strongly preferred [0001] direction of growth, a more random orientation is found with only a slight preference in Mg-1.6Li. An additional phase of MgAgLi occurs (comparison to Ag-Li_2-Mg [208]). Even though a second phase is formed, the corrosion rate of Mg-6Ag-1.6Li is similar to Mg-1.6Li with 0.15±0.03 mm/yr in comparison to 0.13±0.03 mm/yr measured by potentiodynamic polarisation in Hank's balanced salt solution (pH 7.4, T=37±1 °C). The corrosion potential E_{OCV} is increased due to the Ag to -1.29±0.05 V in comparison to -1.73±0.02 V. The mechanical properties are, however, affected much stronger. The results from tensile testing are shown in figure 3.10(b) in comparison to Mg-1.6Li and Mg-3Li for exemplary samples. The maximum elongation is reduced in comparison to Mg-1.6Li but similar to Mg-3Li (3.2±1.0 %) while the yield strength and tensile strength are strongly increased to 335±20 MPa and 350±20 MPa due to the hardening effects of the Ag and additional phases formed [28].
Thus, the results show that the mechanical properties of MgLi can be further adjusted without increasing the corrosion rate by an exemplary alloying element.

4 Conclusion and Outlook

This thesis is based on the idea of developing MgLi thin-film implants that could be placed in the brain as drug reservoirs for the treatment of neurological disorders. Therefore, the properties of magnetron-sputtered MgLi thin films with varying Li content were investigated. Since the corrosion rate influences the released ion concentration and, thus, the possible treatment, a special focus was placed on understanding the corrosion process.

Mg-alloy thin films with Li content of 1.6 - 9.5 wt% were fabricated, thus resulting in films with a pure hcp phase and a mixed phase of hcp and bcc MgLi. Due to the high reactivity of Li, the formation of oxides and carbonates, especially for high Li content, cannot be prevented. The formation of Li_2CO_3 was also found for hcp MgLi alloys. It, however, dissolves when the film is in contact with solution. To gain a full picture of the corrosion processes, several techniques were combined, including in-situ and long-term studies, analysis of ion release, weight loss and electrochemical measurements. A change in Li fraction and orientation influences the corrosion for hcp thin films and a higher Li content and more random orientation result in a higher corrosion rate. During the corrosion process, a dissolution of the Li-containing surface layer is followed by a preferred Mg release in short term measurements. The formation of Mg-containing corrosion products and the higher reactivity of Li lead to a preferred Li release over longer immersion times. For films in the mixed phase, the microgalvanic coupling and formation of protective layers both play an important role. The highest corrosion rate was observed for Mg-5.5Li while for Mg-9.5Li, a rate similar to hcp samples was measured due to the reduction of the corrosion rate by passivation.

For the application as a reservoir for treatments, the release of ions not only needs to be understood but also tailored. To change the corrosion rate and, thus, the ion concentration, the microstructure or surface film can be influenced. The reduction in void formation by changing the sputtering parameters for Mg-3Li reduced the corrosion rate by nearly 50 %. Applying a treatment by atmospheric DBD plasma led to a reduction of the corrosion rate of Mg and Mg-1.6Li by over 45 %. While the addition of Ag did not change the corrosion rate, the alloying with further elements can also adjust other implant parameters such as the mechanical properties.

The surroundings, including the testing solution or organic components, also play a central role. This thesis was part of the research training group "Materials for Brain" and was developed in close collaboration with the project of Krathika Bhat which focused on analysing the effect of MgLi and the degradation of the thin films on cells. Tests with glial cells and brain slice models proved the biocompatibility of the thin films and an effect of the ion release on gene expressions, which might be of interest for the effect on neurological disorders [209]. Additionally, the thin films of Mg and MgLi were studied with Schwannoma cells, showing better peripheral nerve regeneration under the influence of Mg released from the thin films[210]. Further analysis of the interaction by studying

the corrosion products and layers formed on the samples during immersion with cell attachment and a detailed study of the released ions would be necessary to gain a better understanding of the corrosion process under more complex conditions.

While this thesis gives an essential insight into the general mechanisms and influences on the degradation of magnetron-sputtered MgLi thin films, it only marks a first step to the final application. In future work, the analysis of the degradation in more complex systems *in vitro* and *in vivo* is necessary to prove the applicability of MgLi thin films as implants for the treatment of neurological disorders.

Appendix

A.1 Supplement Structural characterisation and degradation of Mg-Li thin films for biodegradable implants

Structural characterisation and degradation of Mg-Li thin films for biodegradable implants - Supplementary information

Lisa Hanke[1], Lea K. Jessen[1], Felix Weisheit[1], Krathika Bhat[2], Ulrike Westernströer[3], Dieter Garbe-Schönberg[3], Regine Willumeit-Römer[2], Eckhard Quandt[1]*

[1]Inorganic Functional Materials, Institute for Materials Science, Faculty of Engineering, Kiel University, Kiel, Germany

[2]Institute of Metallic Biomaterials, Helmholtz Centre hereon, Geesthacht, Germany

[3]Marine Climate Research, Institute of Geosciences, Faculty of Mathematics and Natural Sciences, Kiel University, Kiel, Germany

Mg-Li alloy	Li (%(m/m))			Fe (%(m/m))
	Target	Film, ICP-MS	Film, AAS	Film, ICP-MS
Mg-1.6Li	2.5	1.60±0.06	1.55±0.03	0.0029±0.0008
Mg-3Li	5	3.07±0.12	3.13±0.08	0.0027±0.0003
Mg-5.5Li	9	5.15±0.69	6.12±0.32	0.0028±0.0004
Mg-9.5Li	14	9.31±0.84	9.88±0.07	0.0033±0.0006

Table 1 Mass fractions of Li in targets (nominal) and prepared freestanding thin films analysed by ICP-MS and AAS. Additionally, the Fe contamination measured by ICP-MS is given. The measurement uncertainties given are statistical deviations from minimum 3 samples.

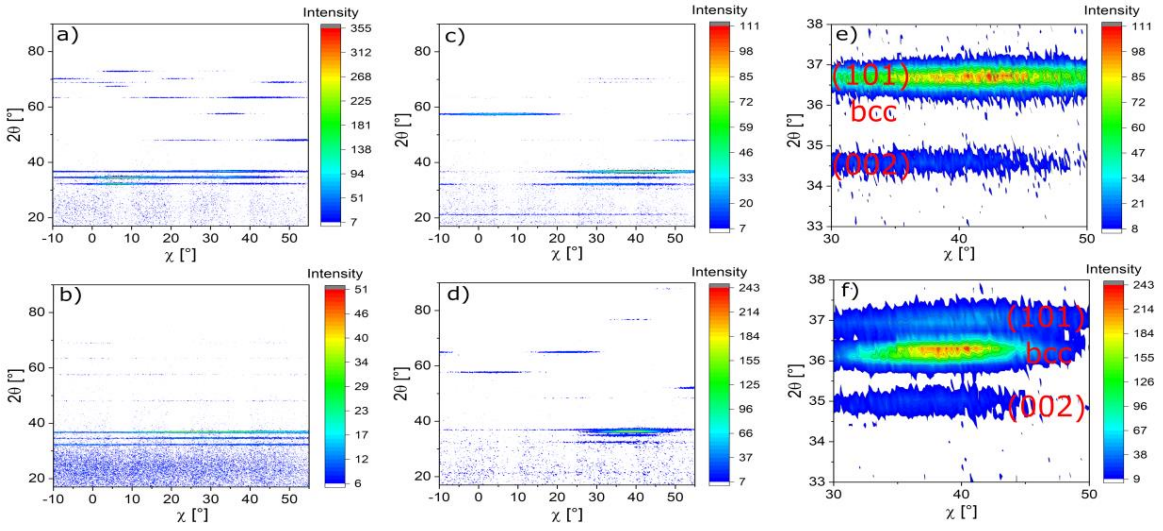

Figure 1 Reciprocal space maps measured with 2D- detector and sample tilting to χ=0°,15°,30°,45° for a) Mg-1.6Li b) Mg-3Li c) Mg-5.5Li d) Mg-9.5Li and zoomed in area around the (002) and (101) hcp and (110) bcc peak for e) Mg-5.5Li and f) Mg-9.5Li.

	Mg-1.6Li	Mg-3Li	Mg-5.5Li	Mg-9.5Li
a [Å]	3.208±0.002	3.202±0.002	3.196±0.004	3.200±0.002
c [Å]	5.197±0.005	5.175±0.007	5.156±0.010	5.161±0.008

Table 2 Average lattice constants *a* und *c* and standard deviations calculated from XRD results for Mg-Li alloys (Li: 1.6 %(m/m), 3 %(m/m), 5.5 %(m/m), 9.5 %(m/m)).

	Mg-1.6Li	Mg-3Li	Mg-5.5Li	Mg-9.5Li
hcp				
100	32.16±0.03	32.25±0.03	32.35±0.08	32.27±0.06
002	34.48±0.03	34.67±0.06	34.78±0.07	34.75±0.07
101	36.63±0.03	36.75±0.03	36.87±0.08	36.78±0.05
102	47.90±0.02	48.09±0.03	48.28±0.10	48.21±0.04
110	57.44±0.01	57.55±0.03	57.69±0.09	57.62±0.05
103	63.26±0.02	63.51±0.04	63.79±0.09	63.75±0.05
200	67.40±0.02	67.56±0.03	67.71±0.07	67.57±0.01
112	68.79±0.02	69.00±0.02	69.16±0.09	69.11±0.06
201	70.11±0.02	70.28±0.04	70.42±0.10	70.33±0.03
004	72.85±0.07	73.21±0.09	73.45	73.48±0.01
202		78.24±0.05		78.33±0.01
104	81.90±0.04	82.23±0.06	82.64±0.12	82.65±0.10
bcc				
110			36.10±0.07	36.03±0.06
200			51.66±0.10	51.48
211			64.89±0.06	64.84±0.07
Li_2CO_3				
110			21.39±0.09	21.29±0.06
200			23.38±0.06	23.32±0.07
$11\bar{1}$			23.49	
111			29.48±0.04	29.38±0.03
$20\bar{2}$			30.67±0.09	30.52±0.06
002			31.77±0.06	31.65±0.05
$11\bar{2}$			34.11±0.01	34.02±0.06
020			36.13±0.03	36.06±0.03
021			39.65±0.01	39.64±0.10
310			39.93±0.02	39.91
$22\bar{1}$				42.60
112				42.60
220			43.55±0.02	43.45
130				56.77±0.04
$33\bar{1}$				65.41

Table 3 Average 2θ angles (°) from XRD diffractograms for Mg-1.6Li, Mg-3Li, Mg-5.5Li and Mg-9.5Li with corresponding miller indices for hcp and bcc Mg-Li and Li_2CO_3 with. A minimum of three samples was measured and standard deviations are given if the peak was present in multiple diffractograms.

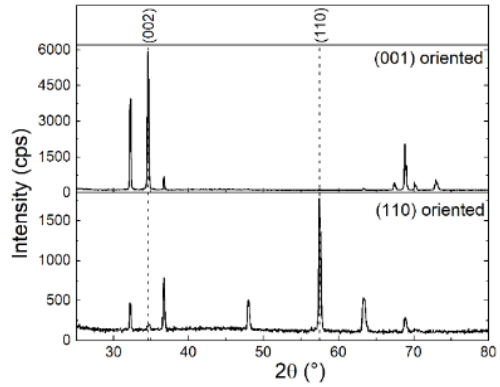

Figure 2 XRD diffractograms for Mg-1.6Li thin films with orientations of (002) and (110). The main orientations are indicated.

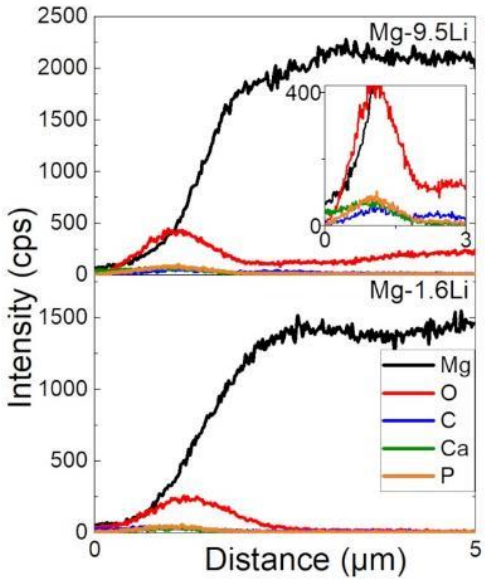

Figure 3 EDX line scans of cross sections of Mg-1.6Li and Mg-9.5Li thin films after corrosion in HBSS over 3-5 days. The inset shows the area of the corrosion layer.

MgLi alloy	Power (W)	Pressure (10^{-3} mbar)	Sputtering rate (nm/s)
Mg-1.6Li	50	2.3	1.45
Mg-3Li	50	3.3	1.75
Mg-5.5Li	50	2.5	1.17
Mg-9.5Li	50	2.3	0.88

Table 4 Sputter parameters for Mg-Li sputtering at standard parameters for stress-free freestanding thin films and for Mg-3Li at different pressure and power.

A.2 Supplement Investigation of in-situ ion release and surface film formation of hcp Mg-Li thin films

Supplementary - Investigation of in-situ ion release and surface film formation of hcp Mg-Li thin films

Lisa Hanke[1], Lukas Kalchgruber[2], Ulrike Westernströer[3], Dieter Garbe-Schönberg[3], Eckhard Quandt[1], Markus Valtiner[2]

[1]Inorganic Functional Materials, Institute for Materials Science, Kiel University, Kiel, Germany

[2]Applied Interface Physics, Institute of Applied Physics, Vienna University of Technology, Vienna, Austria

[3]Marine Climate Research, Institute of Geosciences, Kiel University, Kiel, Germany

1. Calculation of dissolved mass during 3-day corrosion, measured by ICP-MS

	Time	c_{Mg} [µg/L]	c_{Li} [µg/L]
Blank		17910	<1
Mg-1.6Li, sample 1	1 h	19139	12
	4 h	19539	35
	1 day	24593	142
	3 days	36108	433
Mg-1.6Li, sample 2	1 h	22117	16
	4 h	19786	43
	1 day	27067	226
	3 days	43626	661
Mg-3Li, sample 1	1 h	18132	32
	4 h	20292	67
	1 day	25677	360
	3 days	29598	812
Mg-3Li, sample 2	1 h	20210	47
	4 h	19141	98
	1 day	27323	379
	3 days	39602	888
Mg-5.5Li, sample 1	1 h	17134	111
	4 h	20852	213
	1 day	21810	847
	3 days	37944	2120
Mg-5.5Li, sample 2	1 h	19140	98
	4 h	20840	224
	1 day	26640	1598
	3 days	41950	4714

Table 1. Measured Mg and Li concentrations by ICP-MS in a blank HBSS solution (155 mmol, Hanks´ balanced salts H1387, Sigma-Aldrich with added sodium bicarbonate (0.35 g/L)), and after 1 h, 4 h, 1 day and 3 days of corrosion of Mg-1.6Li, Mg-3Li and Mg-5.5Li thin films in the solution at 37±1 °C and pH 7.4±0.2.

The mass of the element (Mg or Li) in the solution at a certain measurement step m_i can be directly determined from the concentration c_i determined (listed in table 1) and the volume adjusted by the

evaporation loss V_i. However, to calculate the overall mass released into the solution $m_{g,i}$, the amount of extracted solution (in the experiments of this study 15 ml) needs to be taken into account. Thus, $m_{g,i}$ can be described by

$$m_{g,i} = m_{g,i-1} + m_i - m_{l,i-1}$$

With $m_{l,i-1}$ as the remaining mass of the element in the overall solution after sample extraction for the step before. c_0 is the concentration of element in the blank solution which is added in the same amount as solution is extracted.

$$\mathrm{m_{l,i}} = \frac{\mathrm{m_i}}{\mathrm{V_i}} \cdot (\mathrm{V_i} - 15\mathrm{ml}) + \mathrm{c_0} \cdot 15\mathrm{mL}$$

2. Additional results

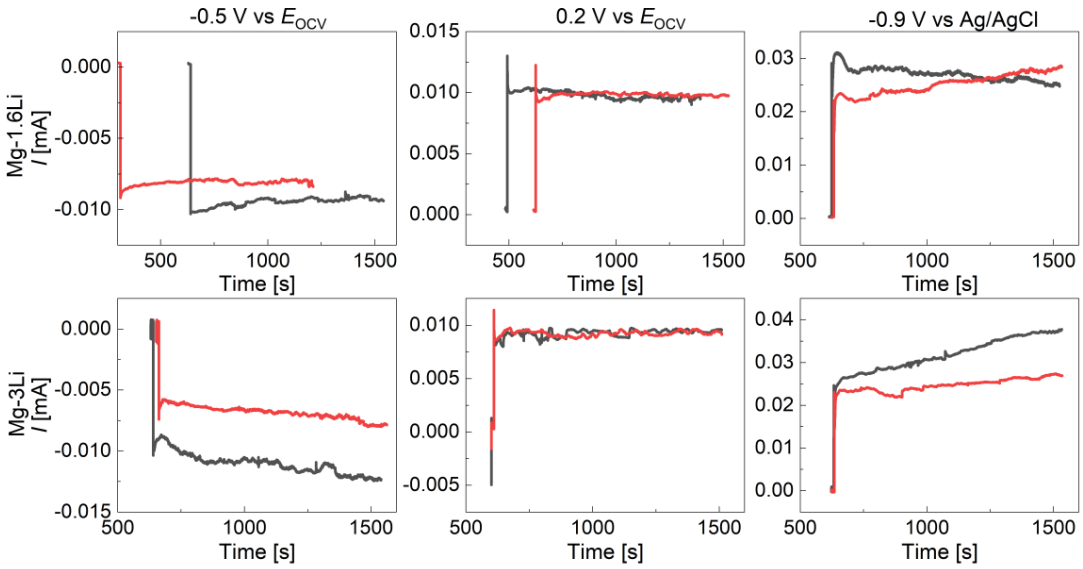

Figure 1. Current *I* measured by the potentiostat in the flow cell at constant voltages of -0.5 V vs E_{OCV}, 0.2 V vs E_{OCV} and -0.9 V vs Ag/AgCl during 15 min after 10 min at E_{OCV} for two samples per alloy (Mg-1.6Li and Mg-3Li).

	$i_{Mg,CV}/i_{Li,CV}$ (E_{OCV})	$i_{Mg,CV}/i_{Li,CV}$ (-0.9 V vs Ag/AgCl)	$i_{Mg,CV}/i_{Li,CV}$ (+0.2 V vs E_{OCV})
Mg-1.6Li	44.3±2.0	64.4±5.2	55.3±1.5
Mg-3Li	20.7±2.6	211.1±45.5	29.1±3.7

Table 2. Ratio of averaged Mg and Li current density during 15 min at a constant potential of E_{OCV}, anodic polarization of -0.9 V vs Ag/AgCl or +0.2 V vs E_{OCV} after 10 min at E_{OCV} for Mg-1.6Li and Mg-3Li thin films.

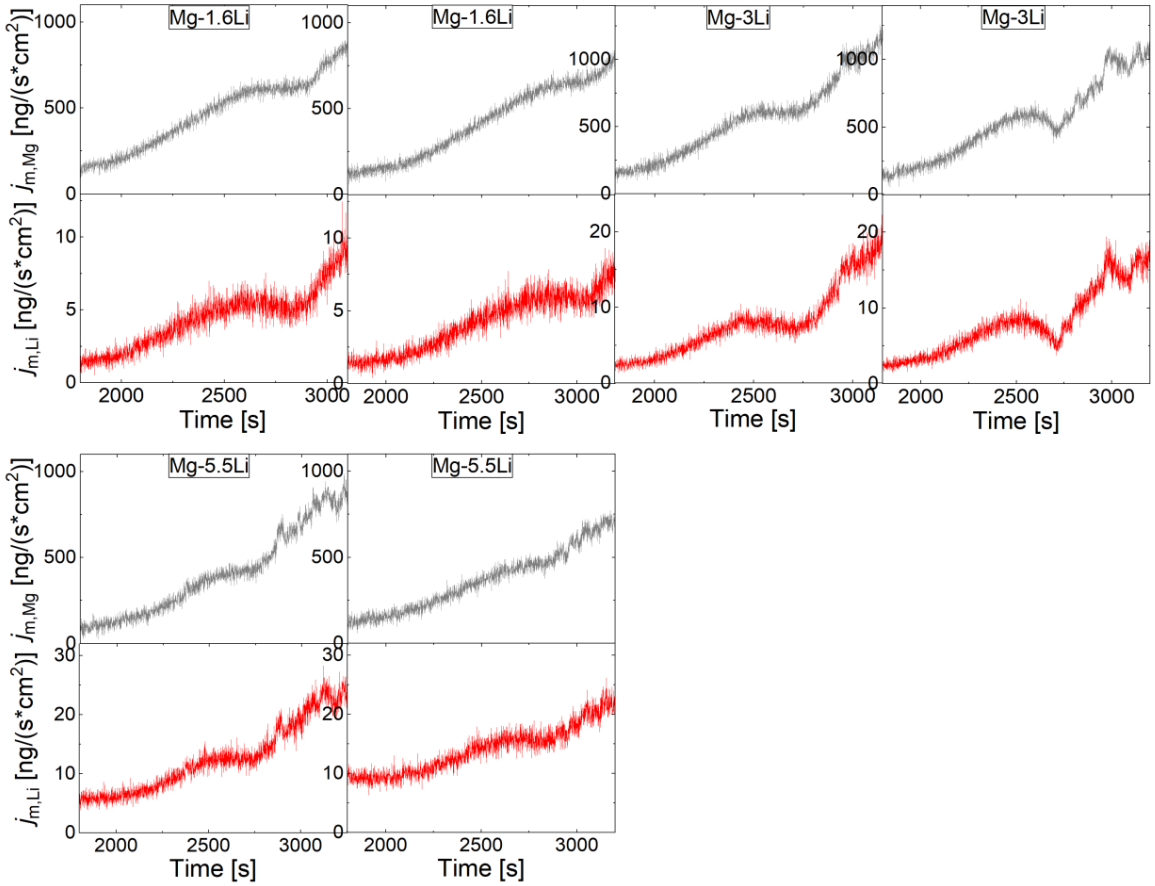

Figure 2. Dissolution rate for two samples per alloy (Mg-1.6Li and Mg-3Li) over LSV from E_{OCV} until -0.5 V vs Ag/AgCl, measured in situ by ICP-MS. The linear sweep is performed after 10 min OCV, 15 min conditioning and further 5 min OCV.

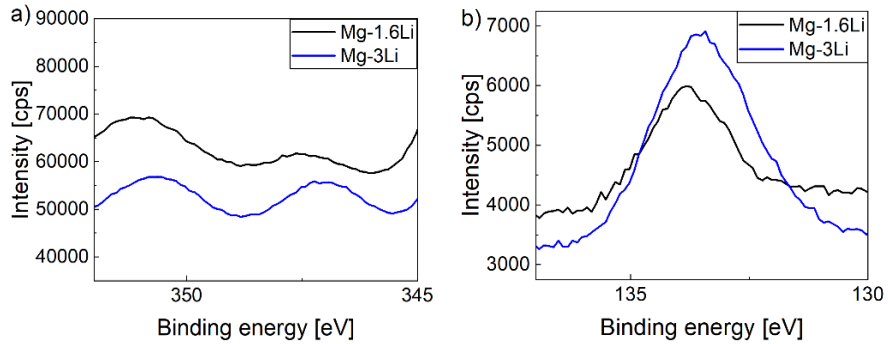

Figure 3. XPS spectra for a) Ca 2p and b) P 2p for Mg-1.6Li and Mg-3Li thin films after 1 h corrosion and storage in ethanol.

A.3 Supplement Tailoring of Mg and MgLi thin-film corrosion rate with dielectric barrier discharge plasma treatment

Tailoring of Mg and MgLi thin-film corrosion rate with dielectric barrier discharge plasma treatment – Supplementary Information

Lisa Hanke [1], Torge Hartig [2], Felix Weisheit [1], Tim Tjardts [2], Tim Pogoda [2], Franz Faupel [2] and Eckhard Quandt [1]

[1] Chair for Inorganic Functional Materials, Institute for Materials Science, Faculty of Engineering, Kiel University, Kiel, Germany
[2] Chair for Multicomponent Materials, Institute for Materials Science, Faculty of Engineering, Kiel University, Kiel, Germany

TABLE SI. Atomic concentrations of the surface of untreated MgLi thin films and thin films after 15 s of DBD determined by XPS.

Untreated Sample			Treated Sample		
Element	Peak used for Analysis	Relative Amount (at%)	Element	Peak used for Analysis	Relative Amount (at%)
C	C 1s	31.16	C	C 1s	13.00
O	O 1s	43.94	O	O 1s	61.74
Mg	Mg 2p	0.45	Mg	Mg 2p	19.59
Li	Li 1s	24.45	Li	Li 1s	4.12

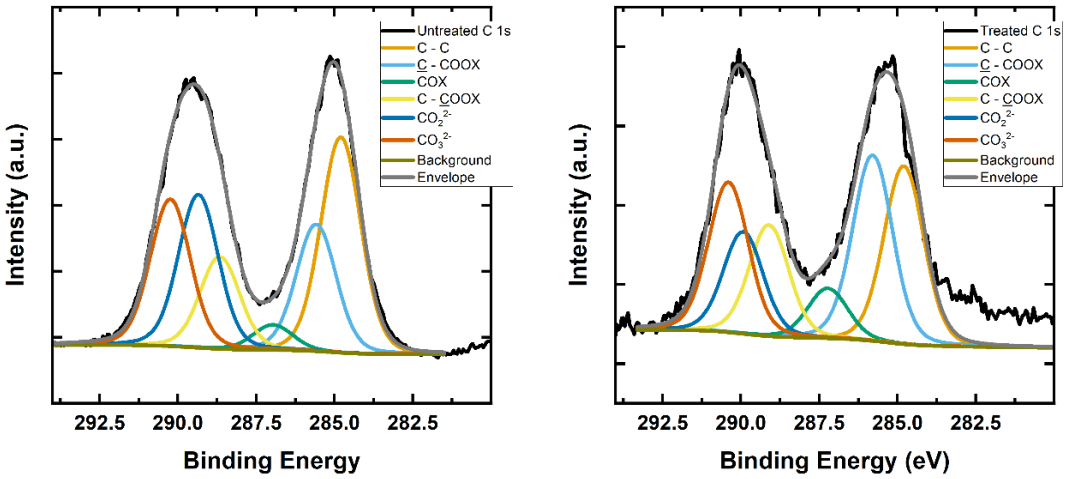

FIG. S1. XPS C 1s spectra of untreated and treated MgLi thin films with all fitted compounds, fitting according to Fotea et al.[62]. The increased intensity for the treated sample at lower binding energy might be influenced by charging effects.

TABLE SII. Binding energy positions and full-width-at-half-maximum (fwhm) of components measured by XPS on the surface of untreated MgLi thin film samples.

Characteristic Peak	Component	Binding Energy Position (eV)	Fwhm (eV)
O 1s	Carbonates	533.6	1.9
	Hydroxides	532.2	1.9
	Oxides	530.6	1.9
Li 1s	Li_2O, LiOH, Li_2CO_3	55.3	1.8
Mg 2p	$Mg(OH)_2$, $MgCO_3$	49.9	2.0
C 1s	CO_3^{2-}	290.2	1.5
	CO_2^{2-}	289.3	1.5
	C - COOX	288.7	1.5
	COX	287.0	1.5
	C - COOX	285.6	1.5
	C - C	284.8	1.5

TABLE SIII. Binding energy positions and full-width-at-half-maximum of components measured by XPS on the surface of treated MgLi thin film samples.

Characterisitc Peak	Component	Binding Energy Position (eV)	Fwhm (eV)
O 1s	Carbonates	533.5	2.0
	Hydroxides	531.9	2.0
	Oxides	529.5	2.0
Li 1s	Li_2O, LiOH, Li_2CO_3	55.5	1.5
Mg 2p	$Mg(OH)_2$, $MgCO_3$	49.8	1.9
C 1s	CO_3^{2-}	290.3	1.5
	CO_2^{2-}	289.9	1.5
	C - COOX	289.1	1.5
	COX	287.2	1.5
	C - COOX	285.8	1.5
	C - C	284.8	1.5

Full List of Publications

- **Hanke, L.**, Kalchgruber, L., Westernströer, U., Garbe-Schönberg, D., Quandt, E., Valtiner, M., Investigation of in-situ ion release and surface film formation of hcp Mg-Li thin films. *Corrosion Science* 238, 112361 (2024), 10.1016/j.corsci.2024.112361.

- Bhat, K., **Hanke, L.**, Helmholz, H., Quandt, E., Pixley, S., Willumeit-Römer, R., Influence of Magnesium Degradation on Schwannoma Cell Responses to Nerve Injury Using an In Vitro Injury Model. *Journal of Functional Biomaterials* 15, 88 (2024), 10.1016/10.3390/jfb15040088.

- Bhat, K., Schlotterose, L., **Hanke, L.**, Helmholz, H., Quandt, E., Hattermann, K., Willumeit-Römer, R., Magnesium-lithium thin films for neurological applications - an *in vitro* investigation of glial cytocompatibility and neuroinflammatory response. *Acta Biomaterialia* 178, 307-319 (2024), 10.1016/j.actbio.2024.02.018.

- **Hanke, L.**, Hartig, T., Weisheit, F., Tjardts, T., Pogoda, T., Faupel, F., Quandt, E., Tailoring of Mg and MgLi thin-film corrosion rates with dielectric barrier discharge plasma treatment. *Journal of Vacuum Science and Technology A* 41, 053109 (2023), 10.1116/6.0002783.

- **Hanke, L.**, Jessen, L.K., Weisheit, F., Bhat, K., Westernströer, U., Garbe-Schönberg, D., Willumeit-Römer, R., Quandt, E., Structural characterisation and degradation of Mg–Li thin films for biodegradable implants. *Scientific Reports* 13, 12572 (2023), 10.1038/s41598-023-39493-9.

- Arivanandhan, G., Li, Z., Curtis, S., **Hanke, L.**, Quandt, E., Kohl, M., Power Optimization of TiNiHf/Si Shape Memory Microactuators. *Actuators* 12, 82 (2023), 10.3390/act12020082.

- Curtis, S., Hörsting, M., Arivanandhan, G., Dengiz, D., Li, Z., Jetter, J., **Hanke, L.**, Bumke, L., Quandt, E., Wulfinghoff, S., Kohl, M., TiNiHf/SiO_2/Si shape memory film composites for bi-directional micro actuation. *International Journal of Smart and Nano Materials* 13, 293-314 (2022), 10.1080/19475411.2022.2071352.

Conference Presentations

- L. Hanke, D. Dengiz, F. Weisheit, E. Quandt, Self-expanding-partial biodegradable composite implants, Oral presentation in Annual Congress of the European Federation of Corrosion (Eurocorr) 2023, Brussels, Belgium, August 27-31, 2023.
- L. Hanke, K. Bhat, L. Kalchgruber, M. Valtiner, R. Willumeit-Römer, E. Quandt, Magnetronsputtered MgLi Coatings and Freestanding Thin Films for Neurological Implants – Preparation and Degradation Process, Oral presentation in Pacific Rim Symposium on Surfaces, Coatings and Interfaces (PacSurf) 2022, Puako, USA (HI), December 11-15, 2022.
- L. Hanke, T. Hartig, F. Weisheit, T. Tjardts, M. Valtiner, F. Faupel, E. Quandt, Tailoring of Mg Thin-Film Corrosion Properties with Dielectric Barrier Discharge Plasma Treatment, Poster presentation in PacSurf 2022, Puako, USA (HI), December 11-15, 2022.
- L. Hanke, L. Kalchgruber, K. Bhat, R. Willumeit-Römer, M. Valtiner, E. Quandt, Degradation and ion release of Mg-Li thin films for potential neurological applications, Oral presentation in Eurocorr 2022, Berlin, Germany, August 28- September 1, 2022.

Symbols and Abbreviations

$\boldsymbol{\alpha}$	transfer coefficient
$\boldsymbol{A}$	area
$\boldsymbol{a}$, $\boldsymbol{c}$	lattice parameters
AAS	atomic absorption spectrometry
aCSF	artificial cerebrospinal fluid
AESEC	atomic emission spectroelectrochemistry
AFM	atomic force microscopy
at% , %(n/n)	atomic percent
AZ alloy	aluminium + zinc alloy
bcc	body centred cubic
$\boldsymbol{c(t)}$	concentration
CE	counter electrode
$\boldsymbol{CR}$	corrosion rate
CVD	chemical vapour deposition
$\boldsymbol{d}$	thickness
DMEM	Dulbecco's modified Eagle's solution
$\boldsymbol{\eta}$	overpotential
$\boldsymbol{E}$	potential
$\boldsymbol{E_{\mathrm{OCV}}}$	open circuit potential / corrosion potential
EDX	energy dispersive X-ray spectroscopy
EIS	electrochemical impedance spectroscopy
$\boldsymbol{f}$	flow rate
$\boldsymbol{F}$	Faraday constant
HBSS	Hank's balanced salt solution
hcp	hexagonal close packed
$\boldsymbol{i}$	current density
$\boldsymbol{i_0}$	corrosion current density/ exchange current density
ICP-AES	inductively coupled plasma - atomic emmission spectrometry
ICP-MS	inductively coupled plasma - mass spectrometry
ICP-OES	inductively coupled plasma - optical emission spectrometry
ICP-RIE	inductively coupled plasma - reactive ion etching
$\boldsymbol{j_{\mathrm{m}}}$	dissolution rate
$\boldsymbol{K_{\mathrm{sp}}}$	solubility product constant
LA alloy	lithium aluminium alloy
LZ alloy	lithium + zinc alloy
$\boldsymbol{m}$	mass
$\boldsymbol{M}$	molar mass
$\boldsymbol{n}$	electrons released per atom
NDE	negative difference effect
PBR	Pilling-Bedworth ratio
PVD	physical vapour deposition
$\boldsymbol{\rho}$	density

$\boldsymbol{R}$	gas constant
RE	reference electrode
REE	rare earth elements
SEM	scanning electron microscopy
SHE	standard hydrogen electrode
$\boldsymbol{t}$	time
$\boldsymbol{T}$	temperature
$\boldsymbol{T_{\mathrm{m}}}$	melting temperature
$\boldsymbol{T_{\mathrm{s}}}$	substrate temperature
WE	working electrode
WE alloy	yttrium + rare earth element alloy
wt% , %(m/m)	weight percent, mass percent
XPS	X-ray photoelectron spectroscopy
XRD	X-ray diffraction

List of Figures

List of Tables

Bibliography

1. Hammond, C. R. & Lide, D. R. *The Elements* in *CRC handbook of chemistry and physics: a ready reference book of chemical and physical data* (eds Rumble, J. R., Bruno, T. J. & Doa, M. J.) 103rd ed., 4-1–4-38 (CRC press, 2022).
2. Schmidt, M. Rohstoffrisikobewertung – Lithium. *DERA Rohstoffinformationen* **54,** 81 (2023).
3. Volkmann, C., Bschor, T. & Köhler, S. Lithium Treatment Over the Lifespan in Bipolar Disorders. *Frontiers in Psychiatry* **11,** 377 (2020).
4. Kamal, Z. M., Dutta, S., Rahman, S., Etando, A., Hasan, E., Nahar, S. N., Wan Ahmad Fakuradzi, W. F. S., Sinha, S., Haque, M. & Ahmad, R. Therapeutic Application of Lithium in Bipolar Disorders: A Brief Review. *Cureus* **14,** e29332 (2022).
5. Can, A., Schulze, T. G. & Gould, T. D. Molecular actions and clinical pharmacogenetics of lithium therapy. *Pharmacology Biochemistry and Behavior* **123,** 3–16 (2014).
6. Lazzara, C. A. & Kim, Y.-H. Potential application of lithium in Parkinson's and other neurodegenerative diseases. *Frontiers in Neuroscience* **9,** 403 (2015).
7. Haupt, M., Bähr, M. & Doeppner, T. R. Lithium beyond psychiatric indications: the reincarnation of a new old drug. *Neural Regeneration Research* **16,** 2383–2387 (2021).
8. Haussmann, R., Noppes, F., Brandt, M. D., Bauer, M. & Donix, M. Minireview: Lithium: a therapeutic option in Alzheimer's disease and its prodromal stages? *Neuroscience Letters* **760,** 136044 (2021).
9. Forlenza, O. V., De-Paula, V. J. R. & Diniz, B. S. O. Neuroprotective Effects of Lithium: Implications for the Treatment of Alzheimer's Disease and Related Neurodegenerative Disorders. *ACS Chemical Neuroscience* **5,** 443–450 (2014).
10. Matsunaga, S., Kishi, T., Annas, P., Basun, H., Hampel, H. & Iwata, N. Lithium as a Treatment for Alzheimer's Disease: A Systematic Review and Meta-Analysis. *Journal of Alzheimer's Disease* **48,** 403–410 (2015).
11. Vallée, A., Vallée, J.-N. & Lecarpentier, Y. Parkinson's Disease: Potential Actions of Lithium by Targeting the WNT/β-Catenin Pathway, Oxidative Stress, Inflammation and Glutamatergic Pathway. *Cells* **10,** 230 (2021).
12. Zheng, Y., Gu, X. & Witte, F. Biodegradable metals. *Materials Science and Engineering: R: Reports* **77,** 1–34 (2014).
13. Gitlin, M. Lithium side effects and toxicity: prevalence and management strategies. *International Journal of Bipolar Disorders* **4,** 27 (2016).
14. Ferensztajn-Rochowiak, E. & Rybakowski, J. K. Long-Term Lithium Therapy: Side Effects and Interactions. *Pharmaceuticals* **16,** 74 (2023).
15. Alexander, M. P., Farag, Y. M. K., Mittal, B. V., Rennke, H. G. & Singh, A. K. Lithium toxicity: A double-edged sword. *Kidney International* **73,** 233–237 (2008).

16. Severus, W., Kleindienst, N., Seemüller, F., Frangou, S., Möller, H. & Greil, W. What is the optimal serum lithium level in the long-term treatment of bipolar disorder – a review? *Bipolar Disorders* **10,** 231–237 (2008).

17. Sun, Y., Zhang, H., Zhang, Y., Liu, Z., He, D., Xu, W., Li, S., Zhang, C. & Zhang, Z. Li–Mg–Si bioceramics provide a dynamic immuno-modulatory and repair-supportive microenvironment for peripheral nerve regeneration. *Bioactive Materials* **28,** 227–242 (2023).

18. Li, L., Peng, X., Qin, Y., Wang, R., Tang, J., Cui, X., Wang, T., Liu, W., Pan, H. & Li, B. Acceleration of bone regeneration by activating Wnt/β-catenin signalling pathway via lithium released from lithium chloride/calcium phosphate cement in osteoporosis. *Scientific Reports* **7,** 45204 (2017).

19. He, F., Yuan, X., Lu, T., Wang, Y., Feng, S., Shi, X., Wang, L., Ye, J. & Yang, H. Preparation and characterization of novel lithium magnesium phosphate bioceramic scaffolds facilitating bone generation. *Journal of Materials Chemistry B* **10,** 4040–4047 (2022).

20. Kocman, A. E., Dag, I., Sengel, T., Soztutar, E. & Canbek, M. The effect of lithium and lithium-loaded hyaluronic acid hydrogel applications on nerve regeneration and recovery of motor functions in peripheral nerve injury. *Rendiconti Lincei. Scienze Fisiche e Naturali* **31,** 889–904 (2020).

21. Li, H., Zheng, Y. & Qin, L. Progress of biodegradable metals. *Progress in Natural Science: Materials International* **24,** 414–422 (2014).

22. Khan, A. R., Grewal, N. S., Zhou, C., Yuan, K., Zhang, H.-J. & Jun, Z. Recent advances in biodegradable metals for implant applications: Exploring in vivo and in vitro responses. *Results in Engineering* **20,** 101526 (2023).

23. Jurgeleit, T., Quandt, E. & Zamponi, C. Mechanical Properties and In Vitro Degradation of Sputtered Biodegradable Fe-Au Foils. *Materials* **9,** 928 (2016).

24. Maier, J. A. M., Locatelli, L., Fedele, G., Cazzaniga, A. & Mazur, A. Magnesium and the Brain: A Focus on Neuroinflammation and Neurodegeneration. *International Journal of Molecular Sciences* **24,** 223 (2023).

25. Kirkland, A., Sarlo, G. & Holton, K. The Role of Magnesium in Neurological Disorders. *Nutrients* **10,** 730 (2018).

26. Haffner, D., Zamponi, C., Lima de Miranda, R. & Quandt, E. Micropatterned freestanding magnetron sputtered Mg-alloy scaffolds. *BioNanoMaterials* **16,** 19–22 (2015).

27. Jessen, L. K., Zamponi, C., Willumeit-Römer, R. & Quandt, E. Magnetron sputtered freestanding MgAg films with ultra-low corrosion rate. *Acta Biomaterialia* **98,** 81–87 (2019).

28. Jessen, L. K., Zamponi, C. & Quandt, E. Mechanical Properties of Magnetron Sputtered Free Standing Mg-Ag Alloy Films. *Frontiers in Materials* **6,** 236 (2019).

29. Schlüter, K., Zamponi, C., Hapke, J., Hort, N., Kainer, K. U. & Quandt, E. Mechanical properties and corrosion behaviour of freestanding, precipitate-free magnesium WE43 thin films. *International Journal of Materials Research* **104,** 286–292 (2013).

30. Schlüter, K., Zamponi, C., Hort, N., Kainer, K. & Quandt, E. Polycrystalline and amorphous MgZnCa thin films. *Corrosion Science* **63,** 234–238 (2012).

31. Schlüter, K., Shi, Z., Zamponi, C., Cao, F., Quandt, E. & Atrens, A. Corrosion performance and mechanical properties of sputter-deposited MgY and MgGd alloys. *Corrosion Science* **78,** 43–54 (2014).

32. Schlüter, K., Zamponi, C., Piorra, A. & Quandt, E. Comparison of the corrosion behaviour of bulk and thin film magnesium alloys. *Corrosion Science* **52,** 3973–3977 (2010).

33. Ma, X.-c., Jin, S.-y., Wu, R.-z., Wang, J.-x., Wang, G.-x., Krit, B. & Betsofen, S. Corrosion behavior of Mg-Li alloys: A review. *Transactions of Nonferrous Metals Society of China* **31,** 3228–3254 (2021).

34. Atrens, A., Song, G.-L., Liu, M., Shi, Z., Cao, F. & Dargusch, M. S. Review of Recent Developments in the Field of Magnesium Corrosion. *Advanced Engineering Materials* **17,** 400–453 (2015).

35. Li, X., Liu, X., Wu, S., Yeung, K., Zheng, Y. & Chu, P. K. Design of magnesium alloys with controllable degradation for biomedical implants: From bulk to surface. *Acta Biomaterialia* **45,** 2–30 (2016).

36. Chaya, A., Yoshizawa, S., Verdelis, K., Myers, N., Costello, B. J., Chou, D.-T., Pal, S., Maiti, S., Kumta, P. N. & Sfeir, C. In vivo study of magnesium plate and screw degradation and bone fracture healing. *Acta Biomaterialia* **18,** 262–269 (2015).

37. Noviana, D., Paramitha, D., Ulum, M. F. & Hermawan, H. The effect of hydrogen gas evolution of magnesium implant on the postimplantation mortality of rats. *Journal of Orthopaedic Translation* **5,** 9–15 (2016).

38. *Physical Constants of Inorganic Compounds* in *CRC handbook of chemistry and physics: a ready reference book of chemical and physical data* (eds Rumble, J. R., Bruno, T. J. & Doa, M. J.) 103rd ed., 4-58–4-69 (CRC press, 2022).

39. Matli, P. R., Krishnan, A. V., Manakari, V., Parande, G., Chua, B. W., Wong, S. C. K., Lim, C. Y. H. & Gupta, M. A new method to lightweight and improve strength to weight ratio of magnesium by creating a controlled defect. *Journal of Materials Research and Technology* **9,** 3664–3675 (2020).

40. Xu, W., Birbilis, N., Sha, G., Wang, Y., Daniels, J. E., Xiao, Y. & Ferry, M. A high-specific-strength and corrosion-resistant magnesium alloy. *Nature Materials* **14,** 1229–1235 (2015).

41. Neelameggham, N. R. & Brown, B. *11. Magnesium* in *Critical Metals Handbook* (ed Gunn, G.) 261–283 (American Geophysical Union, 2014).

42. Becerra, A. & Pekguleryuz, M. Effects of lithium, indium, and zinc on the lattice parameters of magnesium. *Journal of Materials Research* **23,** 3379–3386 (2008).

43. Agnew, S. R. & Duygulu, Ö. Plastic anisotropy and the role of non-basal slip in magnesium alloy AZ31B. *International Journal of Plasticity* **21,** 1161–1193 (2005).

44. Khosravani, A., Fullwood, D., Adams, B., Rampton, T., Miles, M. & Mishra, R. Nucleation and propagation of $\{ 1\ 0\ \bar{1}\ 2 \}$ twins in AZ31 magnesium alloy. *Acta Materialia* **100,** 202–214 (2015).

45. Wang, X., Jiang, L., Luo, A., Song, J., Liu, Z., Yin, F., Han, Q., Yue, S. & Jonas, J. J. Deformation of twins in a magnesium alloy under tension at room temperature. *Journal of Alloys and Compounds* **594,** 44–47 (2014).

46. Ahmad, Z. *Principles of Corrosion Engineering and Corrosion Control* a) 20, b) 2, c) 120-183 (Elsevier Science & Technology, 2006).

47. Costello, R. B. & Rosanoff, A. *Magnesium* in *Present Knowledge in Nutrition : Basic Nutrition and Metabolism* (eds Marriott, B. P., Birt, D. F., Stalling, V. A. & Yates, A. A.) 11th ed., 339–373 (Elsevier Science & Technology, 2020).

48. Topf, J. M. & Murray, P. T. Hypomagnesemia and Hypermagnesemia. *Reviews in Endocrine and Metabolic Disorders* **4,** 195–206 (2003).

49. Witte, F. The history of biodegradable magnesium implants: A review. *Acta Biomaterialia* **6,** 1680–1692 (2010).

50. Huse, E. C. A New Ligature. *The Chicago Medical Journal and Examiner* **37,** 171–172 (1878).

51. Song, G. Control of biodegradation of biocompatable magnesium alloys. *Corrosion Science* **49,** 1696–1701 (2007).

52. De Hemptinne, Q., Xaplanteris, P., Guédès, A., Demeure, F., Vandeloo, B., Dugauquier, C., Picard, F., Warne, D. W., Pilgrim, T., Iglesias, J. F. & Bennett, J. Magmaris Resorbable Magnesium Scaffold Versus Conventional Drug-Eluting Stent in ST-Segment Elevation Myocardial Infarction: 1-Year Results of a Propensity-Score-Matching Comparison. *Cardiovascular Revascularization Medicine* **43,** 28–35 (2022).

53. Song, G., Zhao, H. Q., Liu, Q. & Fan, Z. A review on biodegradable biliary stents: materials and future trends. *Bioactive Materials* **17,** 488–495 (2022).

54. Chen, X., Xia, Y., Shen, S., Wang, C., Zan, R., Yu, H., Yang, S., Zheng, X., Yang, J., Suo, T., Gu, Y. & Zhang, X. Research on the Current Application Status of Magnesium Metal Stents in Human Luminal Cavities. *Journal of Functional Biomaterials* **14,** 462 (2023).

55. May, H., Alper Kati, Y., Gumussuyu, G., Yunus Emre, T., Unal, M. & Kose, O. Bioabsorbable magnesium screw versus conventional titanium screw fixation for medial malleolar fractures. *Journal of Orthopaedics and Traumatology* **21,** 9 (2020).

56. Kačarević, Ž. P., Rider, P., Elad, A., Tadic, D., Rothamel, D., Sauer, G., Bornert, F., Windisch, P., Hangyási, D. B., Molnar, B., Kämmerer, T., Hesse, B., Bortel, E., Bartosch, M. & Witte, F. Biodegradable magnesium fixation screw for barrier membranes used in guided bone regeneration. *Bioactive Materials* **14,** 15–30 (2022).

57. Tian, P. & Liu, X. Surface modification of biodegradable magnesium and its alloys for biomedical applications. *Regenerative Biomaterials* **2,** 135–151 (2015).

58. Xu, C., Wang, S., Wang, H., Liu, K., Zhang, S., Chen, B., Liu, H., Tong, F., Peng, F., Tu, Y. & Li, Y. Magnesium-Based Micromotors as Hydrogen Generators for Precise Rheumatoid Arthritis Therapy. *Nano Letters* **21,** 1982–1991 (2021).

59. Ranathunge, T. A., Karunaratne, D. G. G. P., Rajapakse, R. M. G. & Watkins, D. L. Doxorubicin Loaded Magnesium Oxide Nanoflakes as pH Dependent Carriers for Simultaneous Treatment of Cancer and Hypomagnesemia. *Nanomaterials* **9,** 208 (2019).

60. Nyabadza, A., Shan, C., Murphy, R., Vazquez, M. & Brabazon, D. Laser-synthesised magnesium nanoparticles for amino acid and enzyme immobilisation. *OpenNano* **11,** 100133 (2023).

61. Zaatreh, S., Haffner, D., Strauß, M., Wegner, K., Warkentin, M., Lurtz, C., Zamponi, C., Mittelmeier, W., Kreikemeyer, B., Willumeit-Römer, R., Quandt, E. & Bader, R. Fast corroding, thin magnesium coating displays antibacterial effects and low cytotoxicity. *Biofouling* **33,** 294–305 (2017).

62. Loukil, N. *Alloying Elements of Magnesium Alloys: A Literature Review* in *Magnesium Alloys Structure and Properties* (eds Tański, T. A. & Jarka, P.) chap. 9 (IntechOpen, 2021).

63. Angrisani, N., Reifenrath, J., Zimmermann, F., Eifler, R., Meyer-Lindenberg, A., Vano-Herrera, K. & Vogt, C. Biocompatibility and degradation of LAE442-based magnesium alloys after implantation of up to 3.5 years in a rabbit model. *Acta Biomaterialia* **44,** 355–365 (2016).

64. Ding, Y., Wen, C., Hodgson, P. & Li, Y. Effects of alloying elements on the corrosion behavior and biocompatibility of biodegradable magnesium alloys: a review. *Journal of Materials Chemistry B* **2,** 1912–1933 (2014).

65. Bach, F. W., Schaper, M. & Jaschik, C. Influence of Lithium on hcp Magnesium Alloys. *Materials Science Forum* **419-422,** 1037–1042 (2003).

66. Wu, J., Zhao, D., Ohodnicki, J. M., Lee, B., Roy, A., Yao, R., Chen, S., Dong, Z., Heineman, W. R. & Kumta, P. N. In Vitro and in Vivo Evaluation of Multiphase Ultrahigh Ductility Mg–Li–Zn Alloys for Cardiovascular Stent Application. *ACS Biomaterials Science & Engineering* **4,** 919–932 (2018).

67. Xia, D., Liu, Y., Wang, S., Zeng, R.-C., Liu, Y., Zheng, Y. & Zhou, Y. In vitro and in vivo investigation on biodegradable Mg-Li-Ca alloys for bone implant application. *Science China Materials* **62,** 256–272 (2019).

68. Feyerabend, F., Fischer, J., Holtz, J., Witte, F., Willumeit, R., Drücker, H., Vogt, C. & Hort, N. Evaluation of short-term effects of rare earth and other elements used in magnesium alloys on primary cells and cell lines. *Acta Biomaterialia* **6,** 1834–1842 (2010).

69. Agarwal, S., Curtin, J., Duffy, B. & Jaiswal, S. Biodegradable magnesium alloys for orthopaedic applications: A review on corrosion, biocompatibility and surface modifications. *Materials Science and Engineering: C* **68,** 948–963 (2016).

70. Gu, X.-N. & Zheng, Y.-F. A review on magnesium alloys as biodegradable materials. *Frontiers of Materials Science in China* **4,** 111–115 (2010).

71. Sezer, N., Evis, Z., Kayhan, S. M., Tahmasebifar, A. & Koç, M. Review of magnesium-based biomaterials and their applications. *Journal of Magnesium and Alloys* **6,** 23–43 (2018).

72. Wu, R., Yan, Y., Wang, G., Murr, L. E., Han, W., Zhang, Z. & Zhang, M. Recent progress in magnesium–lithium alloys. *International Materials Reviews* **60,** 65–100 (2015).

73. Haferkamp, H., Jaschik, C., Juchmann, P., Kaese, V., Niemeyer, M. & Tai, P. Entwicklung und Eigenschaften von Magnesium-Lithium-Legierungen. *Materialwissenschaft und Werkstofftechnik* **32,** 25–30 (2001).

74. Witte, F., Hort, N., Vogt, C., Cohen, S., Kainer, K. U., Willumeit, R. & Feyerabend, F. Degradable biomaterials based on magnesium corrosion. *Current Opinion in Solid State and Materials Science* **12,** 63–72 (2008).

75. *Concise Metals Engineering Data Book.* (ed Davis, J. R.) 9 (A S M International, 1997).

76. Nayeb-Hashemi, A. A., Clark, J. B. & Pelton, A. D. The Li-Mg (Lithium-Magnesium) system. *Bulletin of Alloy Phase Diagrams* **5,** 365–374 (1984).

77. Al-Samman, T. Comparative study of the deformation behavior of hexagonal magnesium–lithium alloys and a conventional magnesium AZ31 alloy. *Acta Materialia* **57,** 2229–2242 (2009).

78. Lee, R. E. & Jones, W. J. D. Microplasticity and fatigue of some magnesium-lithium alloys. *Journal of Materials Science* **9,** 469–475 (1974).

79. Zhou, W., Zheng, Y., Leeflang, M. & Zhou, J. Mechanical property, biocorrosion and in vitro biocompatibility evaluations of Mg–Li–(Al)–(RE) alloys for future cardiovascular stent application. *Acta Biomaterialia* **9,** 8488–8498 (2013).

80. Haferkamp, H., Boehm, R., Holzkamp, U., Jaschik, C., Kaese, V. & Niemeyer, M. Alloy Development, Processing and Applications in Magnesium Lithium Alloys. *Materials Transactions* **42,** 1160–1166 (2001).

81. Somekawa, H., Egusa, D. & Abe, E. Grain boundary plasticity in solid solution Mg–Li binary alloy. *Materials Science and Engineering: A* **790,** 139705 (2020).

82. Iwadate, Y., Lassouani, M., Lantelme, F. & Chemla, M. Electrochemical study of mass transfer in Li-Mg and Li-Mg-Al alloys. *Journal of Applied Electrochemistry* **17,** 385–397 (1987).

83. Zhong, W. & Zhao, J.-C. First measurement of diffusion coefficients of lithium in magnesium. *Materialia* **11,** 100674 (2020).

84. Chiu, C.-H., Wu, H.-Y., Wang, J.-Y. & Lee, S. Microstructure and mechanical behavior of LZ91 Mg alloy processed by rolling and heat treatments. *Journal of Alloys and Compounds* **460,** 246–252 (2008).

85. Li, C. Q., Xu, D. K., Wang, B. J., Sheng, L. Y., Qiao, Y. X. & Han, E. H. Natural ageing responses of duplex structured Mg-Li based alloys. *Scientific Reports* **7,** 40078 (2017).

86. Hsu, C.-C., Wang, J.-Y. & Lee, S. Room Temperature Aging Characteristic of MgLiAlZn Alloy. *Materials Transactions* **49,** 2728–2731 (2008).

87. Gould, R. D., Kasap, S. & Ray, A. K. *Thin Films* in *Springer Handbook of Electronic and Photonic Materials* (eds Kasap, S. & Capper, P.) 2nd ed., 645–706 (Springer International Publishing, 2017).

88. Song, N. & Deng, S. *Thin Film Deposition Technologies and Application in Photovoltaics* in *Thin Films - Deposition Methods and Applications* (ed Yang, D.) 3–20 (IntechOpen, 2023).

89. Freund, L. B. & Suresh, S. *Thin Film Materials: Stress, Defect Formation and Surface Evolution* 2–5 (Cambridge University Press, 2004).

90. Mwema, F. M., Akinlabi, E. T. & Oladijo, O. P. *Sputtered Thin Films: Theory and Fractal Descriptions* 3–27 (Taylor & Francis Group, 2021).

91. Ghazal, H. & Sohail, N. *Sputtering Deposition* in *Thin Films - Deposition Methods and Applications* (ed Yang, D.) 21–40 (IntechOpen, 2023).

92. Ohring, M. *Materials Science of Thin Films: Depositon and Structure* 2nd ed., 222–233 (Academic Press, 2002).

93. Movchan, B. A. & Demchishin, A. V. Structure and properties of thick condensates of nickel, titanium, tungsten, aluminum oxides, and zirconium dioxide in vacuum. *Fizika metallov i metallovedenie* **28,** 653–660 (1969).

94. Thornton, J. A. Influence of apparatus geometry and deposition conditions on the structure and topography of thick sputtered coatings. *Journal of Vacuum Science and Technology* **11,** 666–670 (1974).

95. Thornton, J. A. High Rate Thick Film Growth. *Annual Review of Materials Science* **7,** 239–260 (1977).

96. Thornton, J. A. & Hoffman, D. Stress-related effects in thin films. *Thin Solid Films* **171,** 5–31 (1989).

97. Kusano, E. Structure-Zone Modeling of Sputter-Deposited Thin Films: A Brief Review. *Applied Science and Convergence Technology* **28,** 179–185 (2019).

98. Messier, R., Giri, A. P. & Roy, R. A. Revised structure zone model for thin film physical structure. *Journal of Vacuum Science & Technology A* **2,** 500–503 (1984).

99. Barna, P. B. & Adamik, M. Fundamental structure forming phenomena of polycrystalline films and the structure zone models. *Thin Solid Films* **317,** 27–33 (1998).

100. Anders, A. A structure zone diagram including plasma-based deposition and ion etching. *Thin Solid Films* **518,** 4087–4090 (2010).

101. Blawert, C., Heitmann, V., Scharnagl, N., Störmer, M., Lutz, J., Prager-Duschke, A., Manova, D. & Mändl, S. Different Underlying Corrosion Mechanism for Mg Bulk Alloys and Mg Thin Films. *Plasma Processes and Polymers* **6,** S690–S694 (2009).

102. Schlüter, K., Reverey, J., Hort, N., Zamponi, C. & Quandt, E. Mechanical Behaviour and Corrosion Performance of Thin Film Magnesium WE Alloys. *Materials Science Forum* **690,** 286–289 (2011).

103. Davis, J. R. *Corrosion: Understanding the Basics* a) 2-3, b) 35-37, c) 99-144, d) 83, e) 90 (A S M International, 2000).

104. Cicek, V. & Al-Numan, B. *Corrosion Chemistry* a) 3-5, b) 7-14 (John Wiley & Sons, Incorporated, Scrivener Publishing LLC, 2011).

105. Esmaily, M., Svensson, J., Fajardo, S., Birbilis, N., Frankel, G., Virtanen, S., Arrabal, R., Thomas, S. & Johansson, L. Fundamentals and advances in magnesium alloy corrosion. *Progress in Materials Science* **89,** 92–193 (2017).

106. Pilling, N. B. & Bedworth, R. E. The oxidation of metals at high temperatures. *Journal of the Institute of Metals* **29,** 529–591 (1923).

107. Xu, C. & Gao, W. Pilling-Bedworth ratio for oxidation of alloys. *Materials Research Innovations* **3,** 231–235 (2000).

108. Zeng, R.-C., Sun, L., Zheng, Y.-F., Cui, H.-Z. & Han, E.-H. Corrosion and characterisation of dual phase Mg–Li–Ca alloy in Hank's solution: The influence of microstructural features. *Corrosion Science* **79,** 69–82 (2014).

109. Van Muylder, J. & Pourbaix, M. *Magnesium* in *Atlas of electrochemical equilibria in aqueous solutions* (ed Pourbaix, M.) 2nd english ed., 139–145 (National Association of Corrosion Engineers, 1974).

110. Rossrucker, L., Samaniego, A., Grote, J.-P., Mingers, A. M., Laska, C. A., Birbilis, N., Frankel, G. S. & Mayrhofer, K. J. J. The pH Dependence of Magnesium Dissolution and Hydrogen Evolution during Anodic Polarization. *Journal of The Electrochemical Society* **162,** C333–C339 (2015).

111. Johnston, S., Shi, Z. & Atrens, A. The influence of pH on the corrosion rate of high-purity Mg, AZ91 and ZE41 in bicarbonate buffered Hanks' solution. *Corrosion Science* **101,** 182–192 (2015).

112. Santucci, R. J., McMahon, M. E. & Scully, J. R. Utilization of chemical stability diagrams for improved understanding of electrochemical systems: evolution of solution chemistry towards equilibrium. *npj Materials Degradation* **2,** 1 (2018).

113. Abbasi, S., Aliofkhazraei, M., Mojiri, H., Amini, M., Ahmadzadeh, M. & Shourgeshty, M. Corrosion behavior of pure Mg and AZ31 magnesium alloy. *Protection of Metals and Physical Chemistry of Surfaces* **53,** 573–578 (2017).

114. Ng, W. F., Chiu, K. Y. & Cheng, F. T. Effect of pH on the *in vitro* corrosion rate of magnesium degradable implant material. *Materials Science and Engineering: C* **30,** 898–903 (2010).

115. Lebouil, S., Gharbi, O., Volovitch, P. & Ogle, K. Mg Dissolution in Phosphate and Chloride Electrolytes: Insight into the Mechanism of the Negative Difference Effect. *CORROSION* **71,** 234–241 (2015).

116. Beetz, W. XXXIV. On the development of hydrogen from the anode. *The London, Edinburgh, and Dublin Philosophical Magazine and Journal of Science* **32,** 269–278 (1866).

117. Światowska, J., Volovitch, P. & Ogle, K. The anodic dissolution of Mg in NaCl and Na2SO4 electrolytes by atomic emission spectroelectrochemistry. *Corrosion Science* **52,** 2372–2378 (2010).

118. Atrens, A., Chen, X. & Shi, Z. Mg Corrosion—Recent Progress. *Corrosion and Materials Degradation* **3,** 566–597 (2022).

119. Atrens, A. & Dietzel, W. The Negative Difference Effect and Unipositive Mg+. *Advanced Engineering Materials* **9,** 292–297 (2007).

120. Cao, F., Song, G.-L. & Atrens, A. Corrosion and passivation of magnesium alloys. *Corrosion Science* **111,** 835–845 (2016).

121. Liu, Y., Liu, D., You, C. & Chen, M. Effects of grain size on the corrosion resistance of pure magnesium by cooling rate-controlled solidification. *Frontiers of Materials Science* **9,** 247–253 (2015).

122. Ralston, K. D., Birbilis, N. & Davies, C. H. J. Revealing the relationship between grain size and corrosion rate of metals. *Scripta Materialia* **63,** 1201–1204 (2010).

123. Ralston, K. D., Williams, G. & Birbilis, N. Effect of pH on the Grain Size Dependence of Magnesium Corrosion. *Corrosion* **68,** 507–517 (2012).

124. Qu, Z., Liu, L., Deng, Y., Tao, R., Liu, W., Zheng, Z. & Zhao, M.-C. Relationship between Biodegradation Rate and Grain Size Itself Excluding Other Structural Factors Caused by Alloying Additions and Deformation Processing for Pure Mg. *Materials* **15,** 5295 (2022).

125. Song, G.-L. & Xu, Z. Effect of microstructure evolution on corrosion of different crystal surfaces of AZ31 Mg alloy in a chloride containing solution. *Corrosion Science* **54,** 97–105 (2012).

126. Liu, M., Qiu, D., Zhao, M.-C., Song, G. & Atrens, A. The effect of crystallographic orientation on the active corrosion of pure magnesium. *Scripta Materialia* **58,** 421–424 (2008).

127. Gerashi, E., Alizadeh, R. & Langdon, T. G. Effect of crystallographic texture and twinning on the corrosion behavior of Mg alloys: A review. *Journal of Magnesium and Alloys* **10,** 313–325 (2022).

128. Bland, L. G., Gusieva, K. & Scully, J. R. Effect of Crystallographic Orientation on the Corrosion of Magnesium: Comparison of Film Forming and Bare Crystal Facets using Electrochemical Impedance and Raman Spectroscopy. *Electrochimica Acta* **227,** 136–151 (2017).

129. McCall, C. R., Hill, M. A. & Lillard, R. S. Crystallographic pitting in magnesium single crystals. *Corrosion Engineering, Science and Technology* **40,** 337–343 (2005).

130. Wang, B., Xu, D., Dong, J. & Ke, W. Effect of Texture on Biodegradable Behavior of an As-Extruded Mg–3%Al–1%Zn Alloy in Phosphate Buffer Saline Medium. *Journal of Materials Science & Technology* **32,** 646–652 (2016).

131. Agha, N. A., Feyerabend, F., Mihailova, B., Heidrich, S., Bismayer, U. & Willumeit-Römer, R. Magnesium degradation influenced by buffering salts in concentrations typical of *in vitro* and *in vivo* models. *Materials Science and Engineering: C* **58,** 817–825 (2016).

132. Kwon, D., Pham, H. V., Song, P. & Moon, S. Corrosion Behavior of the AZ31 Mg Alloy in Neutral Aqueous Solutions Containing Various Anions. *Metals* **13,** 962 (2023).

133. Silva, E. L., Lamaka, S. V., Mei, D. & Zheludkevich, M. L. The Reduction of Dissolved Oxygen During Magnesium Corrosion. *ChemistryOpen* **7,** 664–668 (2018).

134. Xu, L., Liu, X., Sun, K., Fu, R. & Wang, G. Corrosion Behavior in Magnesium-Based Alloys for Biomedical Applications. *Materials* **15,** 2613 (2022).

135. Kieke, M., Feyerabend, F., Lemaitre, J., Behrens, P. & Willumeit-Römer, R. Degradation rates and products of pure magnesium exposed to different aqueous media under physiological conditions. *BioNanoMaterials* **17,** 131–143 (2016).

136. Mei, D., Lamaka, S. V., Gonzalez, J., Feyerabend, F., Willumeit-Römer, R. & Zheludkevich, M. L. The role of individual components of simulated body fluid on the corrosion behavior of commercially pure Mg. *Corrosion Science* **147,** 81–93 (2019).

137. Martinez Sanchez, A. H., Luthringer, B. J. C., Feyerabend, F. & Willumeit, R. Mg and Mg alloys: How comparable are in vitro and in vivo corrosion rates? A review. *Acta Biomaterialia* **13,** 16–31 (2015).

138. Zhao, D., Wang, T., Nahan, K., Guo, X., Zhang, Z., Dong, Z., Chen, S., Chou, D.-T., Hong, D., Kumta, P. N. & Heineman, W. R. *In vivo* characterization of magnesium alloy biodegradation using electrochemical H2 monitoring, ICP-MS, and XPS. *Acta Biomaterialia* **50,** 556–565 (2017).

139. Hofstetter, J., Martinelli, E., Weinberg, A. M., Becker, M., Mingler, B., Uggowitzer, P. J. & Löffler, J. F. Assessing the degradation performance of ultrahigh-purity magnesium in vitro and in vivo. *Corrosion Science* **91,** 29–36 (2015).

140. Hillis, J. E. The Effects of Heavy Metal Contamination on Magnesium Corrosion Performance. *SAE Transactions* **92,** 553–559 (1983).

141. Hanawalt, J. D., Nelson, C. & Peloubet, J. A. Corrosion Studies of Magnesium and Its Alloys. *Transactions of the American Institute of Mining and Metallurgical Engineers* **147,** 273–299 (1942).

142. Südholz, A. D., Kirkland, N. T., Buchheit, R. G. & Birbilis, N. Electrochemical Properties of Intermetallic Phases and Common Impurity Elements in Magnesium Alloys. *Electrochemical and Solid-State Letters* **14,** C5–C7 (2011).

143. Parfenov, E. V., Kulyasova, O. B., Mukaeva, V. R., Mingo, B., Farrakhov, R. G., Cherneikina, Y. V., Yerokhin, A., Zheng, Y. F. & Valiev, R. Z. Influence of ultra-fine grain structure on corrosion behaviour of biodegradable Mg-1Ca alloy. *Corrosion Science* **163,** 108303 (2020).

144. Xu, D. K. & Han, E. H. Effect of quasicrystalline phase on improving the corrosion resistance of a duplex structured Mg–Li alloy. *Scripta Materialia* **71,** 21–24 (2014).

145. Zhao, W., Wang, J., Weiyang, J., Qiao, B., Wang, Y., Li, Y. & Jiang, D. A novel biodegradable Mg-1Zn-0.5Sn alloy: Mechanical properties, corrosion behavior, biocompatibility, and antibacterial activity. *Journal of Magnesium and Alloys* **8,** 374–386 (2020).

146. Du, W., Liu, K., Ma, K., Wang, Z. & Li, S. Effects of trace Ca/Sn addition on corrosion behaviors of biodegradable Mg–4Zn–0.2Mn alloy. *Journal of Magnesium and Alloys* **6,** 1–14 (2018).

147. Blawert, C., Heitmann, V., Dietzel, W., Störmer, M., Bohne, Y., Mändl, S. & Rauschenbach, B. Corrosion Properties of Supersaturated Magnesium Alloy Systems. *Materials Science Forum* **539-543,** 1679–1684 (2007).

148. Sun, Y.-h., Wang, R.-c., Peng, C.-q., Feng, Y. & Yang, M. Corrosion behavior and surface treatment of superlight Mg–Li alloys. *Transactions of Nonferrous Metals Society of China* **27,** 1455–1475 (2017).

149. *Solubility Product Constants of Inorganic Salts* in *CRC handbook of chemistry and physics: a ready reference book of chemical and physical data* (eds Rumble, J. R., Bruno, T. J. & Doa, M. J.) 103rd ed., 5-192–5-193 (CRC press, 2022).

150. Li, C. Q., Xu, D. K., Chen, X.-B., Wang, B. J., Wu, R. Z., Han, E. H. & Birbilis, N. Composition and microstructure dependent corrosion behaviour of Mg-Li alloys. *Electrochimica Acta* **260,** 55–64 (2018).

151. Wang, B.-J., Luan, J.-Y., Xu, D.-K., Sun, J., Li, C.-Q. & Han, E.-H. Research Progress on the Corrosion Behavior of Magnesium–Lithium-Based Alloys: A Review. *Acta Metallurgica Sinica (English Letters)* **32,** 1–9 (2019).

152. Taheri, M., Danaie, M. & Kish, J. R. TEM Examination of the Film Formed on Corroding Mg Prior to Breakdown. *Journal of The Electrochemical Society* **161,** C89–C94 (2013).

153. Li, C., He, Y. & Huang, H. Effect of lithium content on the mechanical and corrosion behaviors of HCP binary Mg–Li alloys. *Journal of Magnesium and Alloys* **9,** 569–580 (2021).

154. Cano, Z. P., McDermid, J. R. & Kish, J. R. Cathodic Activity of Corrosion Filaments Formed on Mg Alloy AM30. *Journal of The Electrochemical Society* **162,** C732–C740 (2015).

155. Xiang, Q., Jiang, B., Zhang, Y., Chen, X., Song, J., Xu, J., Fang, L. & Pan, F. Effect of rolling-induced microstructure on corrosion behaviour of an as-extruded Mg-5Li-1Al alloy sheet. *Corrosion Science* **119,** 14–22 (2017).

156. Dobkowska, A., Adamczyk-Cieslak, B., Mizera, J., Kubásek, J. & Vojtěch, D. Corrosion Behaviour of Magnesium Lithium Alloys in NaCl Solution. *Solid State Phenomena* **227,** 87–90 (2015).

157. Liu, X., Wang, X., Guo, E., Chen, Z., Kang, H. & Wang, T. Influence of deformation on the corrosion behavior of LZ91 Mg—Li alloy. *International Journal of Minerals, Metallurgy and Materials* **30,** 72–81 (2023).

158. Song, Y., Shan, D., Chen, R. & Han, E.-H. Corrosion characterization of Mg–8Li alloy in NaCl solution. *Corrosion Science* **51,** 1087–1094 (2009).

159. Wang, B. J., Xu, D. K., Cai, X., Qiao, Y. X. & Sheng, L. Y. Effect of rolling ratios on the microstructural evolution and corrosion performance of an as-rolled Mg-8 wt.%Li alloy. *Journal of Magnesium and Alloys* **9,** 560–568 (2021).

160. Dobkowska, A., Adamczyk – Cieślak, B., Kubásek, J., Vojtěch, D., Kuc, D., Hadasik, E. & Mizera, J. Microstructure and corrosion resistance of a duplex structured Mg–7.5Li–3Al–1Zn. *Journal of Magnesium and Alloys* **9,** 467–477 (2021).

161. Yan, Y., Qiu, Y., Gharbi, O., Birbilis, N. & Nakashima, P. N. H. Characterisation of Li in the surface film of a corrosion resistant Mg-Li(-Al-Y-Zr) alloy. *Applied Surface Science* **494,** 1066–1071 (2019).

162. Yan, Y. M., Maltseva, A., Zhou, P., Li, X. J., Zeng, Z. R., Gharbi, O., Ogle, K., La Haye, M., Vaudescal, M., Esmaily, M., Birbilis, N. & Volovitch, P. On the in-situ aqueous stability of an Mg-Li-(Al-Y-Zr) alloy: Role of Li. *Corrosion Science* **164,** 108342 (2020).

163. Chen, X.-B., Li, C. & Xu, D. Biodegradation of Mg-14Li alloy in simulated body fluid: A proof-of-concept study. *Bioactive Materials* **3,** 110–117 (2018).

164. Li, C. Q., Xu, D. K., Zhang, Z. R. & Han, E. H. Influence of the lithium content on the negative difference effect of Mg-Li alloys. *Journal of Materials Science & Technology* **57,** 138–145 (2020).

165. Li, C., Liang, D., Lin, Y., Dong, Y., Shi, B., Yan, C. & Zhang, Z. Effect of Li Content on the Surface Film Formed on the Binary Mg–Li Alloys in NaCl Solution. *Metals and Materials International* **30,** 127–142 (2024).

166. Hou, L., Raveggi, M., Chen, X.-B., Xu, W., Laws, K. J., Wei, Y., Ferry, M. & Birbilis, N. Investigating the Passivity and Dissolution of a Corrosion Resistant Mg-33at.%Li Alloy in Aqueous Chloride Using Online ICP-MS. *Journal of The Electrochemical Society* **163,** C324–C329 (2016).

167. Zhou, B.-C., Shang, S.-L., Wang, Y. & Liu, Z.-K. Diffusion coefficients of alloying elements in dilute Mg alloys: A comprehensive first-principles study. *Acta Materialia* **103,** 573–586 (2016).

168. Yan, Y. M., Gharbi, O., Maltseva, A., Chen, X. B., Zeng, Z. R., Xu, S. W., Xu, W. Q., Volovich, P., Ferry, M. & Birbilis, N. Investigating the Structure of the Surface Film on a Corrosion Resistant Mg-Li(-Al-Y-Zr) Alloy. *CORROSION* **75,** 80–89 (2019).

169. Zaghloul, B. & Kish, J. R. Corrosion Inhibition of Mg Alloy ZEK100 Sheet Metal by Dissolved Lithium Carbonate. *Journal of The Electrochemical Society* **168,** 081507 (2021).

170. Feng, J., Zhang, H., Zhang, L., Zou, G., Wang, J. & Peng, Q. Microstructure and corrosion properties for ultrahigh-pressure Mg-Li alloys. *Corrosion Science* **206,** 110519 (2022).

171. Kirkland, N. T., Birbilis, N. & Staiger, M. P. Assessing the corrosion of biodegradable magnesium implants: A critical review of current methodologies and their limitations. *Acta Biomaterialia* **8,** 925–936 (2012).

172. Ghoneim, A. A., Fekry, A. M. & Ameer, M. A. Electrochemical behavior of magnesium alloys as biodegradable materials in Hank's solution. *Electrochimica Acta* **55,** 6028–6035 (2010).

173. Thirumalaikumarasamy, D., Shanmugam, K. & Balasubramanian, V. Comparison of the corrosion behaviour of AZ31B magnesium alloy under immersion test and potentiodynamic polarization test in NaCl solution. *Journal of Magnesium and Alloys* **2,** 36–49 (2014).

174. Van Gaalen, K., Quinn, C., Weiler, M., Gremse, F., Benn, F., McHugh, P. E., Vaughan, T. J. & Kopp, A. Predicting localised corrosion and mechanical performance of a PEO surface modified rare earth magnesium alloy for implant use through in-silico modelling. *Bioactive Materials* **26,** 437–451 (2023).

175. Song, G., Atrens, A. & StJohn, D. *An Hydrogen Evolution Method for the Estimation of the Corrosion Rate of Magnesium Alloys* in *Magnesium Technology 2001* (ed Hryn, J. N.) 1st ed., 254–262 (John Wiley & Sons, Ltd, 2001).

176. Jurgeleit, T., Quandt, E. & Zamponi, C. Magnetron Sputtering a New Fabrication Method of Iron Based Biodegradable Implant Materials. *Advances in Materials Science and Engineering* **2015,** 294686 (2015).

177. Schmickler, W. & Santos, E. *Interfacial electrochemistry* 2nd ed., 92–96 (Springer, 2010).

178. Dickinson, E. J. F. & Wain, A. J. The Butler-Volmer equation in electrochemical theory: Origins, value, and practical application. *Journal of Electroanalytical Chemistry* **872,** 114145 (2020).

179. Hamann, C. H. & Vielstich, W. *Elektrochemie* 4th ed., 166–168 (Wiley-VCH, 2005).

180. Shi, Z., Liu, M. & Atrens, A. Measurement of the corrosion rate of magnesium alloys using Tafel extrapolation. *Corrosion Science* **52,** 579–588 (2010).

181. Song, G. & Atrens, A. Understanding Magnesium Corrosion—A Framework for Improved Alloy Performance. *Advanced Engineering Materials* **5,** 837–858 (2003).

182. Rossrucker, L., Mayrhofer, K. J. J., Frankel, G. S. & Birbilis, N. Investigating the Real Time Dissolution of Mg Using Online Analysis by ICP-MS. *Journal of The Electrochemical Society* **161,** C115–C119 (2014).

183. Pardo, A., Feliu, S., Merino, M. C., Arrabal, R. & Matykina, E. Electrochemical Estimation of the Corrosion Rate of Magnesium/Aluminium Alloys. *International Journal of Corrosion* **2010,** 953850 (2010).

184. Curioni, M. The behaviour of magnesium during free corrosion and potentiodynamic polarization investigated by real-time hydrogen measurement and optical imaging. *Electrochimica Acta* **120,** 284–292 (2014).

185. Cherevko, S. & Mayrhofer, K. J. J. *On-Line Inductively Coupled Plasma Spectrometry in Electrochemistry: Basic Principles and Applications* in *Encyclopedia of Interfacial Chemistry: Surface Science and Electrochemistry* (ed Wandelt, K.) 326–335 (Elsevier, 2018).

186. Liu, Y., Wu, Y., Bian, D., Gao, S., Leeflang, S., Guo, H., Zheng, Y. & Zhou, J. Study on the Mg-Li-Zn ternary alloy system with improved mechanical properties, good degradation performance and different responses to cells. *Acta Biomaterialia* **62,** 418–433 (2017).

187. Nene, S. S., Kashyap, B. P., Prabhu, N., Estrin, Y. & Al-Samman, T. Biocorrosion and biodegradation behavior of ultralight Mg–4Li–1Ca (LC41) alloy in simulated body fluid for degradable implant applications. *Journal of Materials Science* **50,** 3041–3050 (2015).

188. Ogle, K. Atomic Emission Spectroelectrochemistry: Real-Time Rate Measurements of Dissolution, Corrosion, and Passivation. *Corrosion* **75,** 1398–1419 (2019).

189. Ogle, K. & Weber, S. Anodic Dissolution of 304 Stainless Steel Using Atomic Emission Spectroelectrochemistry. *Journal of The Electrochemical Society* **147,** 1770–1780 (2000).

190. Hochstrasser-Kurz, S., Reiss, D., Suter, T., Latkoczy, C., Günther, D., Virtanen, S., Uggowitzer, P. J. & Schmutz, P. ICP-MS, SKPFM, XPS, and Microcapillary Investigation of the Local Corrosion Mechanisms of WC–Co Hardmetal. *Journal of The Electrochemical Society* **155,** C415–C426 (2008).

191. Klemm, S. O., Topalov, A. A., Laska, C. A. & Mayrhofer, K. J. J. Coupling of a high throughput microelectrochemical cell with online multielemental trace analysis by ICP-MS. *Electrochemistry Communications* **13,** 1533–1535 (2011).

192. Kasian, O., Geiger, S., Mayrhofer, K. J. J. & Cherevko, S. Electrochemical On-line ICP-MS in Electrocatalysis Research. *The Chemical Record* **19,** 2130–2142 (2019).

193. Shkirskiy, V., Maciel, P., Deconinck, J. & Ogle, K. On The Time Resolution of the Atomic Emission Spectroelectrochemistry Method. *Journal of The Electrochemical Society* **163,** C37–C44 (2016).

194. Han, L., Li, X., Bai, J., Xue, F., Zheng, Y. & Chu, C. Effects of flow velocity and different corrosion media on the *in vitro* bio-corrosion behaviors of AZ31 magnesium alloy. *Materials Chemistry and Physics* **217,** 300–307 (2018).

195. Li, Z. & Zhang, J. The influence of flow velocity on electrochemical reaction of metal surface. *IOP Conference Series: Materials Science and Engineering* **274,** 012098 (2017).

196. Dworschak, D., Brunnhofer, C. & Valtiner, M. Photocorrosion of ZnO Single Crystals during Electrochemical Water Splitting. *ACS Applied Materials & Interfaces* **12,** 51530–51536 (2020).

197. Dworschak, D., Cheng, H.-W., Ku, C.-S., Chiang, C.-Y., Lin, C.-H. & Valtiner, M. Comparison of elemental resolved non-confined and restricted electrochemical degradation of nickel base alloys. *Corrosion Science* **190,** 109629 (2021).

198. Shkirskiy, V., King, A. D., Gharbi, O., Volovitch, P., Scully, J. R., Ogle, K. & Birbilis, N. Revisiting the Electrochemical Impedance Spectroscopy of Magnesium with Online Inductively Coupled Plasma Atomic Emission Spectroscopy. *ChemPhysChem* **16,** 536–539 (2015).

199. Jenewein, K. J., Kormányos, A., Knöppel, J., Mayrhofer, K. J. J. & Cherevko, S. Accessing In Situ Photocorrosion under Realistic Light Conditions: Photoelectrochemical Scanning Flow Cell Coupled to Online ICP-MS. *ACS Measurement Science Au* **1,** 74–81 (2021).

200. Yan, Y., Zhou, P., Gharbi, O., Zeng, Z., Chen, X., Volovitch, P., Ogle, K. & Birbilis, N. Investigating ion release using inline ICP during in situ scratch testing of an Mg-Li(-Al-Y-Zr) alloy. *Electrochemistry Communications* **99,** 46–50 (2019).

201. Thomas, S., Gharbi, O., Salleh, S. H., Volovitch, P., Ogle, K. & Birbilis, N. On the effect of Fe concentration on Mg dissolution and activation studied using atomic emission spectroelectrochemistry and scanning electrochemical microscopy. *Electrochimica Acta* **210,** 271–284 (2016).

202. Hanke, L., Jessen, L., Weisheit, F., Bhat, K., Westernströer, U., Garbe-Schönberg, D., Willumeit-Römer, R. & Quandt, E. Structural characterisation and degradation of Mg-Li thin films for biodegradable implants. *Scientific Reports* **13,** 12572 (2023).

203. Birbilis, N., Ralston, K. D., Virtanen, S., Fraser, H. L. & Davies, C. H. J. Grain character influences on corrosion of ECAPed pure magnesium. *Corrosion Engineering, Science and Technology* **45,** 224–230 (2010).

204. Pursel, S. M., Petrilli, J. D., Horn, M. W. & Shaw, B. A. *Effect of alloy addition and growth conditions on the formation of Mg-based bioabsorbable thin films* in *Nanostructured Thin Films* (eds Smith, G. B. & Lakhtakia, A.) 704113 (SPIE, 2008).

205. Lee, M. H., Bae, I. Y., Kim, K. J., Moon, K. M. & Oki, T. Formation mechanism of new corrosion resistance magnesium thin films by PVD method. *Surface and Coatings Technology* **169-170,** 670–674 (2003).

206. Hanke, L., Kalchgruber, L., Westernströer, U., Garbe-Schönberg, D., Quandt, E. & Valtiner, M. Investigation of in-situ ion release and surface film formation of hcp Mg-Li thin films. *Corrosion Science* **238,** 112361 (2024).

207. Hanke, L., Hartig, T., Weisheit, F., Tjardts, T., Pogoda, T., Faupel, F. & Quandt, E. Tailoring of Mg and MgLi thin-film corrosion rates with dielectric barrier discharge plasma treatment. *Journal of Vacuum Science and Technology A* **41,** 053109 (2023).

208. Weiss, A., Pauly, H. & Witte, H. Kubisch-flächenzentrierte Legierungen der Zusammensetzung Li2 Mg X mit raumzentrierter Unterstruktur. *Zeitschrift für Metallkunde* **59.** COD ID: 1509442, 414–418 (1968).

209. Bhat, K., Schlotterose, L., Hanke, L., Helmholz, H., Quandt, E., Hattermann, K. & Willumeit-Römer, R. Magnesium-lithium thin films for neurological applications–An *in vitro* investigation of glial cytocompatibility and neuroinflammatory response. *Acta Biomaterialia* **178,** 307–319 (2024).

210. Bhat, K., Hanke, L., Helmholz, H., Quandt, E., Pixley, S. & Willumeit-Römer, R. Influence of Magnesium Degradation on Schwannoma Cell Responses to Nerve Injury Using an In Vitro Injury Model. *Journal of Functional Biomaterials* **15,** 88 (2024).

Acknowledgements

This work would not have been possible without all the great support I received. Therefore, I would like to thank:

My supervisor Prof. Dr. Eckhard Quandt for being able to work in his group on this interesting, interdisciplinary topic and the support and helpful suggestions during the last four years.

Prof. Dr. Regine Willumeit-Römer for her support during my PhD regarding magnesium and corrosion specific questions as my second supervisor.

My colleagues of the group inorganic functional materials for helping me to learn the necessary machines and for the general support both scientific and personal, especially Lea Jessen for teaching me everything about Mg thin films and measurement techniques available, but also helping me to generally feeling welcomed in the group when I started. Thanks to Hanna Lewitz, Lars Thormälen, Dr. Justin Jetter, Felix Weisheit and Duygu Dengiz for being not only a great help by practical support, answering questions and discussing problems but also by moral support. A special thanks goes to Lars for keeping the machines alive so that experimental work was possible.

My colleagues from the research training group "Materials for Brain", especially Krathika Bhat, for continuous discussions over the time of the PhD and a lot of help to understand the requirements from a biological point of view but also the willingness to learn the material science part so that actual exchange was possible.

Prof. Dr. Markus Valtiner for not only hosting me during my research at the TU Vienna, but also being available for any questions and discussions during that stay and motivating me to develop a deeper understanding of my scientific problems. I would like to extend my gratitude to the group members in Vienna, Lukas Kalchgruber, Dr. Laura Mears and Matteo Olgiati for helping me learn the machines, answering all my questions and helping me with further measurements and everyone else for creating a pleasant working atmosphere.

Ulrike Westernströer and by extension Dr. Dieter-Garbe Schönberg for agreeing to measuring my samples by ICP-MS without which many parts of my studies would not have been possible or relevant.

Last but not least I would like to thank my family, especially my parents and my sister, and my friends for continuously supporting and motivating me.